CHAPTER 5

SUBCOOLED FLOW BOILING OF FC-72 ON A HEADED MICRO PIN-FINNED SILICON CHIP FLUSH MOUNTED ON BOTTOM OF RECTANGULAR CHANNEL

The experimental data obtained in the second part of this study are presented in this chapter to illustrate the subcooled flow boiling heat transfer on a heated micro pin-finned silicon chip flush mounted onto the bottom of a rectangular channel. The present experiments are carried out for the dielectric coolant FC-72 flowing in a rectangular channel with the mass flux of FC-72 varying from 287 kg/m^{2}s to 431 kg/m^{2}s, coolant inlet subcooled temperature from 2.3 ^{o}C to 4.3 ^{o}C, and imposed heat flux from 1 W/cm^2 to 10 W/cm^2. Besides, the silicon chips contain three different geometries of surface micro-structures, namely, the smooth, pin-finned 200 and pin-finned 100 surfaces. The coolant is at atmospheric pressure with T_{sat} = 54.3 ^{o}C.

In the following, the effects of the coolant mass flux, inlet subcooling, imposed heat flux, and surface micro-structures on the FC-72 subcooled flow boiling heat transfer performance and associated bubble characteristics are examined in detail. The heat transfer performance is also presented in terms of the boiling curves and boiling heat transfer coefficients.

5.1 Subcooled Flow Boiling Curves

Effects of the coolant mass flux G, inlet subcooling ΔT_{sub}, and surface micro-structures of the heated silicon chip on the boiling curves measured in the FC-72 subcooled flow boiling are shown in Figs. 5.1 - 5.8.

The effects of the mass flux on the boiling curves illustrated in Fig. 5.1 for the chip

with a smooth surface indicate that for a given boiling curve as the imposed heat flux gradually increases from a small value, the temperature of the chip surface increases from a subcooled state to a certain value just exceeding the saturated temperature of the coolant. No bubble nucleation is observed. The heat transfer in this region is completely due to the single-phase forced convection. With the continuing increase in the chip surface heat flux, bubbles begin to appear on the surface and there is a sudden drop in the temperature of chip surface. We have onset of nucleate boiling (ONB) in the flow. The reason causing the sudden drop in the chip surface temperature at ONB is due to a significant increase in the wall heat transfer by the boiling processes. A close inspection of the data for the single-phase region further reveals that at a higher mass flux of 431 kg/m^2s the chip surface temperature is somewhat lower for the same imposed heat flux. This obviously results from the increase in the single-phase convection heat transfer coefficient with the coolant mass flux. Note that except for the imposed heat flux slightly beyond that for ONB the coolant mass flux exhibits little effects on the boiling curves, suggesting that the dominance of the wall heat transfer by the fully developed nucleate boiling. Similar results were found by Willingham and Mudarar [11]. However at a higher G the wall superheat and heat flux at ONB are substantially higher. This can be attributed to the fact that at a higher G more energy is needed for the vapor to nucleate from the cavities in the wall since the residence time of the coolant on the chip is shorter. Checking the results in Figs. 5.2 and 5.3 reveals that for the pin-finned surfaces the boiling curves show similar trend to that for the smooth surface. A scrutiny of these data further suggests that the fully developed nucleate boiling prevails in the flow after ONB.

Next, the effects of the inlet subcooling of the coolant on the boiling curve shown in Fig. 5.4 for the chip with a smooth surface indicate that the wall superheat and the

imposed heat flux for the incipient boiling are both somewhat higher at a larger inlet subcooling of the coolant. Moreover, at the same ΔT_{sat} the boiling heat flux is noticeably higher only in the region just beyond ONB. Elsewhere in the fully developed nucleate boiling region the effects of the inlet liquid subcooling are rather insignificant. This is in accordance with the results from Heindel et al. [12] and Tso et al. [14]. It is of interest to note that the onset of nucleate boiling heat flux delays to a higher value at increasing inlet liquid subcooling is due to the fact that more energy is needed for boiling incipience on the chip surface when the bulk liquid is in a more subcooled state. For the finned surface, the effects of ΔT_{sub} on the wall superheat and wall heat flux at the incipient boiling are similar to the chip for smooth surface (Figs. 5.5 and 5.6). Moreover, for the finned surface the surface heat flux is slightly higher in the single-phase region for a higher ΔT_{sub}.

Finally, how the boiling curves are affected by the surface micro-structure of the chip is shown in Figs. 5.7 and 5.8. The results clearly indicate that in both the single-phase and nucleate boiling regions at the same wall superheat the chip surface heat flux is highest for the pin-finned 100 surface and lowest for the smooth surface, suggesting that using the micro pin-finned structure can effectively enhance the single-phase and flow boiling heat transfer from the chip. The large increase in the total surface area by the micro pin-fins is indeed beneficial for the heat transfer. Note that the boiling curves for the pin-finned 100 surface are relatively steep in the nucleate boiling region, implying very effective heat removal by the bubble nucleation in this region. Besides, the wall superheat required for the boiling inception is substantially lower for the pin-finned 100 surface. This is ascribed to the increase in the density of the active nucleation sites by the surface micro-structures. Particularly, in the corner region of the pin fins the bubbles are found to appear at a lower ΔT_{sat}.

5.2 Subcooled Flow Boiling Heat Transfer Coefficient

We proceed to examine how the subcooled flow boiling heat transfer coefficient $h_{2\phi,sub}$ is affected by the FC-72 coolant mass flux, inlet subcooling and the surface micro-structures. The results for the variations of $h_{2\phi,sub}$ with the surface heat flux presented in Figs. 5.9 - 5.11 indicate that the coolant mass flux exhibits little influences on the flow boiling heat transfer coefficients for the smooth and finned surfaces. However, for a given coolant mass flux the boiling heat transfer coefficient increases substantially with the imposed heat flux. Moreover, the inlet subcooling of the coolant also show a significant effect on the boiling heat transfer coefficients, as evident from the data in Figs. 5.12 - 5.14. Specifically, $h_{2\phi,sub}$ is higher for a lower ΔT_{sub}. The inlet subcooling effect is stronger at a higher imposed heat flux for the pin-finned surfaces. Finally, it is noted from Figs. 5.15 and 5.16 that the surface micro-structures in the form of micro-pin-fins produce some positive effects on the boiling heat transfer coefficient at high imposed heat flux. This is because the increase in the active nucleation sites by adding the pin-fin structures to the chip surface can effectively promote boiling heat transfer performance. Besides, the heat transfer is further enhanced by a serpentine motion of liquid between adjacent rows of pin-fins, which in turn augment turbulent mixing. Furthermore, there exists the development of multiple thermal entry regions at the top surfaces of individual pin-fins.

5.3 Bubble characteristics

To elucidate the FC-72 subcooled flow boiling heat transfer characteristics, the data for the bubble characteristics obtained from the present flow visualization are examined in the following. At first, the top views of the boiling flow for various coolant mass flow rates, imposed heat fluxes and inlet subcoolings are shown in Figs.

5.17 - 5.22 for the chips with the smooth and micro-structured surfaces.

In the flow visualization we note that as the wall superheat exceeds that for the boiling incipience, the vapor bubbles generated from the heated surface begin to appear. In the beginning, tiny bubbles are observed in the active nucleation sites corresponding to ΔT_w. The tiny bubbles keep growing until their diameters reach to a certain size and they detach from the active nucleation sites immediately and then slide along the heating surface. The processes of bubble growth and departure are nearly regular and the bubbles are nearly spherical at low imposed heat flux. The formation, growth, and detachment processes of the bubbles on the heated chip surface obviously depend on the flow and thermal conditions and on the geometry of the cavities. The top view flow photos given in Figs. 5.17 - 5.22 clearly indicate that more nucleation sites are activated and more bubbles are generated from the chip surface at higher imposed heat flux, lower coolant mass flux, and lower inlet liquid subcooling for both smooth and finned surfaces. Thus at these conditions the merging of small bubbles to form large bubbles occurs more frequently.

To quantify the bubble characteristics, the measured data for the mean bubble departure diameter, bubble departure frequency and active nucleation site density are given in Figs. 5.23 - 5.46. The effects of the coolant mass flux G, inlet liquid subcooling ΔT_{sub}, imposed heat flux q", and surface micro-structures on the bubble characteristics are examined in the following. The results in Figs. 5.23 - 5.25 clearly show that increasing the coolant mass flux can significantly reduce the size of the bubbles departing from the chips with the smooth and finned surfaces. This is simply due to the higher drag acting on the bubbles still attaching the cavities by the surrounding subcooled liquid flowing at a higher speed for a higher G. We also note that at the higher inlet liquid subcooling the bubbles departing from the heated surface are smaller, as evident from the data in Figs. 5.26 - 5.28. This is considered to result

from the stronger vapor condensation inside the bubbles for a higher ΔT_{sub}. It is further noted from Figs. 5.29 and 5.30 that the presence of the micro pin-fins on the chips causes a significantly earlier departure of the bubbles from the chip surface. But the mean bubble departure diameter is smaller for the surface with larger fins. This is because the liquid coolant may be partially accelerated when it flows through the space between the adjacent pin-fins. The partially accelerated coolant can effectively enhance the drag force acting the bubbles and causes them to detach earlier from the finned surface. But for the pin-finned 100 surface although the partially coolant acceleration is more pronounced, the space between the adjacent fins are so small and the bubbles already contact the sides of the fins before departure. Therefore, the bubbles grow for a longer period of time before they detach from the chip surface. Longer bubble growth time causes the growing bubble to keep absorbing energy from the heated surface and results in a larger mean bubble departure diameter. The mean bubble departure diameter on the pin-finned100 surface is still smaller than that on the smooth surface. The reasonable explanation is that the fin height is smaller than the mean bubble departure diameter so the partially coolant acceleration effect still plays an important role in affecting the bubble departure processes.

Next, the data given in Figs. 5.31 - 5.33 manifest that the mean bubble departure frequency can be substantially augmented by raising the coolant mass flux. The mass flux effects are slightly larger at a higher imposed heat flux. The increase of f with G is attributed again to the higher drag on the bubbles still attaching to the chip surface by the subcooled liquid coolant moving at a higher speed for a higher G. This, in turn, causes an earlier departure of the bubbles from the surface, resulting in a higher departure frequency. It is also noted that the mean bubble departure frequency increases noticeably with the imposed heat flux. Moreover, the bubble departure frequency is somewhat higher for a lower inlet liquid subcooling, according to the

data in Figs. 5.34 - 5.36. This again results from the fact that the vapor condensation in the bubble is less important and the bubble growth rate is faster for a lower ΔT_{sub}. Note that the effects of ΔT_{sub} on f are stronger for the higher coolant mass flux. Finally, the data given in Figs. 5.37 and 5.38 indicate that the bubble departure frequency can be enhanced significantly only by using the pin-finned 200 surface. For the pin-finned 100 surface the space between the adjacent fins is too small, leading to a delay in the departure of bubbles.

Attention is turned to the data for the mean active nucleation site density shown in Figs. 5.39 - 5.46. The active nucleation site density is calculated based on the surface area of a bare chip. Firstly, it is noted from Figs. 5.39 - 5.41 that an increase in the coolant mass flux results in somewhat lower mean active nucleation site densities for the smooth and micro-structured surfaces. This directly relates to the higher imposed heat flux is needed for the boiling inception at a higher G, as already discussed in the previous section. Then, the results given in Figs. 5.42 - 5.44 indicate that the effects of the inlet liquid subcooling variation on the mean active nucleation site density are rather slight. Finally, Figs. 5.45 and 5.46 manifest that adding the micro pin-fins to the chip surface can effectively increase the active nucleation sites. This is ascribed to the increase in the surface area of micro pin-fins. More specifically, the nucleation site density on the pin-finned 100 surface is slightly higher than that on the pin-finned 200 surface.

5.4 Correlation Equations

According to the present experimental data, empirical correlations for the heat transfer coefficient in the subcooled flow boiling of FC-72 on the heated silicon chip flush mounted on the bottom of the rectangular channel are proposed here. The proposed correlating equations for the smooth and micro pin-finned surfaces are

respectively

$$Nu_{2\phi,sub} = \frac{h_{2\phi,sub} \cdot L}{k_l} = [100 \cdot Fr_l^{0.8} + 180 \cdot Bo^{0.4} \cdot Ja^{1.1}] \quad (5.1)$$

and

$$Nu_{2\phi,sub} = \frac{h_{2\phi,sub} \cdot L}{k_l} = [35 \cdot Fr_l^{0.8} + 120 \cdot Bo^{0.4} \cdot Ja^{1.2} \cdot F_{tp,sub}] \quad (5.2)$$

Here the Froude number Fr_l, Boiling number Bo and Jacob number Ja are respectively defined as

$$Fr_l = \frac{G^2}{\rho_l^2 \cdot g \cdot D_h} \quad (5.3)$$

$$Bo = \frac{q''}{G \cdot i_{lv}} \quad (5.4)$$

and

$$Ja = \frac{\rho_l \cdot c_{pl} \cdot \Delta T_{sat}}{\rho_v \cdot i_{lv}} \quad (5.5)$$

where G is the coolant mass flux, ρ_l is the liquid density, g is the acceleration due to gravity, D_h is the hydraulic diameter of the test section, c_{pl} is the liquid specific heat, ΔT_{sat} (= T_w - T_{sat}) is the wall superheat, and L is the chip length. Besides, a dimensionless factor $F_{tp,sub}$ is used to account for the effect of the geometric arrangements of the micro-pin-fins on the boiling heat transfer coefficient and it is defined as

$$F_{tp,sub} = \left(\frac{S_f}{H}\right)^{-0.2} \left(\frac{H-B_f}{W_f}\right)^{-0.06} \left(\frac{N \cdot A_f}{A_s}\right)^{0.3} \quad (5.6)$$

where S_f is the space between two adjacent fins, H is the rectangular channel height, B_f is the fin height, W_f is the fin width, N is the total number of pin-fins on a chip, A_f is the total surface area of a single fin, and A_s is the surface area of a bare chip. The proposed correlations are compared with the present data in Figs. 5.47 and 5.48. The comparison indicates that our data can be correlated with a deviation less than $\pm 25\%$ by the above empirical correlations.

Then, empirical correlations for the average bubble departure diameter in FC-72

subcooled flow boiling on the heated silicon chip flush mounted on the bottom of the rectangular channel estimated from the present flow visualization are proposed as

$$\frac{d_p}{\sqrt{\sigma/g\cdot\Delta\rho}} = \frac{0.38\cdot(\rho_l/\rho_v)^{1.32}}{Re_l^{0.2}\cdot[Ja' + \frac{0.6\cdot(\rho_l/\rho_v)^{0.9}}{Bo^{0.3}Re_l^{0.1}}]} \quad \text{for smooth surafce,} \tag{5.7}$$

and

$$\frac{d_p}{\sqrt{\sigma/g\cdot\Delta\rho}} = \frac{0.17\cdot(\rho_l/\rho_v)^{1.32}\cdot F_{d,sub}}{Re_l^{0.2}\cdot[Ja' + \frac{0.6\cdot(\rho_l/\rho_v)^{0.9}}{Bo^{0.3}Re_l^{0.1}}]} \quad \text{for pin-finned surfaces} \tag{5.8}$$

with the fin-geometry factor $F_{d,sub}$ correlated as

$$F_{d,sub} = (\frac{S_f}{H})^{-0.125}(\frac{H-B_f}{W_f})^{0.05}(\frac{N\cdot A_f}{A_s})^{0.4} \tag{5.9}$$

Here Ja' is the modified Jacob number based on the coolant inlet subcooled temperature ΔT_{sub} and Re_l is the all liquid Reynolds number based on the chip length. They are respectively defined as

$$Ja' = \frac{\rho_l\cdot c_{pl}\cdot\Delta T_{sub}}{\rho_v\cdot i_{lv}} \tag{5.10}$$

and

$$Re_l = \frac{G\cdot L}{\mu_l} \tag{5.11}$$

Note that $F_{d,sub}$ is a dimensionless factor to account for the fin-geometry effects on the mean bubble departure diameter. Figures 5.49 and 5.50 show that the present experimental data fall within ± 20 % of the correlations given in Equations (5.7) and (5.8). In addition, empirical equations are provided to correlate the data for the mean bubble departure frequency as

$$\frac{f\cdot d_p}{\mu_l/\rho_l\cdot D_h} = 0.52Re_l^{1.4}\cdot Ja'^{-0.3}\cdot Bo^{0.5} \quad \text{for smooth surface,} \tag{5.12}$$

and

$$\frac{f\cdot d_p}{\mu_l/\rho_l\cdot D_h} = 0.175Re_l^{1.42}\cdot Ja'^{-0.3}\cdot Bo^{0.53}\cdot F_{fin,sub} \quad \text{for pin-finned surfaces} \tag{5.13}$$

with the fin-geometry factor $F_{fin,sub}$

$$F_{fin,sub} = (\frac{S_f}{H})^{0.12}(\frac{H\text{-}B_f}{W_f})^{0.4}(\frac{N \cdot A_f}{A_s})^{-0.02} \quad (5.14)$$

where $F_{fin,sub}$ is a dimensionless factor accounting for fin-geometry effects on the mean bubble departure frequency. Figures 5.51 and 5.52 reveal that the present experimental data for $f \cdot d_p$ can be correlated with the deviation less than ± 25 % by the above two equations. Moreover, empirical correlations for the mean active nucleation site density in the FC-72 subcooled flow boiling deduced from the present flow visualization are proposed as

$$N_{ac} \cdot d_p^{\,2} = 65 \cdot Bo^{0.87} \cdot Re_l^{\,-0.15} \cdot Ja'^{\,-0.05} \quad \text{for smooth surface,} \quad (5.15)$$

and

$$N_{ac} \cdot d_p^{\,2} = 48 \cdot Bo^{0.85} \cdot Re_l^{\,-0.15} \cdot Ja'^{\,-0.1} \cdot F_{n,sub} \quad \text{for pin-finned surfaces} \quad (5.16)$$

with the factor $F_{n,sub}$ correlated as

$$F_{n,sub} = (\frac{S_f}{H})^{-0.15}(\frac{H\text{-}B_f}{W_f})^{-0.06}(\frac{N \cdot A_f}{A_s}) \quad (5.17)$$

where $F_{n,sub}$ is a dimensionless factor to include the fin geometry effects on the active nucleation site density. The comparison in Figs. 5.53 and 5.54 show that more than 80 % of the present experimental data fall within ± 30 % of the correlation given in Equations (5.15) and (5.16). Finally, the total heat flux input to the boiling flow q_t'' is considered to be roughly composed of two parts: one resulting from the bubble nucleation q_b'' and another due to the single phase forced convection q_c''. Thus

$$q_t'' = q_b'' + q_c'' \quad (5.18)$$

Here q_b" and q_c" can be individually calculated from the quantitative data for the bubble characteristics examined in section 5.3 and single phase liquid forced convection as

$$q_b'' = \rho_v \cdot V_v \cdot f \cdot N_{ac} \cdot i_{lv} \quad (5.19)$$

where ρ_v is the vapor density, V_v is the vapor volume of the mean departing bubble

defined as $\frac{4\pi}{3}(\frac{d_p}{2})^3$, f is the bubble departure frequency, N_{ac} is the active nucleation site density, i_{lv} is the enthalpy of vaporization, and

$$q_c'' = E \cdot \bar{h}_{1\phi} \cdot \Delta T_{sat} \tag{5.20}$$

where E is an enhancement factor added to account for the agitating motion of the bubbles which can enhance the single phase liquid convection heat transfer. From the experimental data, E can be empirically correlated as

$$E = 5.5 \cdot N_{conf}^{0.5} \cdot Fr_l^{0.2} \cdot (1 + 275 \cdot Bo)^{1.8} \quad \text{for smooth surface,} \tag{5.21}$$

and

$$E = 3.3 \cdot N_{conf}^{0.5} \cdot Fr_l^{0.2} \cdot (1 + 250 \cdot Bo)^{1.8} \cdot F_{E,sub} \quad \text{for pin-finned surfaces} \tag{5.22}$$

with the fin-geometry factor $F_{E,sub}$

$$F_{E,sub} = (\frac{S_f}{H})^{-0.16} (\frac{H-B_f}{W_f})^{-0.07} (\frac{N \cdot A_f}{A_s})^{0.04} \tag{5.23}$$

where $F_{E,sub}$ is included above to account for the fin-geometry effects on the enhancement factor. The dimensionless factor N_{conf} is the Confinement number and it is defined as

$$N_{conf} = \frac{(\sigma / g \cdot \Delta\rho)^{0.5}}{D_h} \tag{5.24}$$

The results in Figs. 5.55 & 5.56 indicate that the present data can be correlated with the deviation less than $\pm 25\%$ by the empirical correlation given in Equations (5.18) - (5.24).

5.5 Concluding Remarks

The FC-72 subcooled flow boiling heat transfer performance and associated bubble characteristics on a heated micro-pin-finned silicon chip flush mounted onto the bottom of a rectangular channel have been investigated experimentally. The effects of

the coolant mass flux, inlet liquid subcooling, and surface micro-structures of the chip on the subcooled flow boiling heat transfer coefficients and associated bubble characteristics such as the mean bubble departure diameter, bubble departure frequency, and active nucleation site density have been examined in detail. Furthermore, empirical equations to correlate the measured subcooled flow boiling heat transfer coefficient, mean bubble departure diameter, mean bubble departure frequency, and mean active nucleation site density are proposed. Major results obtained here can be summarized as follows:

(1) Increases in the coolant mass flux and inlet liquid subcooling delay the boiling incipience to higher surface heat flux. The temperature of chip surface is lowered by increasing the coolant mass flux and inlet liquid subcooling in single-phase region, but it is affected slightly in the two-phase subcooled flow boiling region. Besides, adding the micro-pin-fins to the chips can effectively lower the temperature of chip surface in both single-phase and two-phase regions.

(2) The mass flux shows little influence on the subcooled flow boiling heat transfer coefficient. An increase in the inlet liquid subcooling results in a slight reduction in the subcooled flow boiling heat transfer coefficient. Besides, the boiling heat transfer coefficient increases substantially with the imposed heat flux. Furthermore, the addition of micro-pin-fins to the chip is also beneficial in enhancing the single-phase and two-phase heat transfer.

(3) Mean bubble departure diameter is reduced at increasing coolant mass flux and inlet liquid subcooling. Besides, the higher imposed heat flux results in a larger bubble departure diameter but the smaller mean bubble departure diameter is found on pin-finned surfaces due to the partial flow acceleration effect when the coolant passes through the space between the adjacent fins.

(4) Bubble departure frequency increases with the coolant mass flux and imposed

heat flux. However, at a higher inlet liquid subcooling the bubble departure frequency is lower. On the other hand, higher bubble departure frequency is noted on the pin-finned surfaces.

(5) Active nucleation site density is less for higher coolant mass flux and inlet liquid subcooling. However, the opposite is the case for a higher imposed heat flux and for the chip with micro-pin-fin structures.

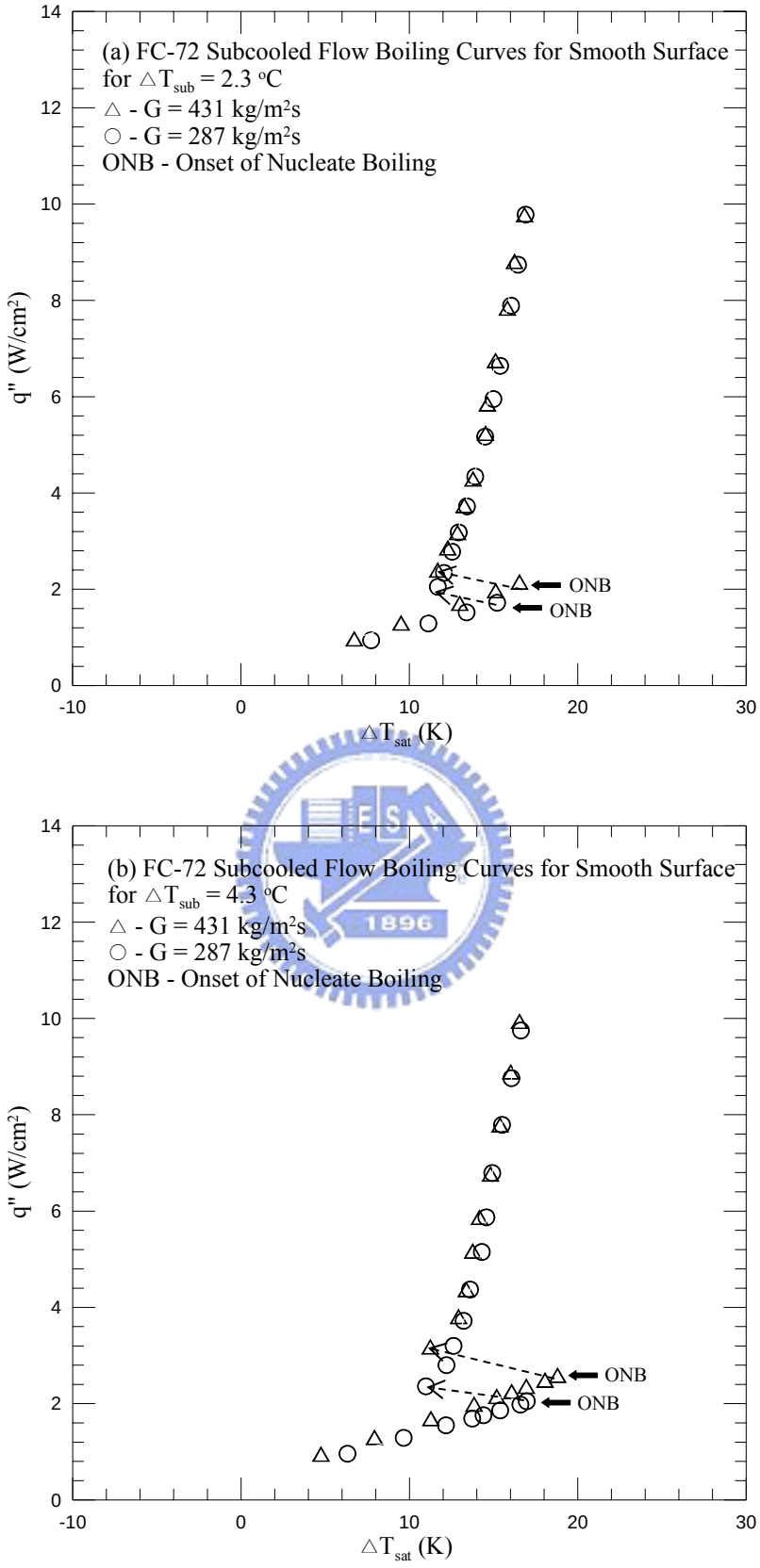

Fig 5.1 Boiling curves for the chip with smooth surface for various coolant mass fluxes at (a) $\Delta T_{sub} = 2.3\ ^{o}C$ and (b) $\Delta T_{sub} = 4.3\ ^{o}C$

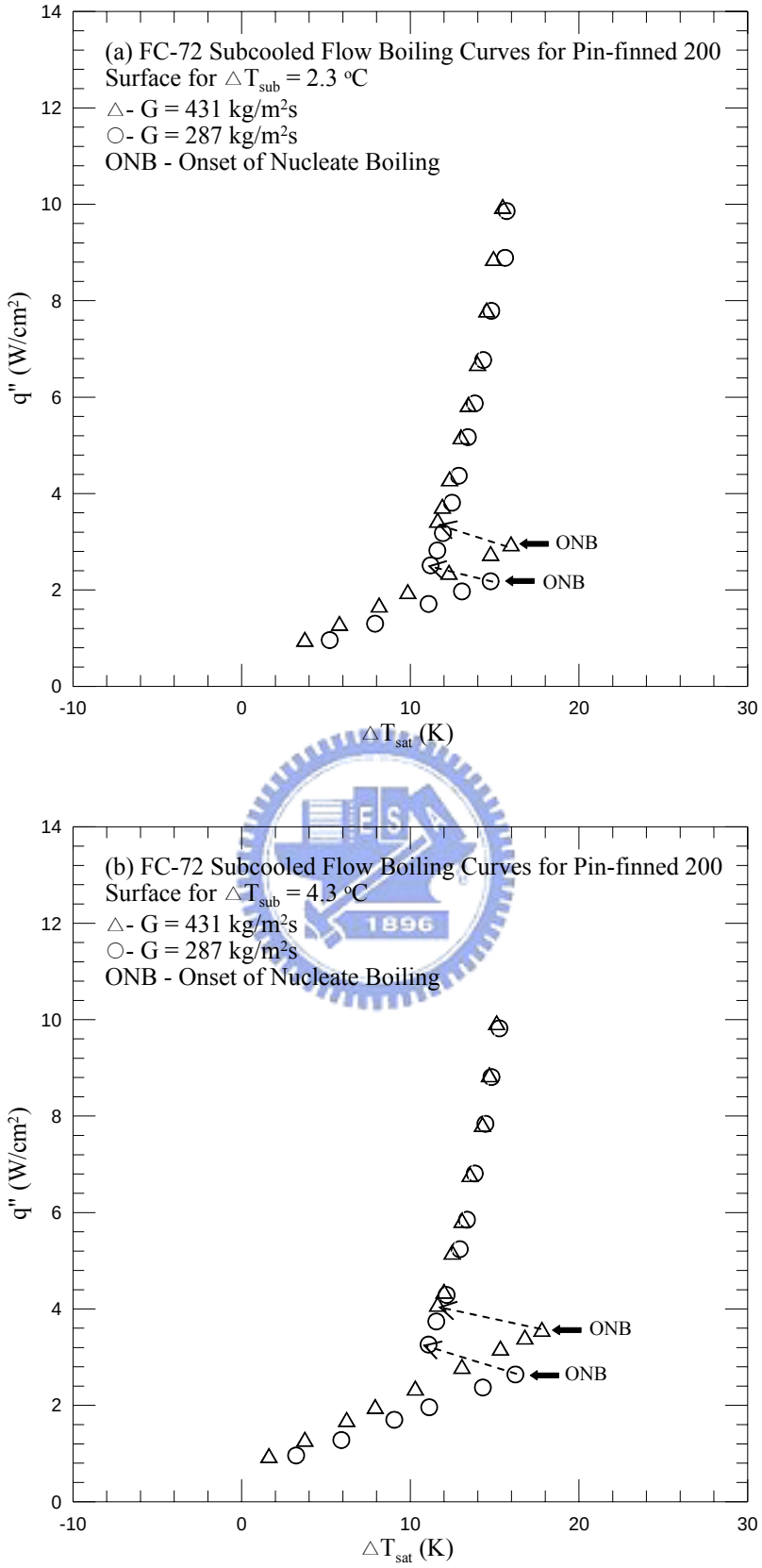

Fig. 5.2 Boiling curves for the chip with pin-finned 200 surface for various coolant mass fluxes at (a) $\Delta T_{sub} = 2.3\ ^{o}C$ and (b) $\Delta T_{sub} = 4.3\ ^{o}C$

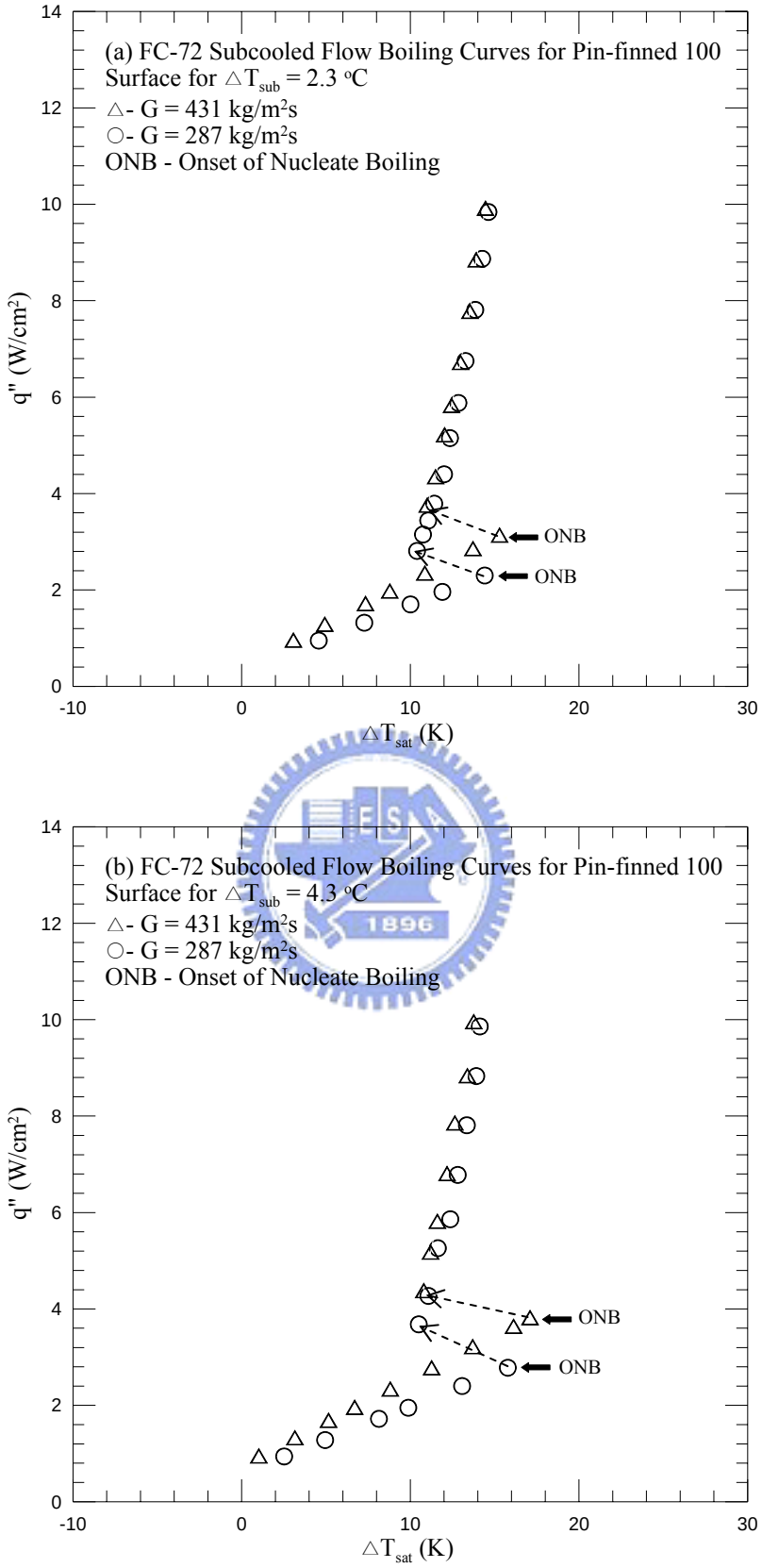

Fig. 5.3 Boiling curves for the chip with pin-finned 100 surface for various coolant mass fluxes at (a) $\Delta T_{sub} = 2.3\ ^{o}C$ and (b) $\Delta T_{sub} = 4.3\ ^{o}C$

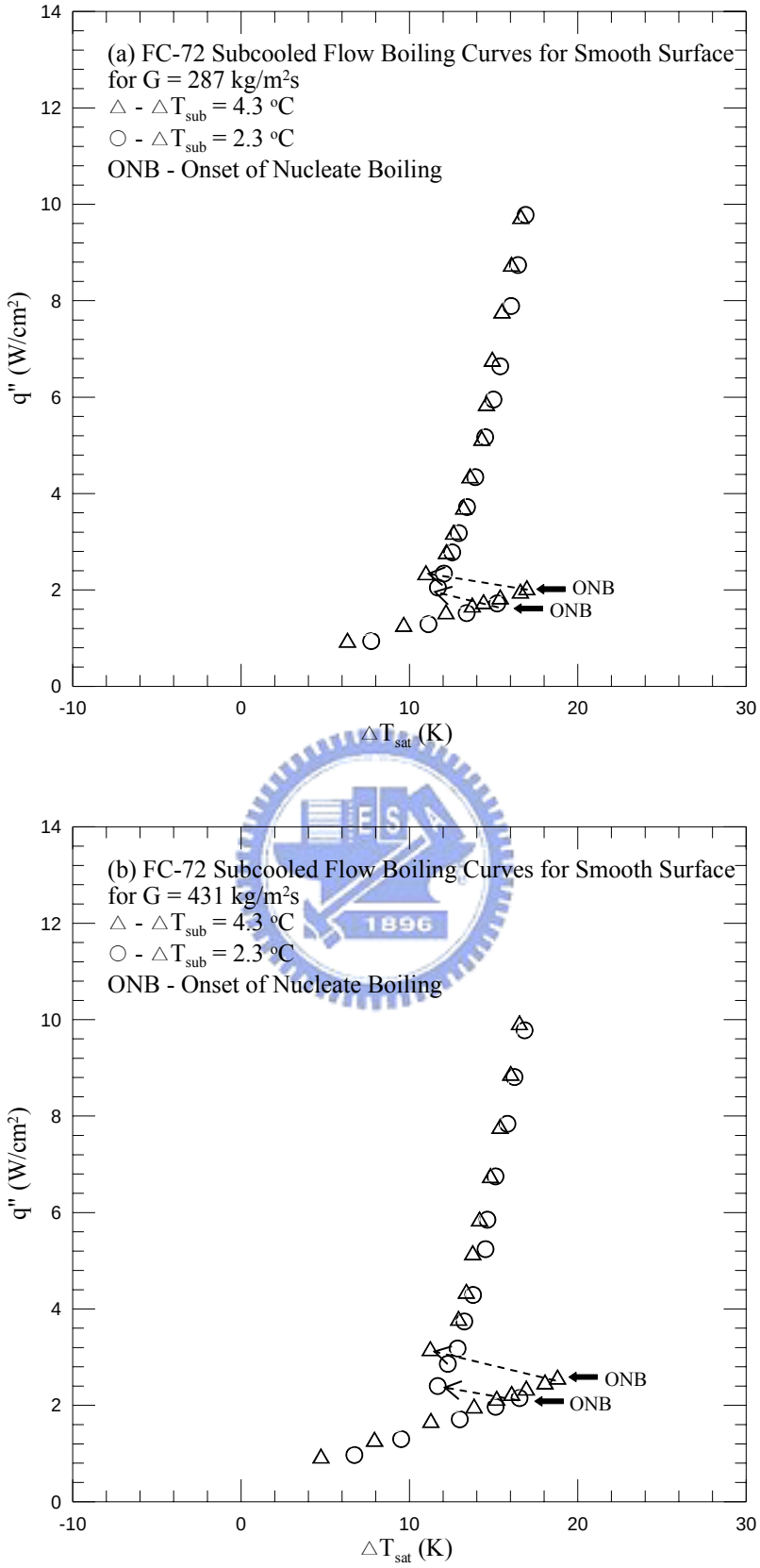

Fig 5.4 Boiling curves for the chip with smooth surface for various inlet liquid subcoolings at (a) G = 287 kg/m^{2}s and (b) G = 431 kg/m^{2}s

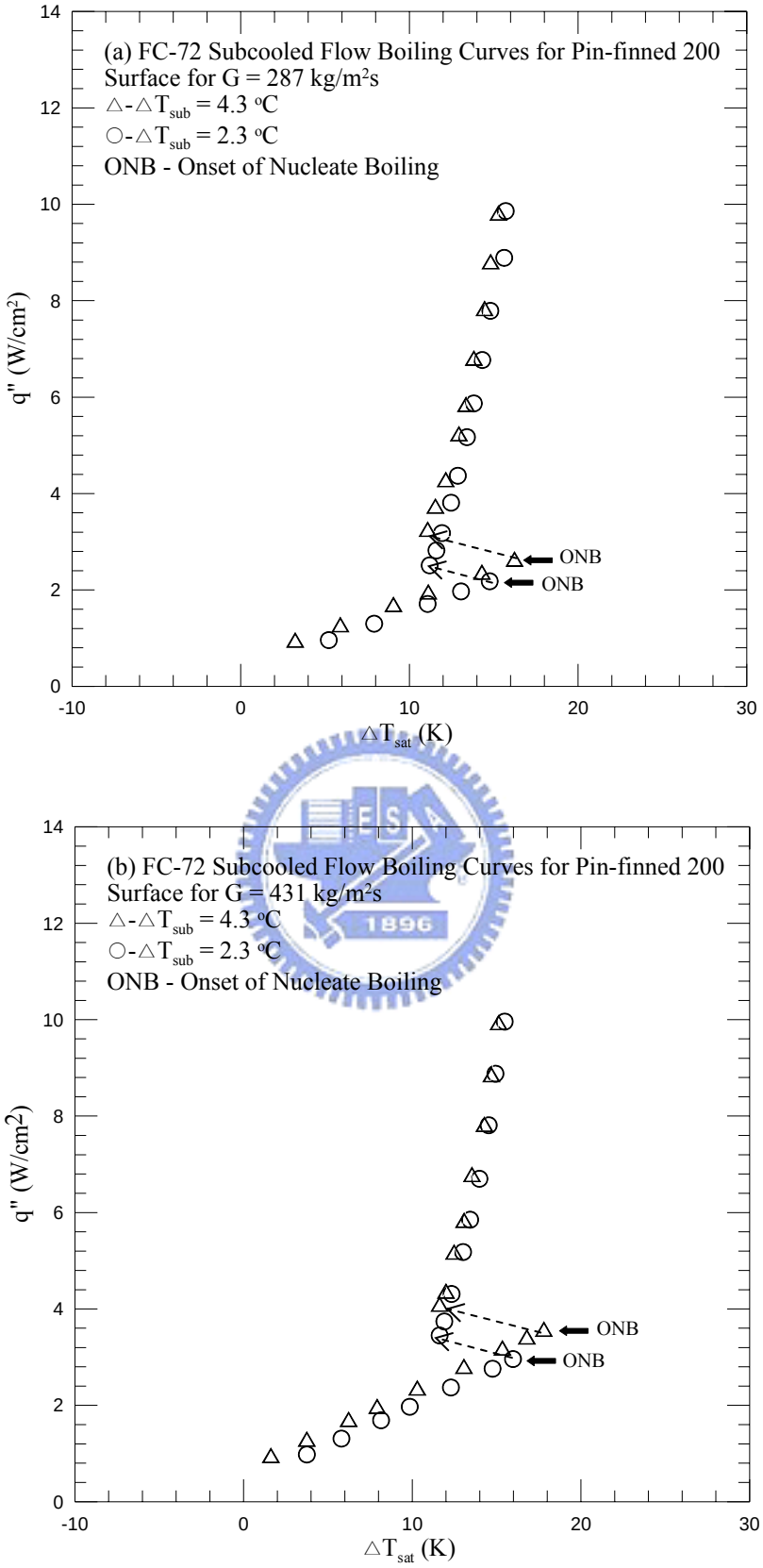

Fig. 5.5 Boiling curves for the chip with pin-finned 200 surface for various inlet liquid subcoolings at (a) G = 287 kg/m^{2}s and (b) G = 431 kg/m^{2}s

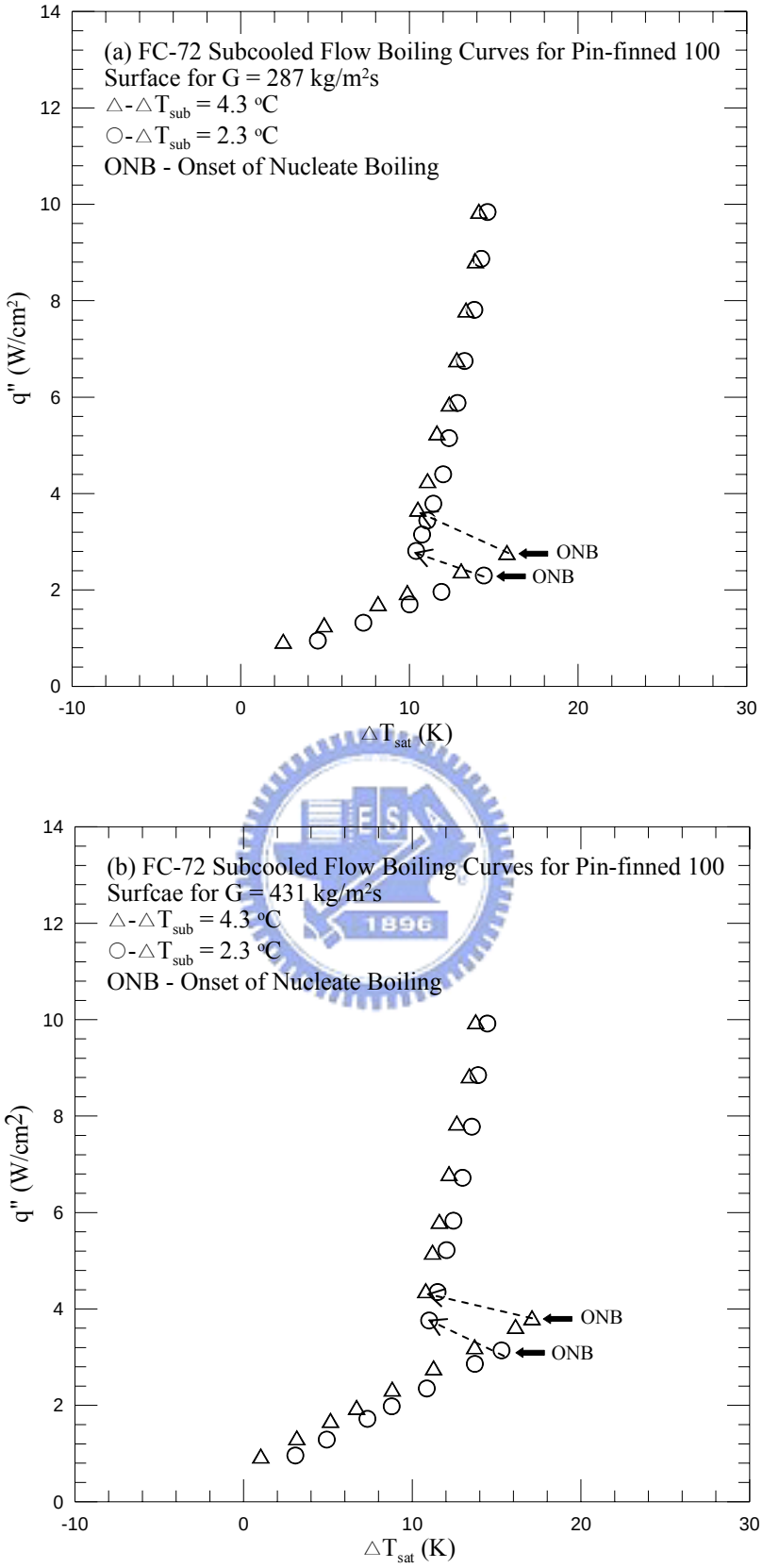

Fig. 5.6 Boiling curves for the chip with pin-finned100 surface for various inlet liquid subcoolings at (a) G = 287 kg/m^{2}s and (b) G = 431 kg/m^{2}s

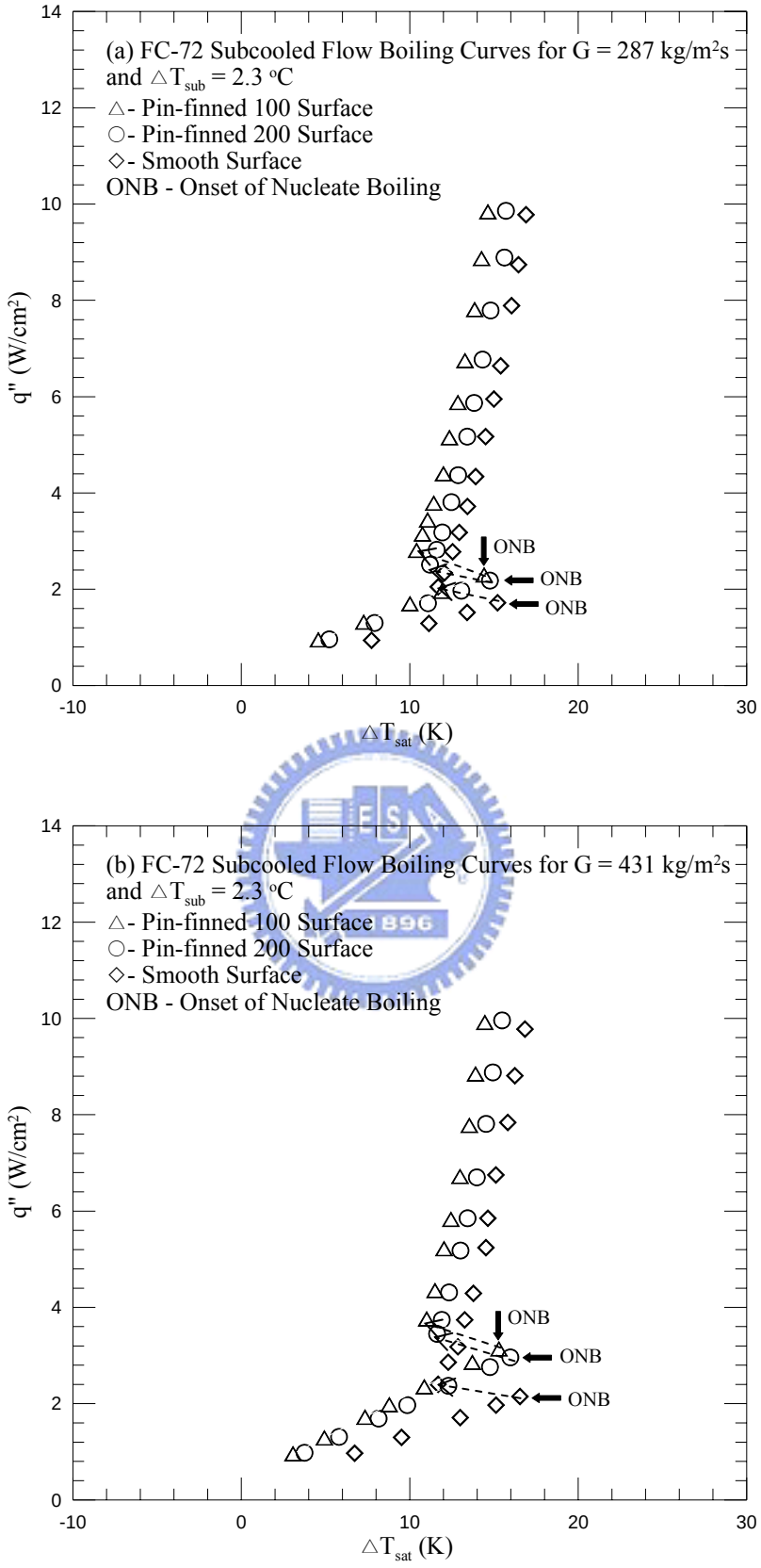

Fig. 5.7 Boiling curves affected by surface micro-structures for ΔT_{sub} = 2.3 °C at (a) G = 287 kg/m^{2}s and (b) G = 431 kg/m^{2}s

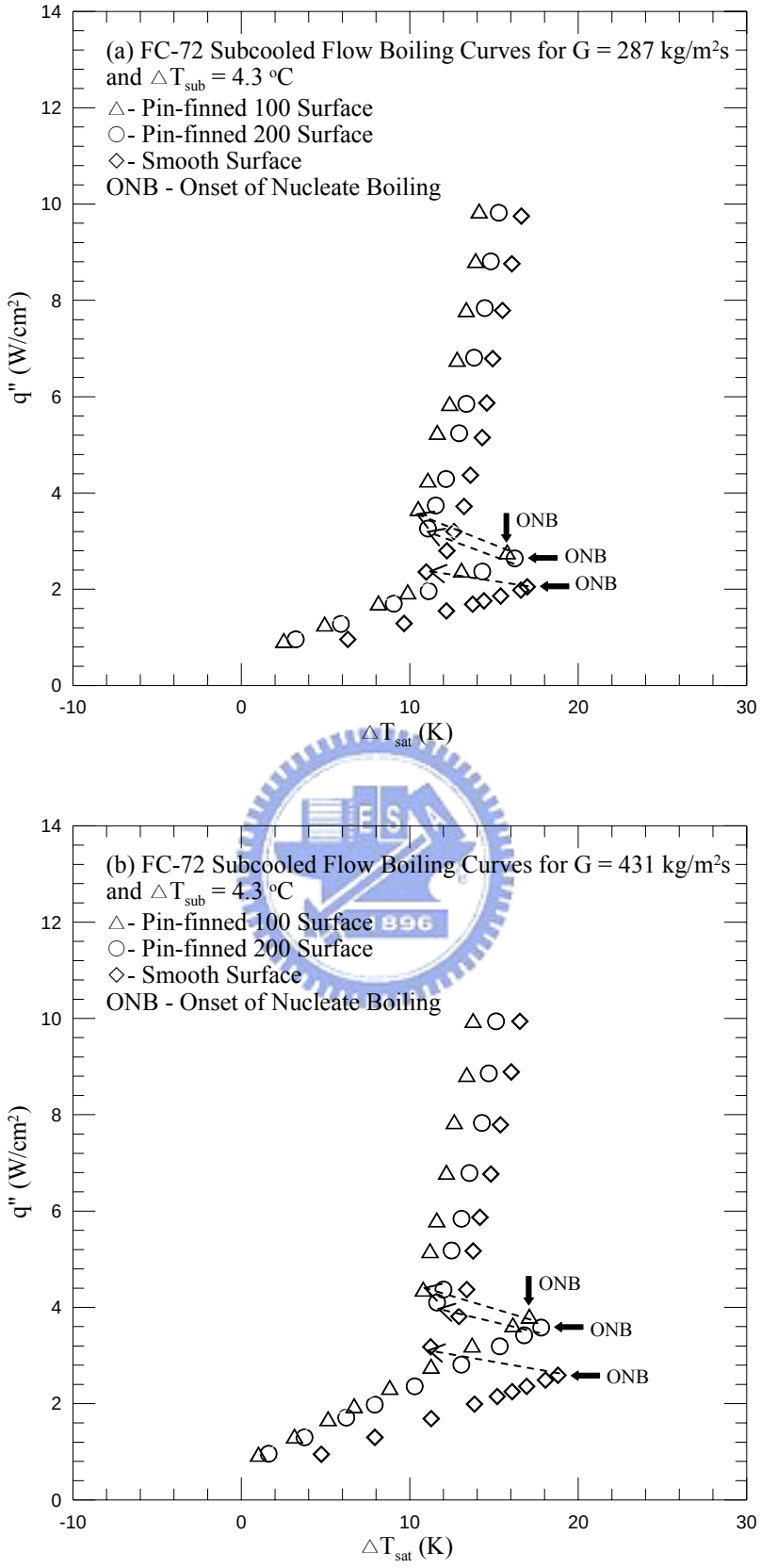

Fig. 5.8 Boiling curves affected by surface micro-structures for ΔT_{sub} = 4.3 °C at (a) G = 287 kg/m^{2}s and (b) G = 431 kg/m^{2}s

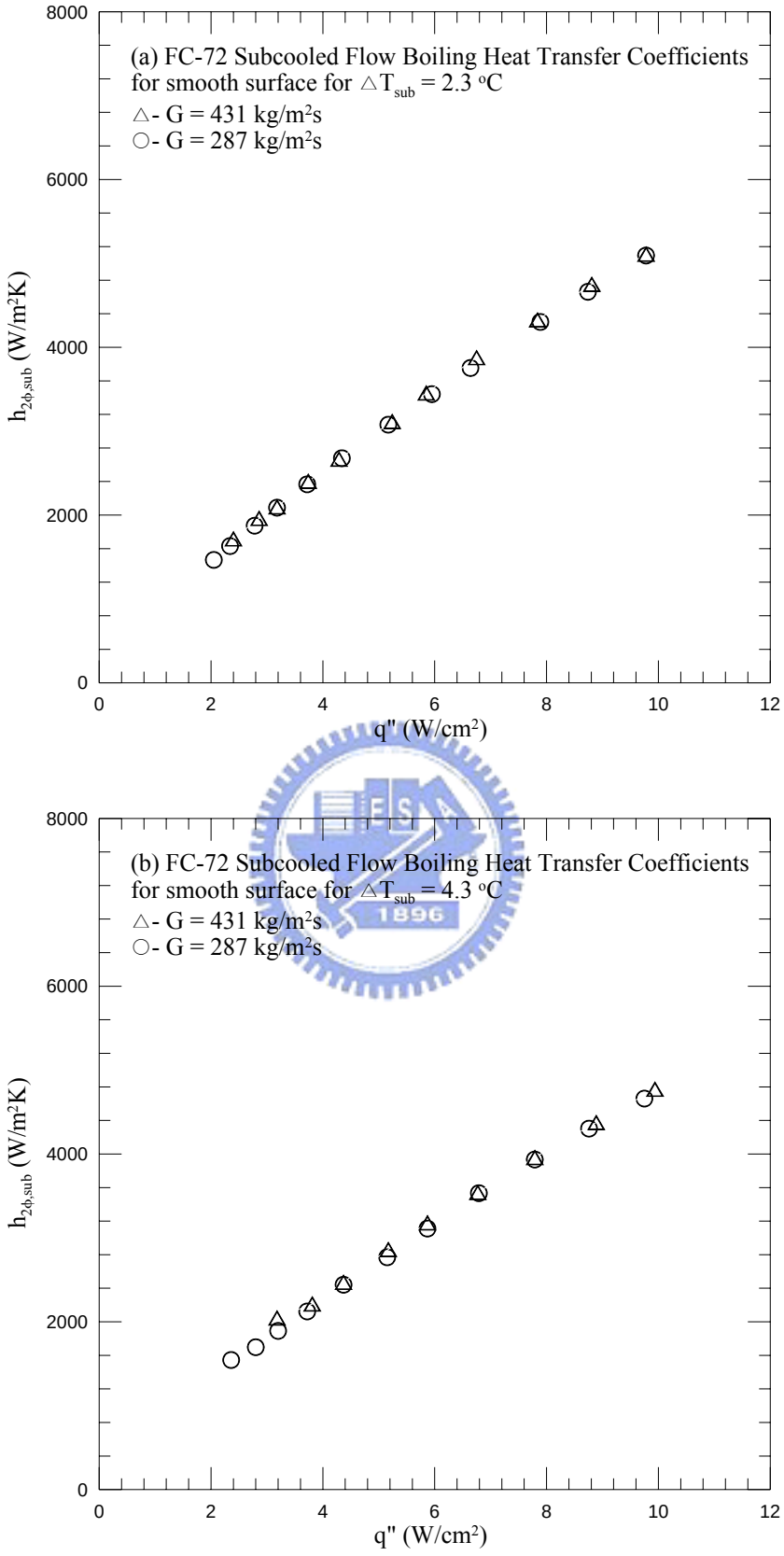

Fig. 5.9 Subcooled flow boiling heat transfer coefficients for the chip with smooth surface for various coolant mass fluxes at (a) ΔT_{sub} = 2.3 °C and (b) ΔT_{sub} = 4.3 °C

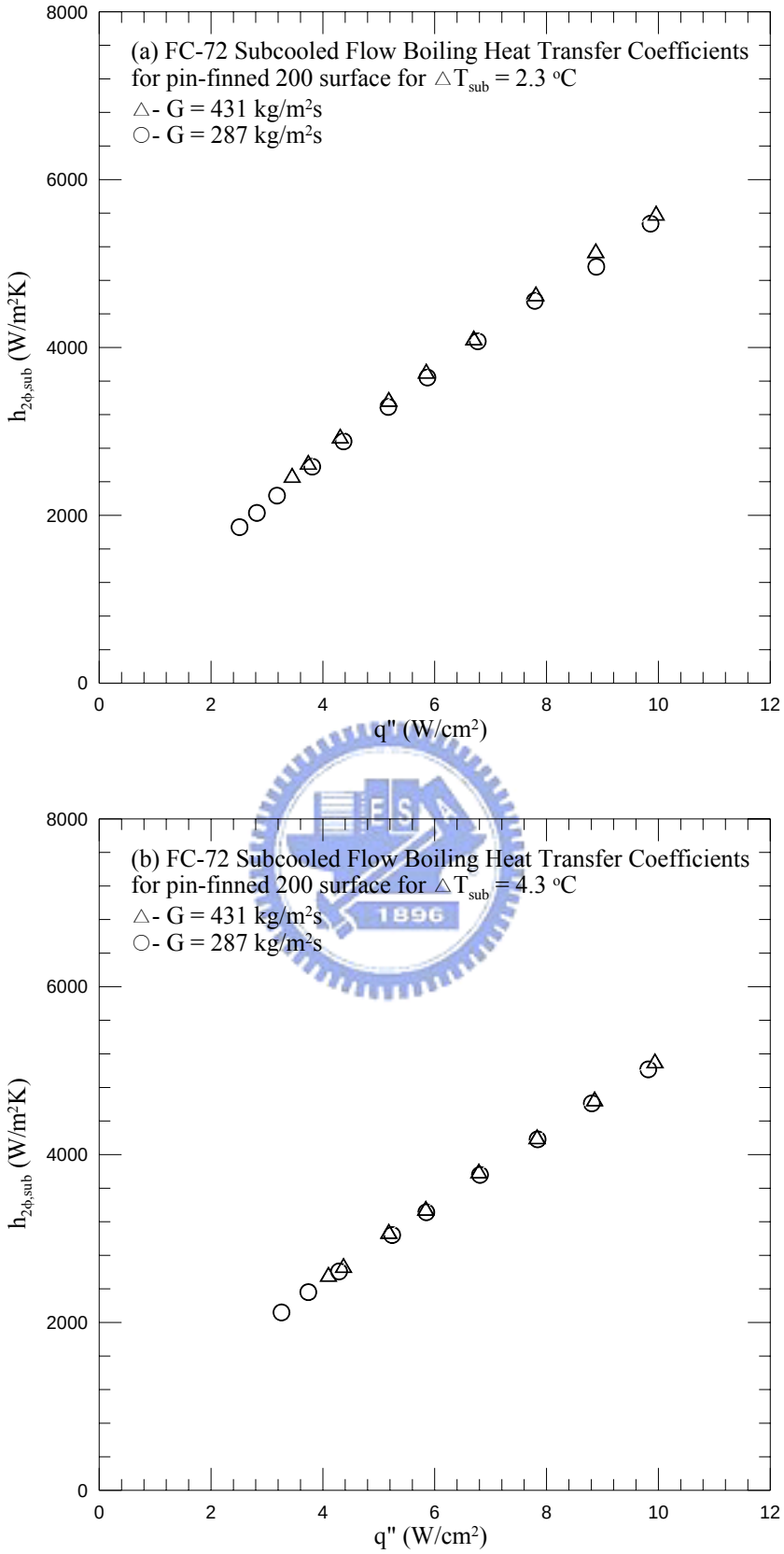

Fig. 5.10 Subcooled flow boiling heat transfer coefficients for the chip with pin-finned 200 surface for various coolant mass fluxes at (a) ΔT_{sub} = 2.3 °C and (b) ΔT_{sub} = 4.3 °C

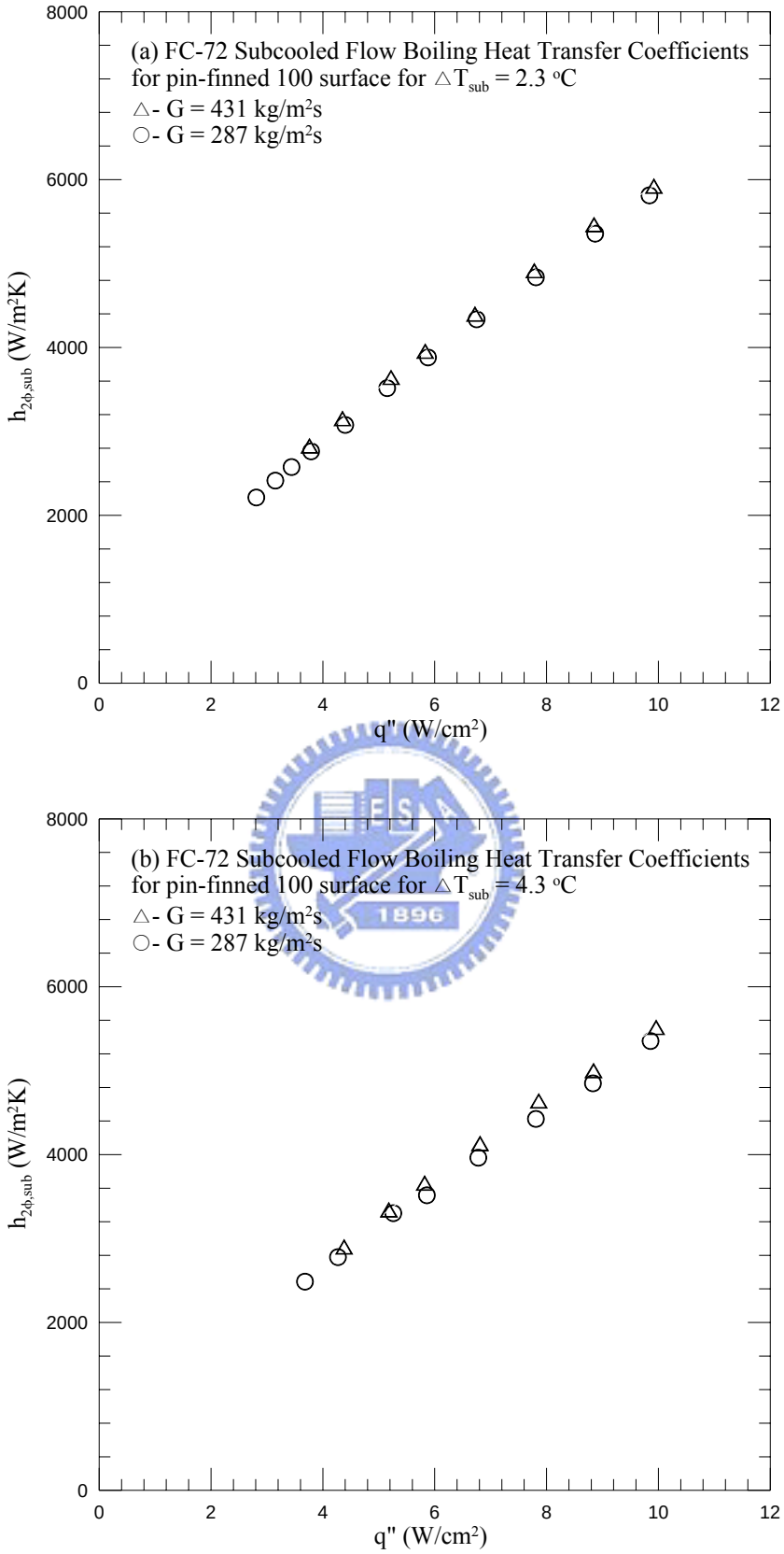

Fig. 5.11 Subcooled flow boiling heat transfer coefficients for the chip with pin-finned 100 surface for various coolant mass fluxes at (a) ΔT_{sub} = 2.3 °C and (b) ΔT_{sub} = 4.3 °C

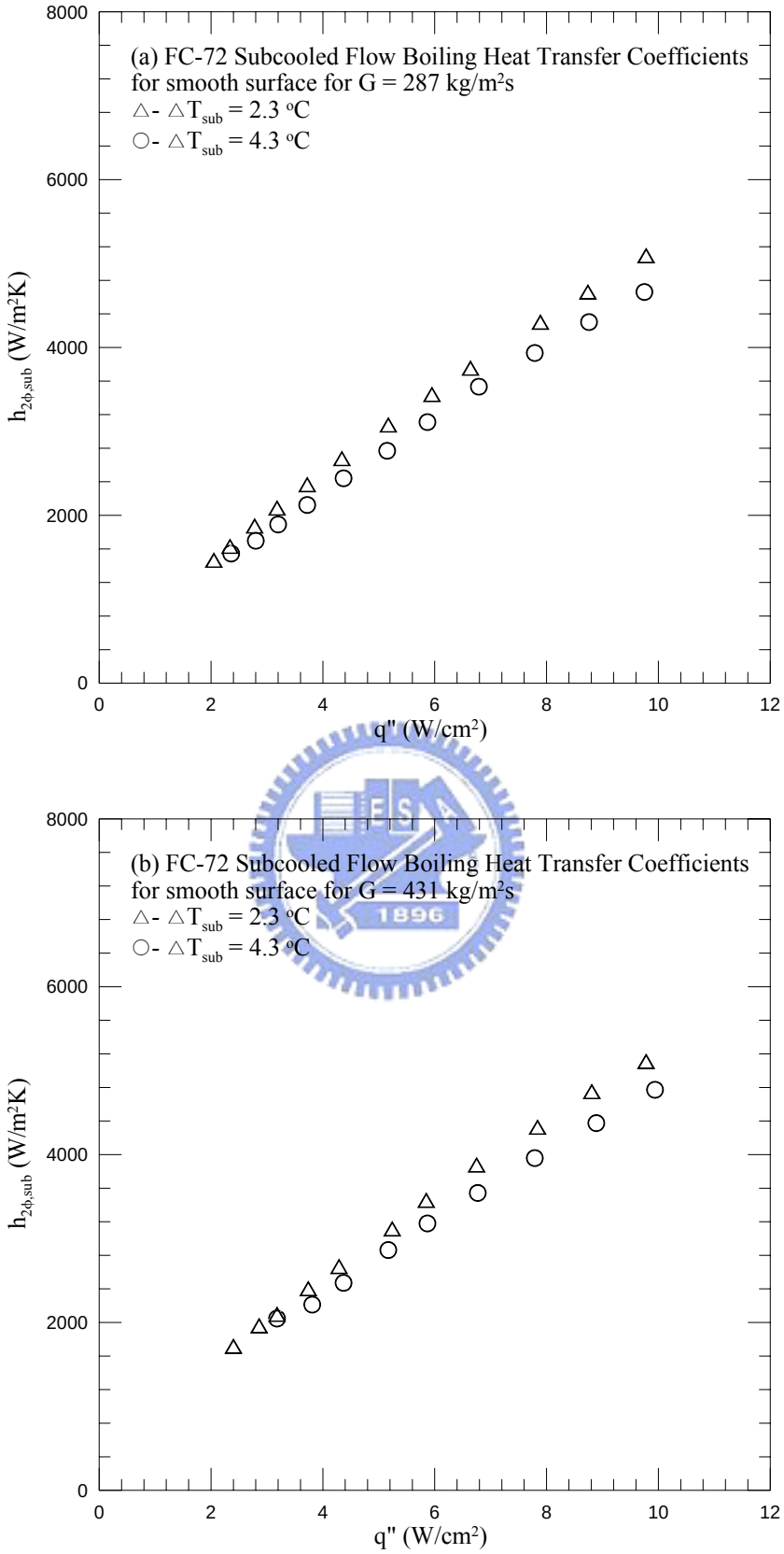

Fig. 5.12 Subcooled flow boiling heat transfer coefficients for the chip with smooth surface for various inlet liquid subcoolings at (a) G = 287 kg/m^{2}s and (b) G = 431 kg/m^{2}s

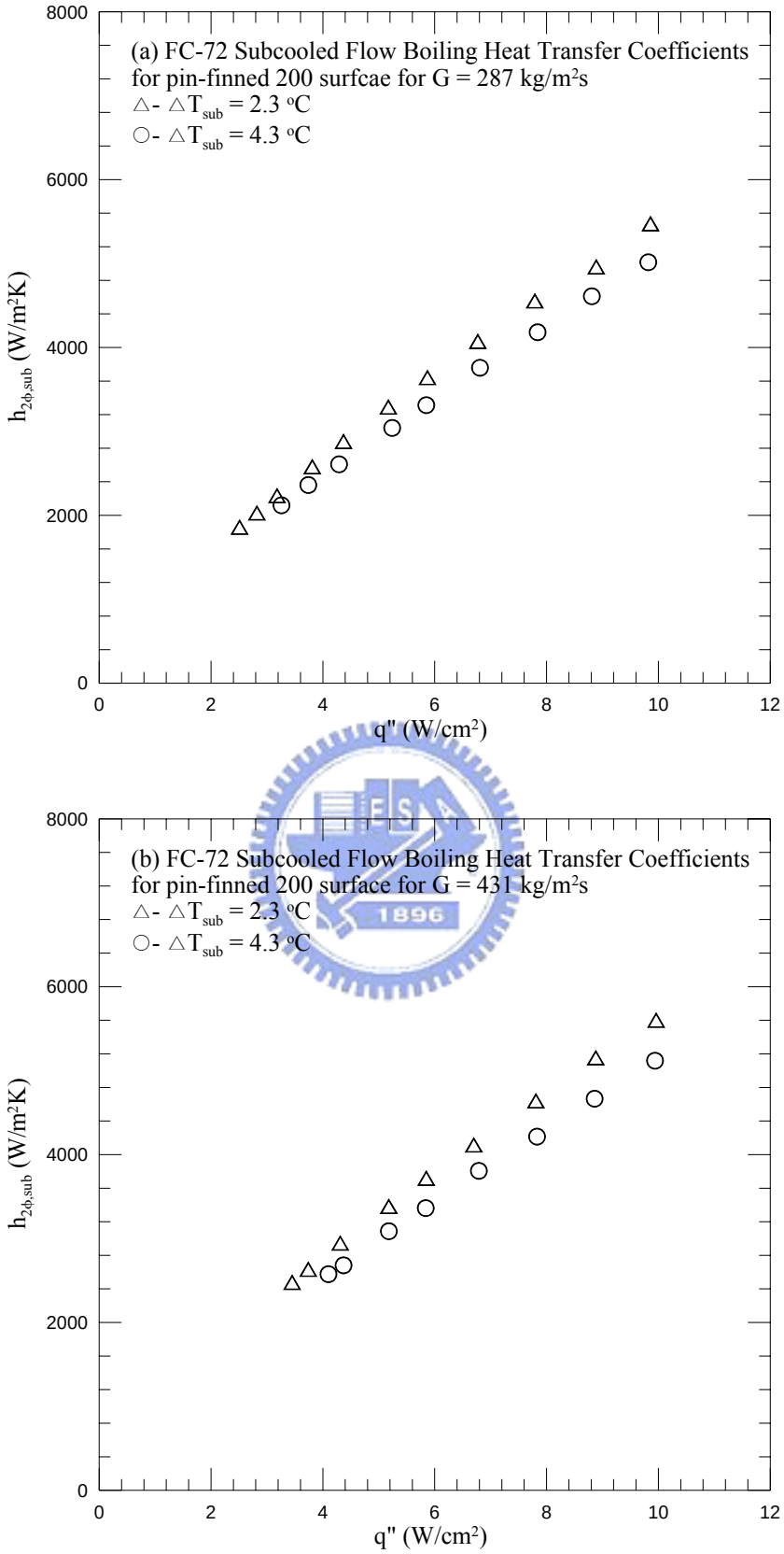

Fig. 5.13 Subcooled flow boiling heat transfer coefficients for the chip with pin-finned 200 surface for various inlet liquid subcoolings at (a) G = 287 kg/m^{2}s and (b) G = 431 kg/m^{2}s

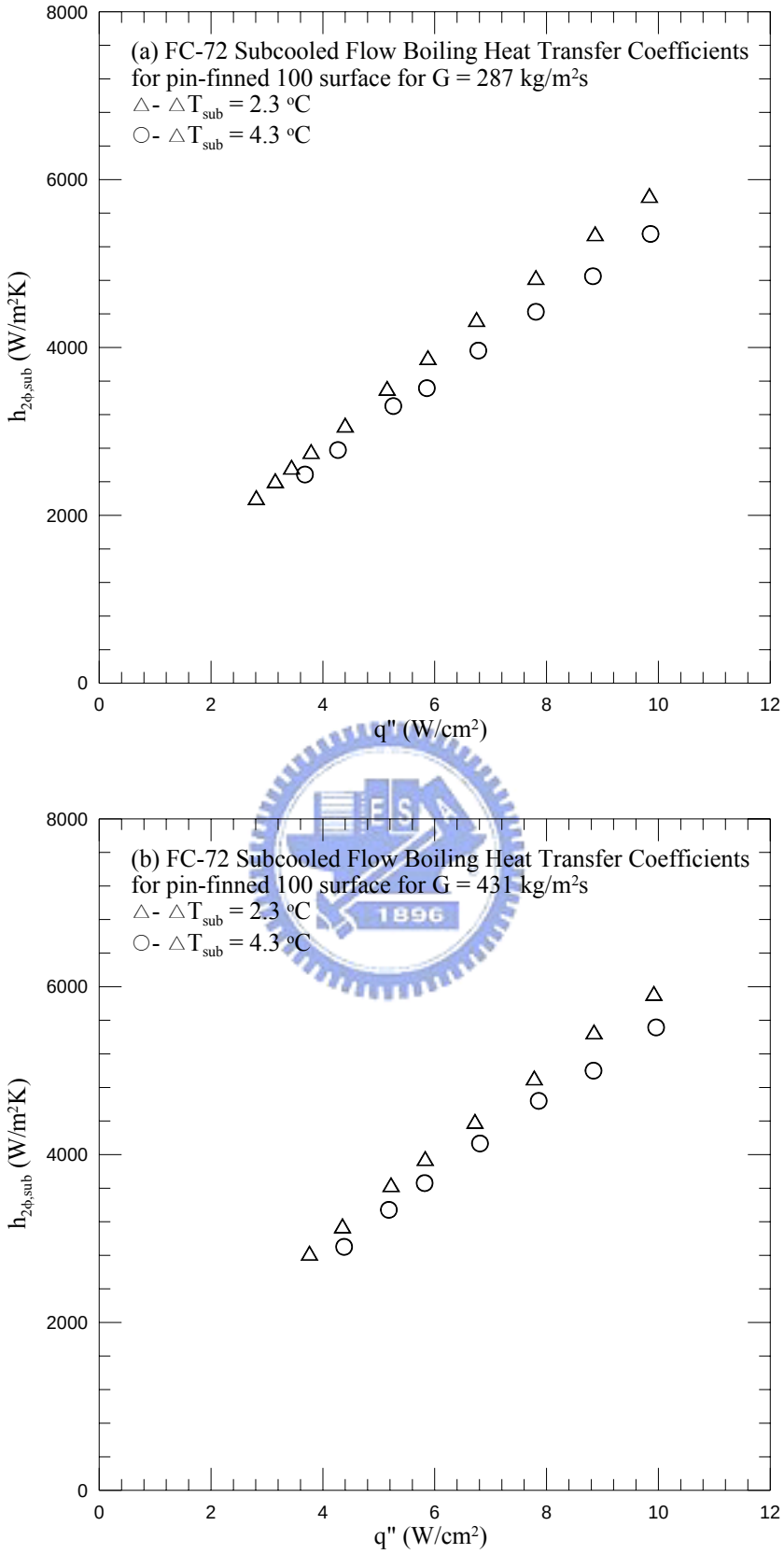

Fig. 5.14 Subcooled flow boiling heat transfer coefficients for the chip with pin-finned 100 surface for various inlet liquid subcoolings at (a) G = 287 kg/m^{2}s and (b) G = 431 kg/m^{2}s

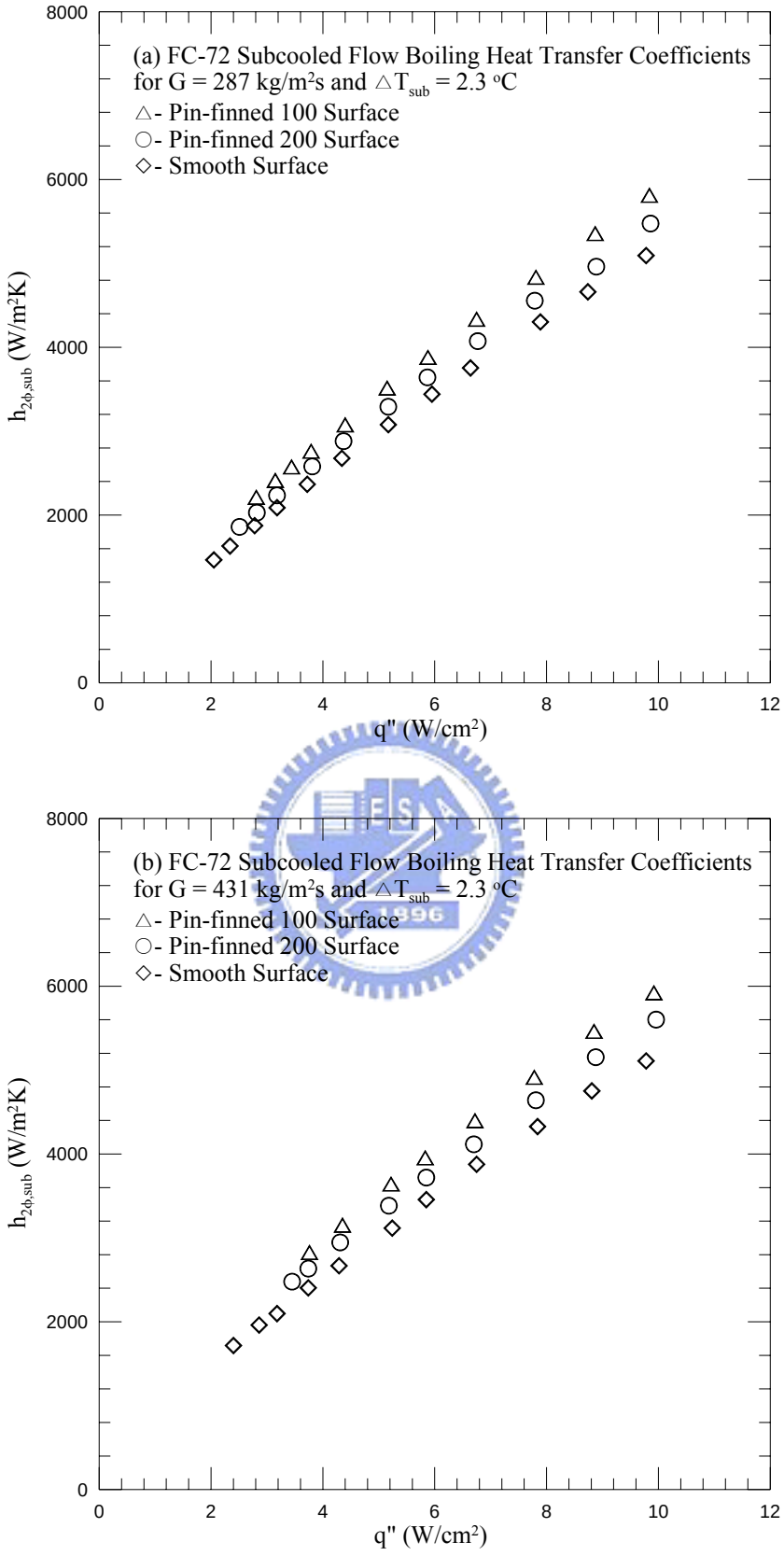

Fig. 5.15 Subcooled flow boiling heat transfer coefficients affected by surface micro-structures for ΔT_{sub} = 2.3 °C at (a) G = 287 kg/m^{2}s and (b) G = 431 kg/m^{2}s

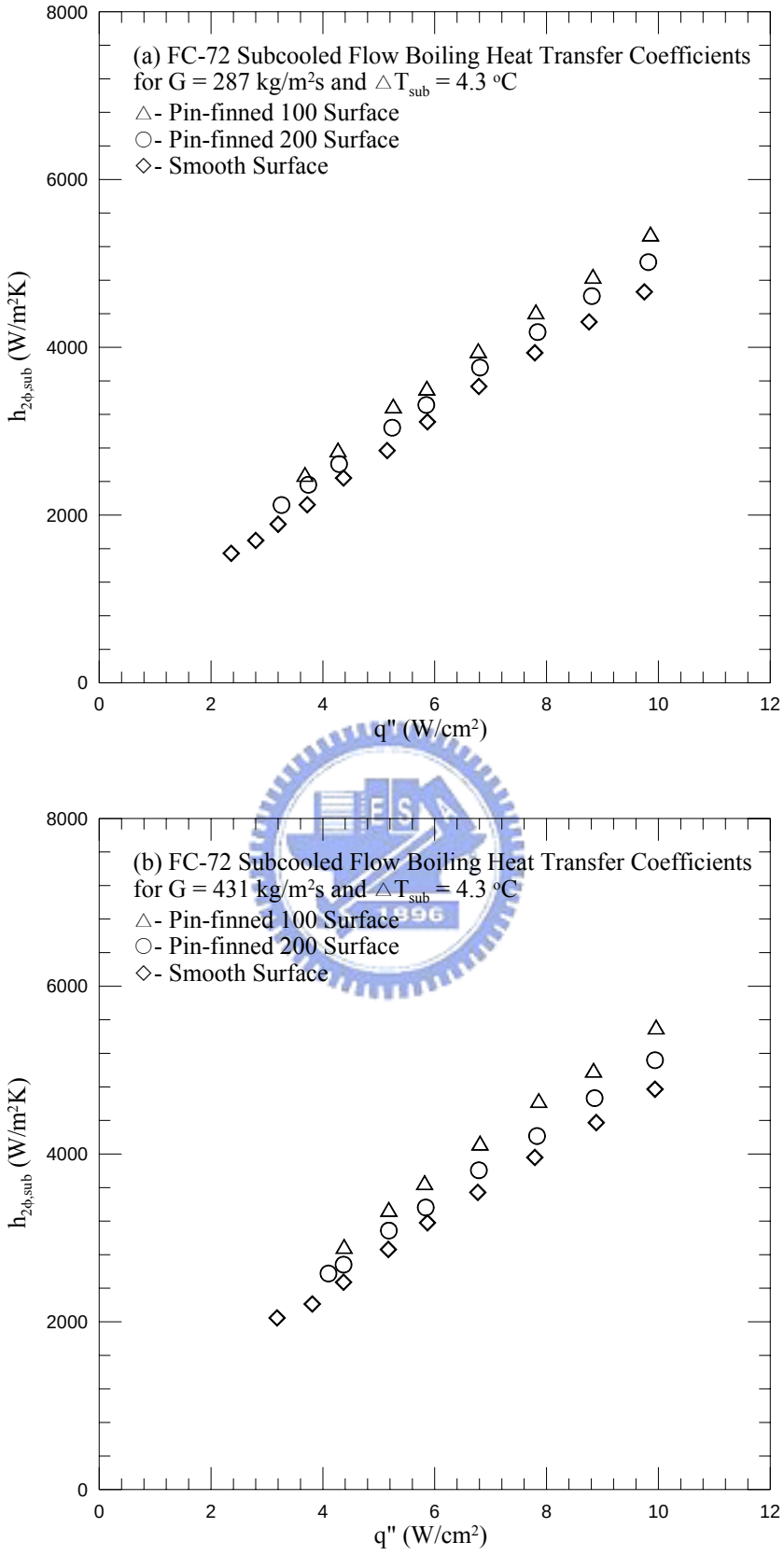

Fig. 5.16 Subcooled flow boiling heat transfer coefficients affected by surface micro-structures for ΔT_{sub} = 4.3 °C at (a) G = 287 kg/m^{2}s and (b) G = 431 kg/m^{2}s

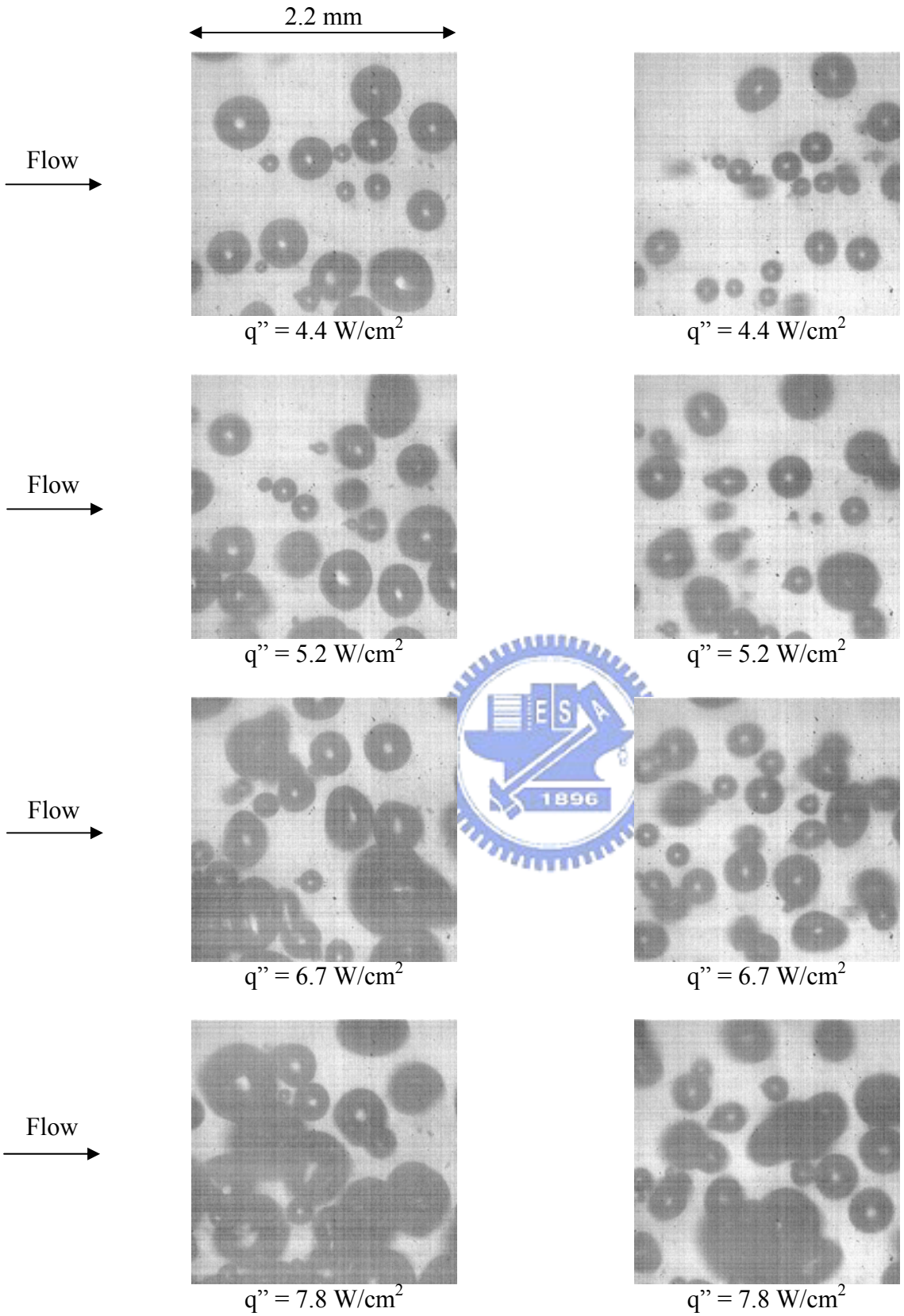

Fig. 5.17 Photos of boiling flow for various imposed heat fluxes for the chip with smooth surface at ΔT_{sub} = 2.3 °C for (a) G = 287 kg/m^{2}s and (b) G = 431 kg/m^{2}s

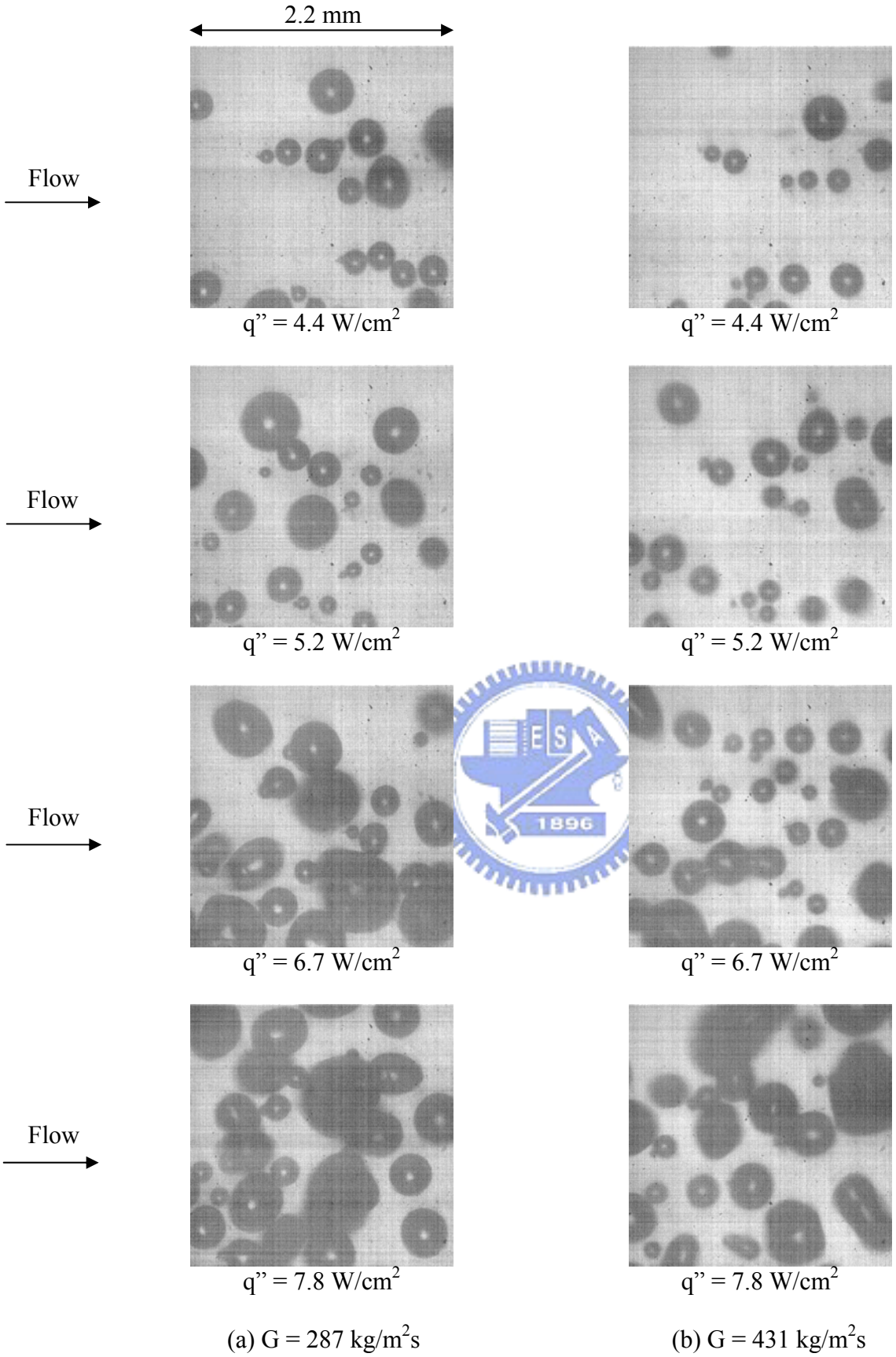

Fig. 5.18 Photos of boiling flow for various imposed heat fluxes for the chip with smooth surface at ΔT_{sub} = 4.3 ^{o}C for (a) G = 287 kg/m^{2}s and (b) G = 431 kg/m^{2}s

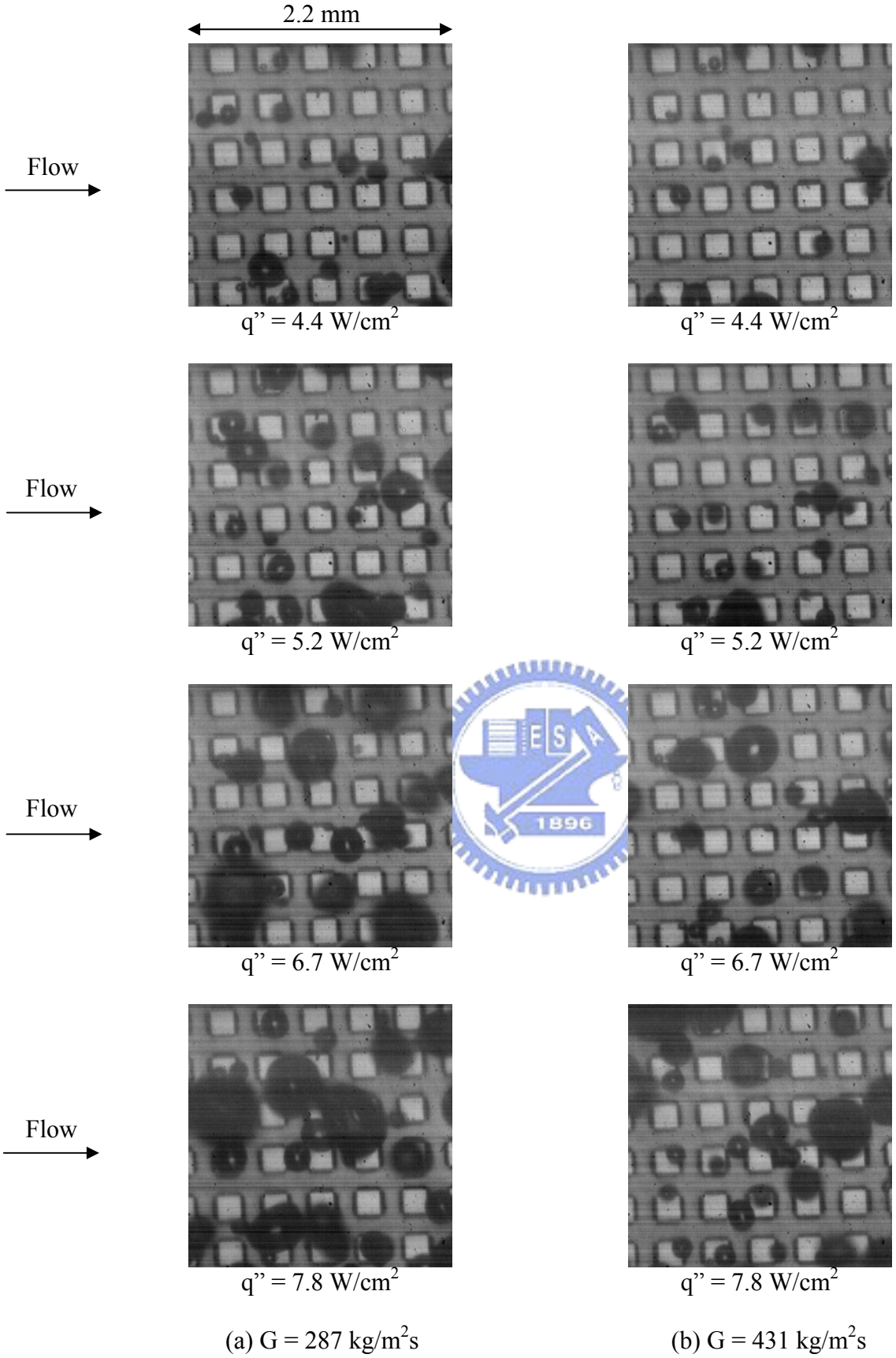

Fig. 5.19 Photos of boiling flow for various imposed heat fluxes for the chip with pin-finned 200 surface at ΔT_{sub} = 2.3 ^{o}C for (a) G = 287 kg/m^{2}s and (b) G = 431 kg/m^{2}s

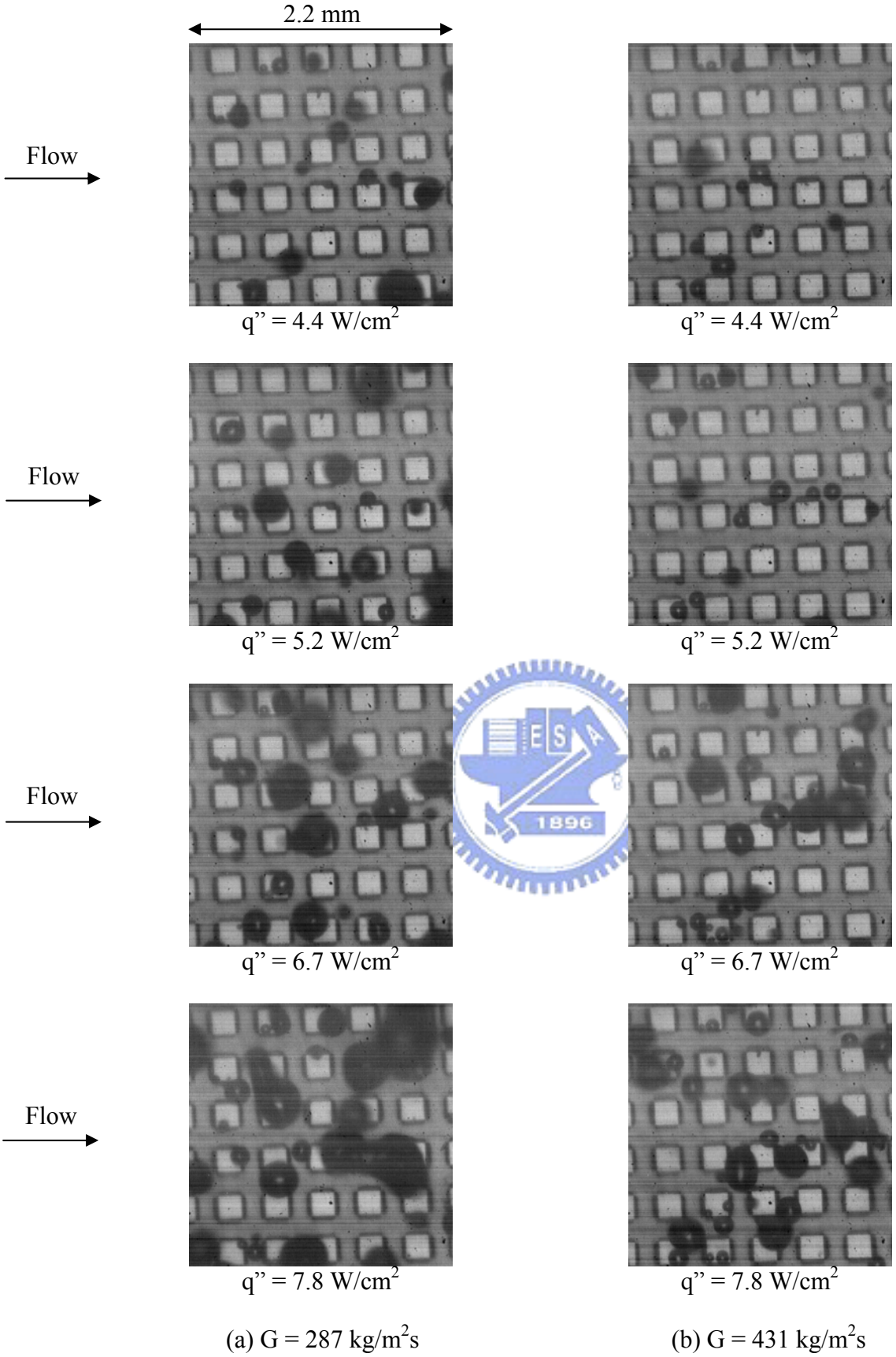

Fig. 5.20 Photos of boiling flow for various imposed heat fluxes for the chip with pin-finned 200 surface at ΔT_{sub} = 4.3 °C for (a) G = 287 kg/m^{2}s and (b) G = 431 kg/m^{2}s

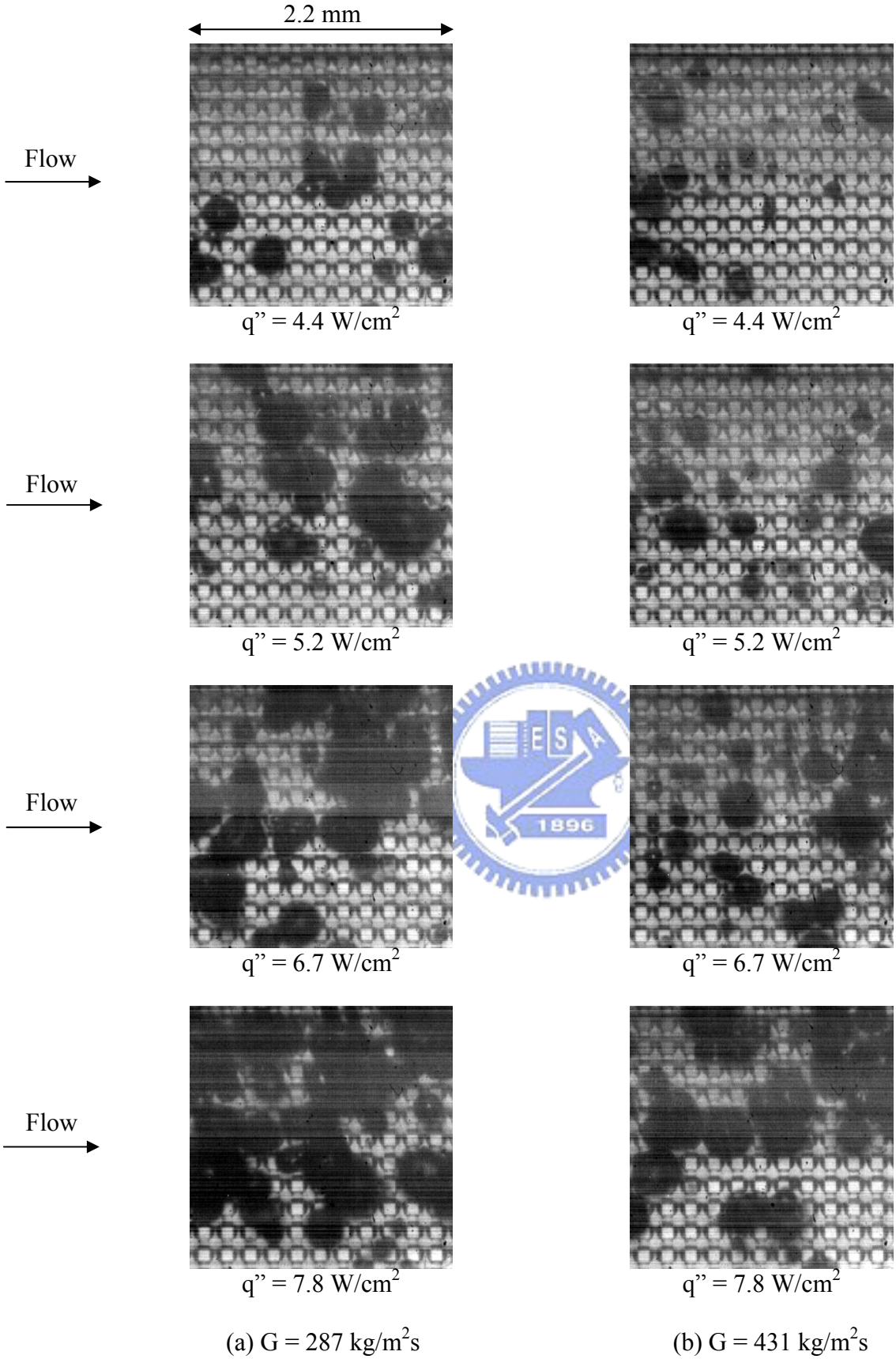

Fig 5.21 Photos of boiling flow for various imposed heat fluxes for the chip with pin-finned 100 surface at ΔT_{sub} = 2.3 °C for (a) G = 287 kg/m^{2}s and (b) G = 431 kg/m^{2}s

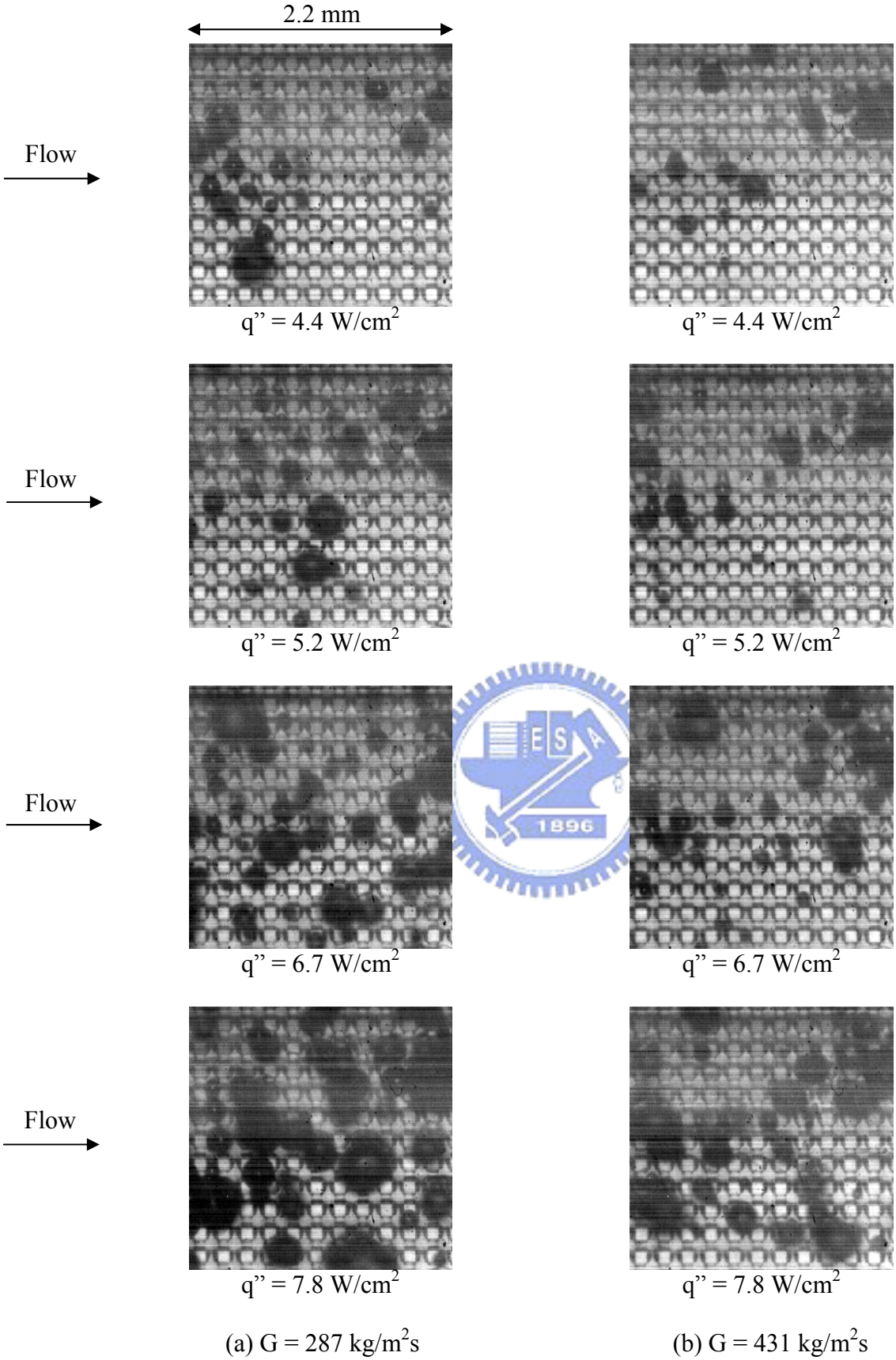

Fig 5.22 Photos of boiling flow for various imposed heat fluxes for the chip with pin-finned 100 surface at ΔT_{sub} = 4.3 ^{o}C for (a) G = 287 kg/m^{2}s and (b) G = 431 kg/m^{2}s

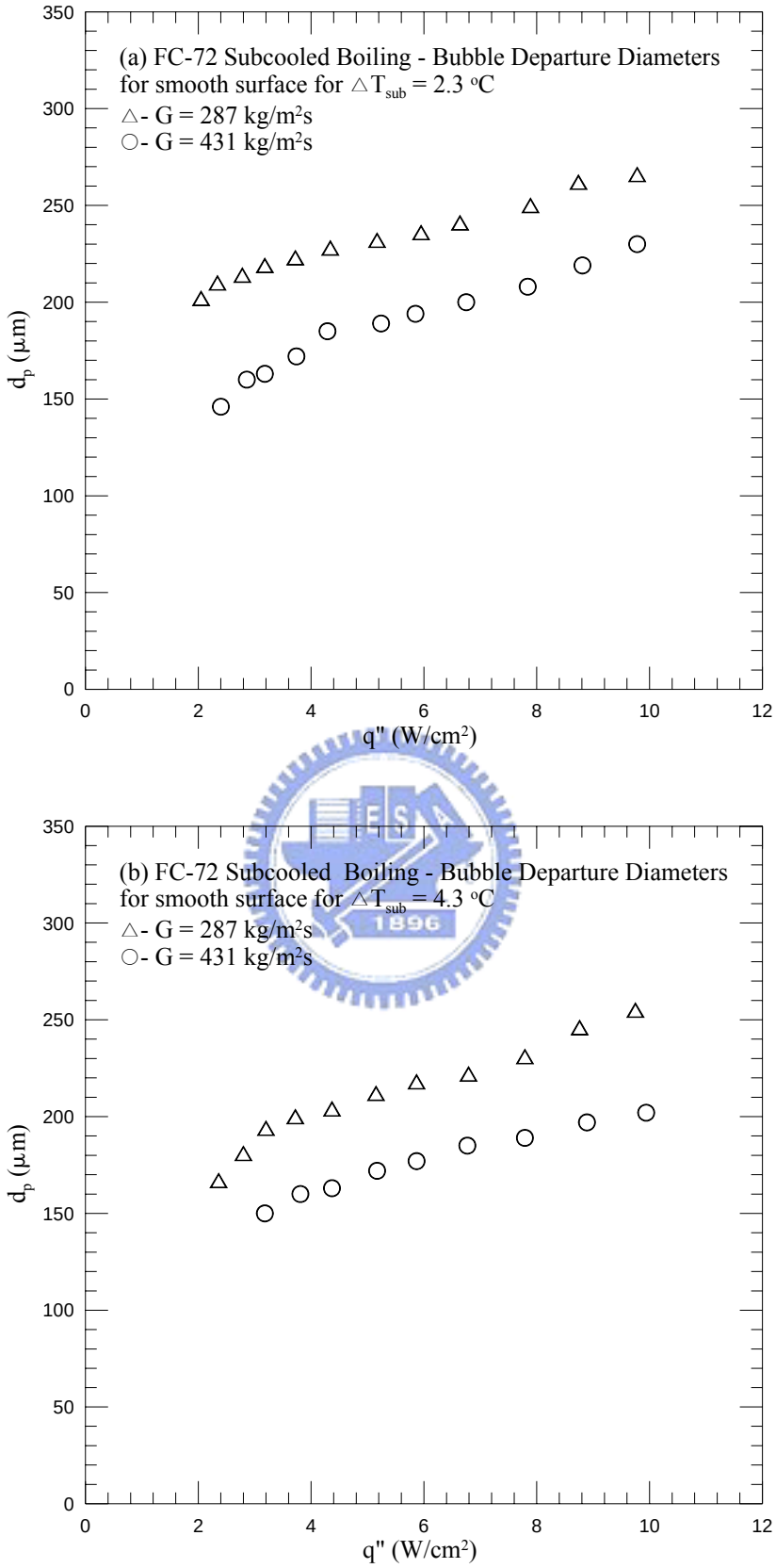

Fig. 5.23 Mean bubble departure diameters for subcooled flow boiling from smooth surface for various coolant mass fluxes at (a) ΔT_{sub} = 2.3 °C and (b) ΔT_{sub} = 4.3 °C

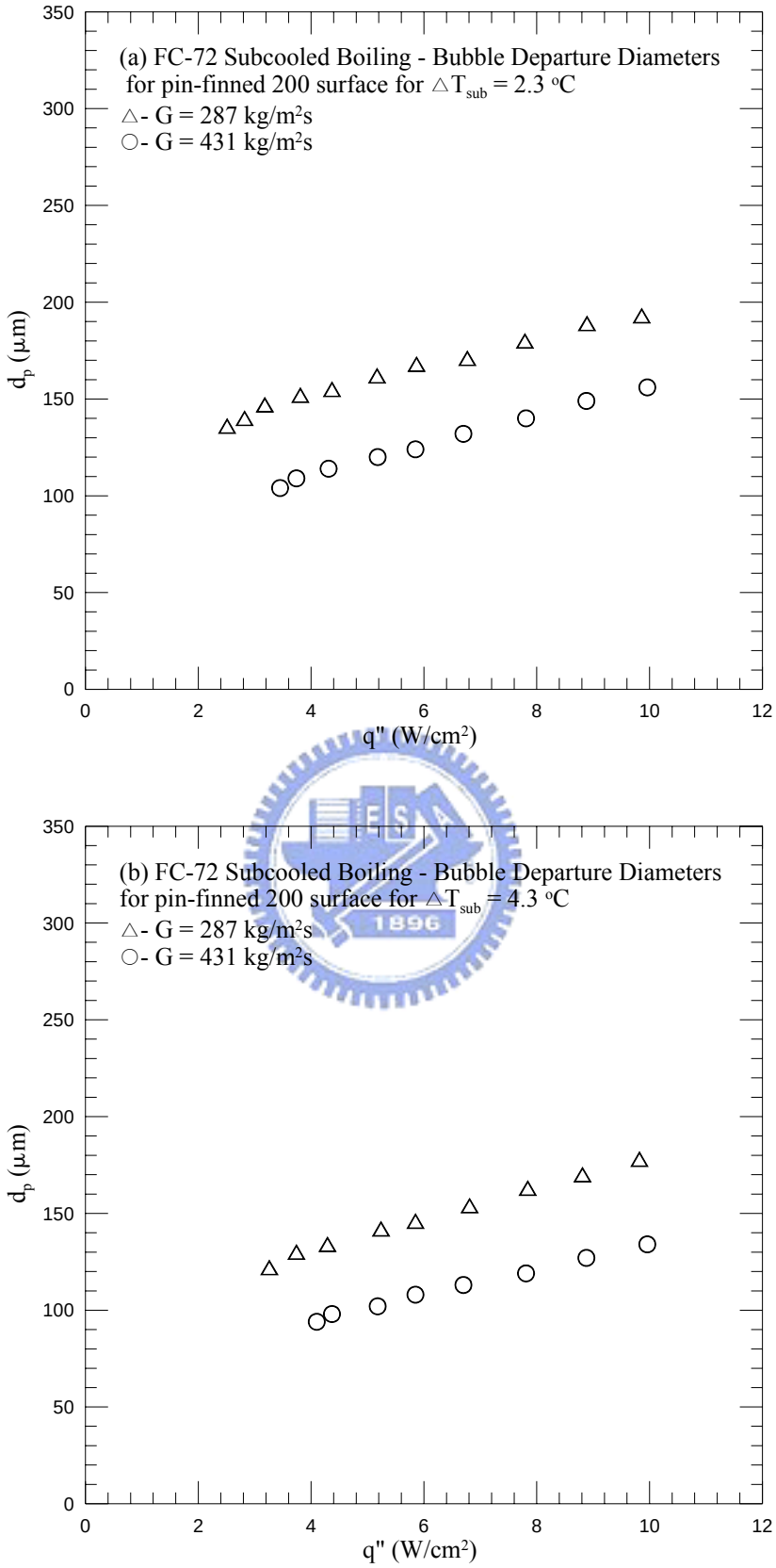

Fig. 5.24 Mean bubble departure diameters for subcooled flow boiling from pin-finned 200 surface for various coolant mass fluxes at (a) ΔT_{sub} = 2.3 °C and (b) ΔT_{sub} = 4.3 °C

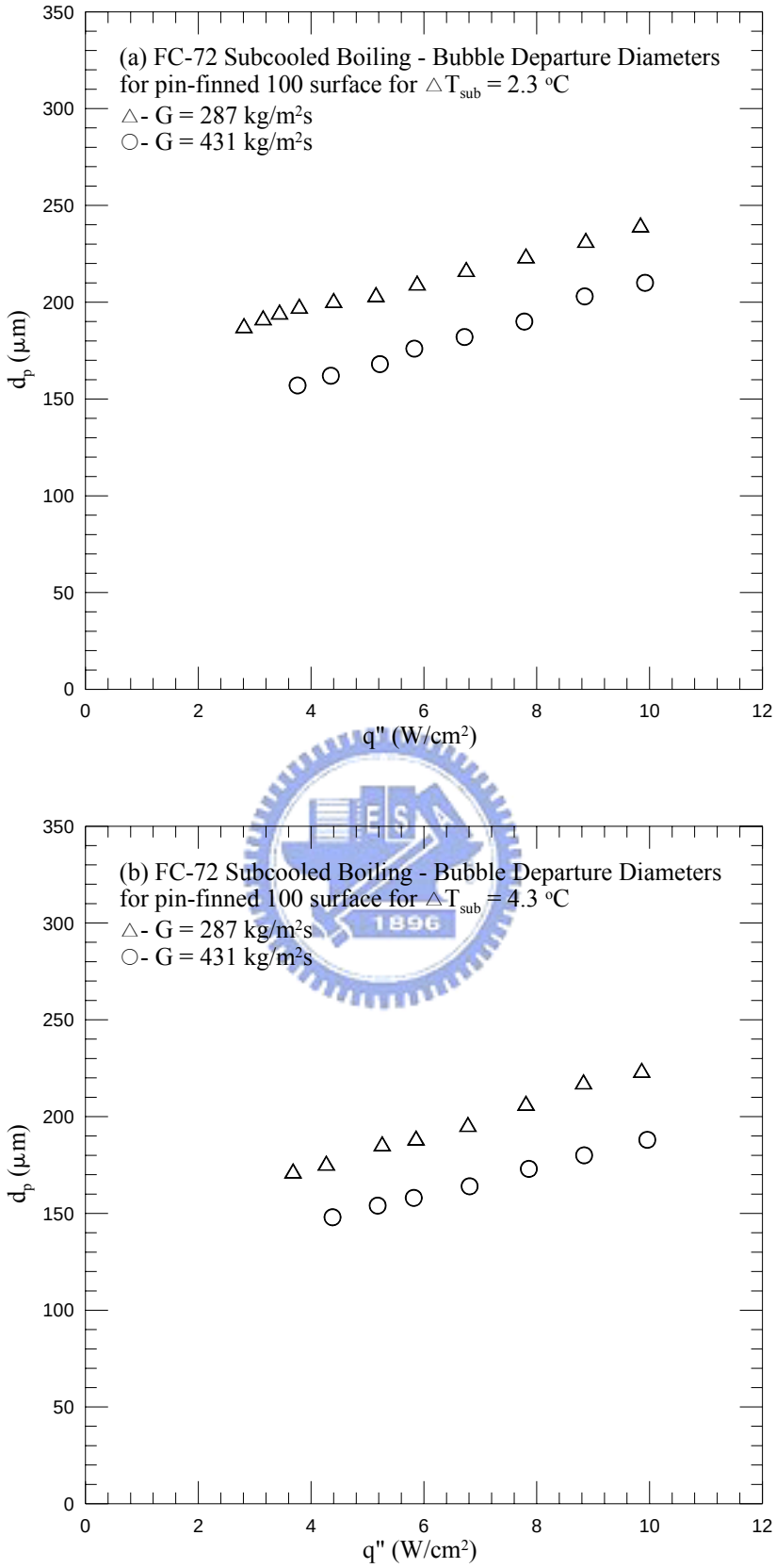

Fig. 5.25 Mean bubble departure diameters for subcooled flow boiling from pin-finned 100 surface for various coolant mass fluxes at (a) ΔT_{sub} = 2.3 °C and (b) ΔT_{sub} = 4.3 °C

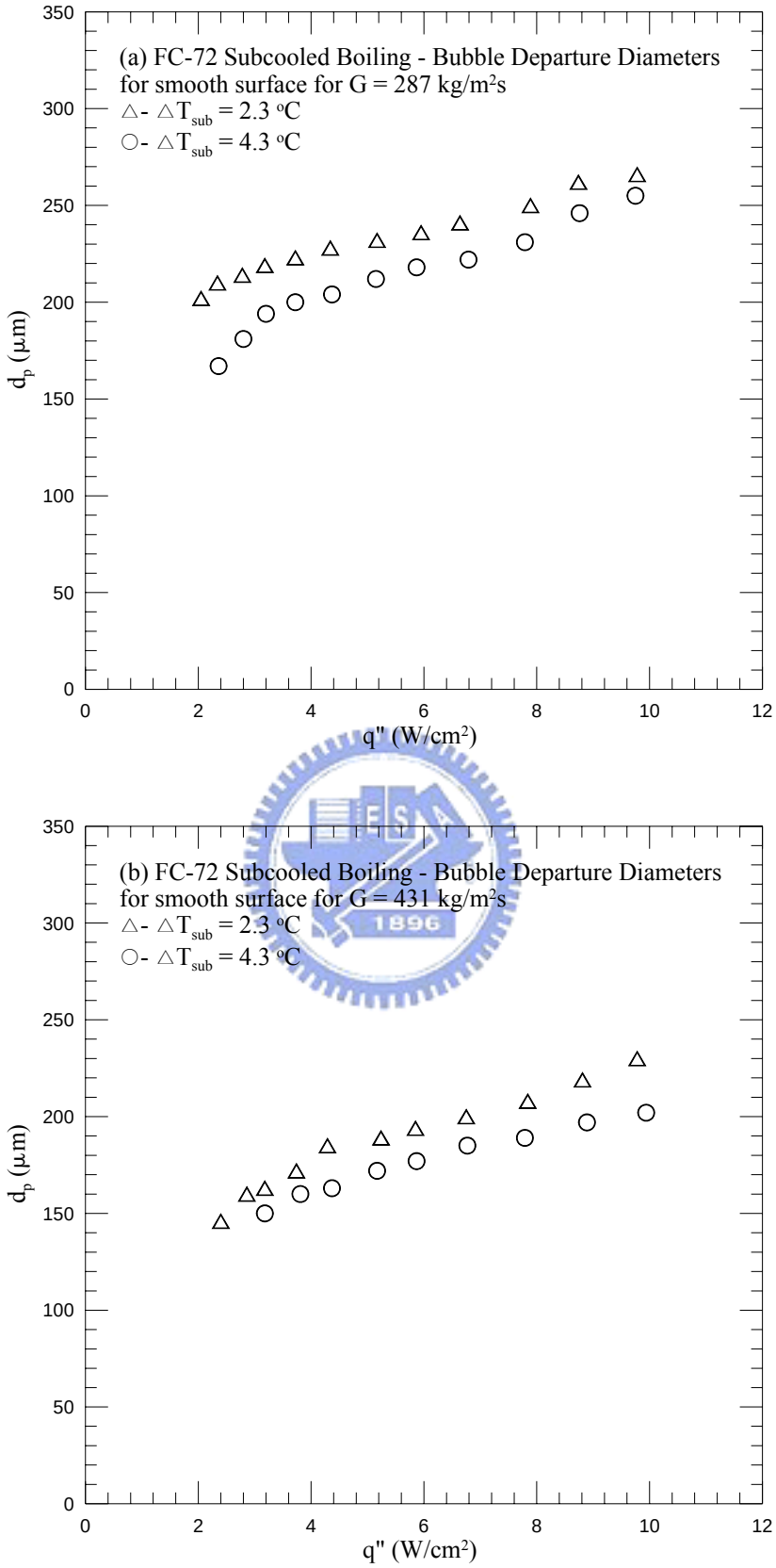

Fig. 5.26 Mean bubble departure diameters for subcooled flow boiling from smooth surface for various inlet liquid subcoolings at (a) G = 287 kg/m^{2}s and (b) G = 431 kg/m^{2}s

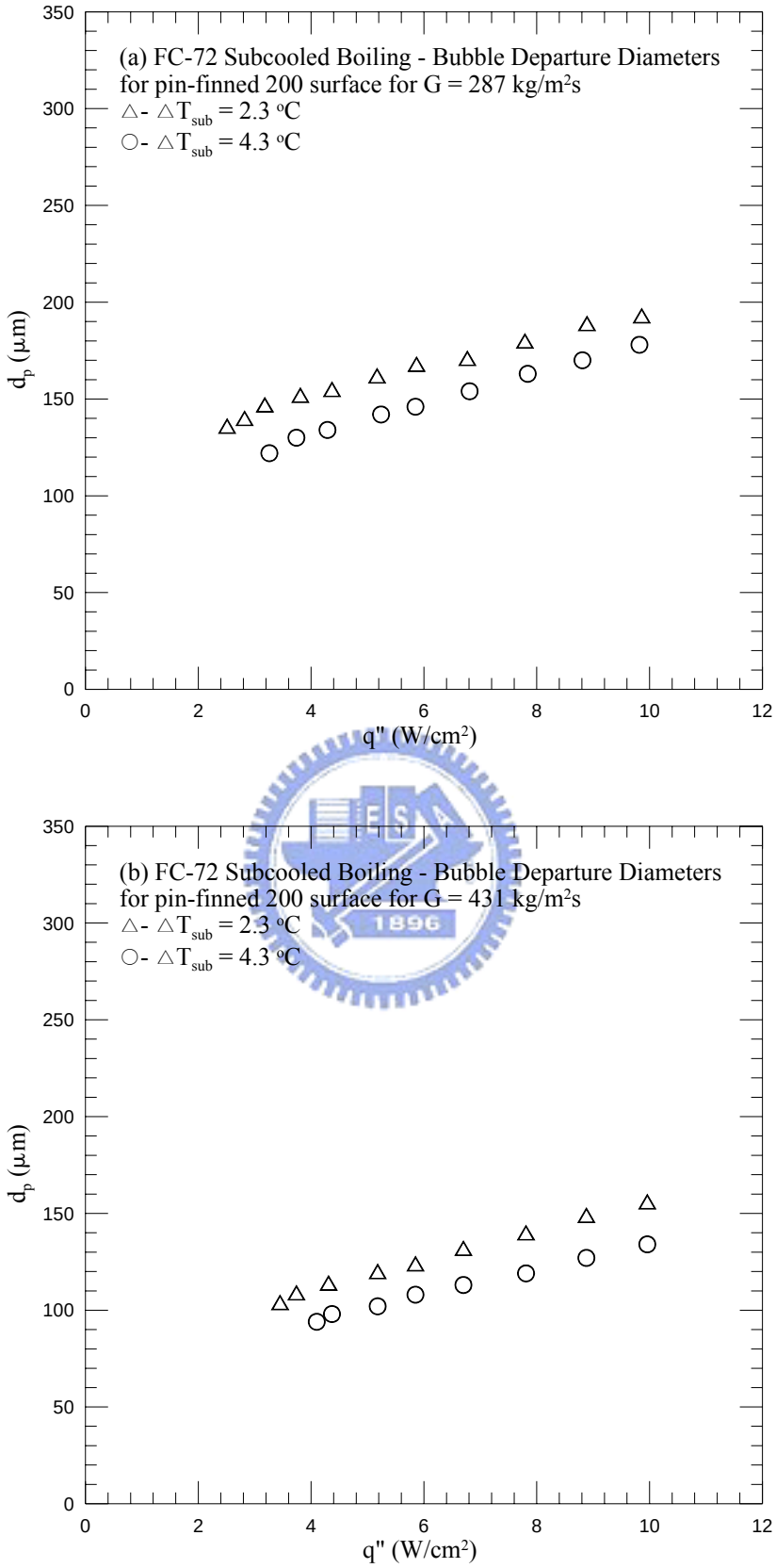

Fig. 5.27 Mean bubble departure diameters for subcooled flow boiling from pin-finned 200 surface for various inlet liquid subcoolings at (a) G = 287 kg/m^{2}s and (b) G = 431 kg/m^{2}s

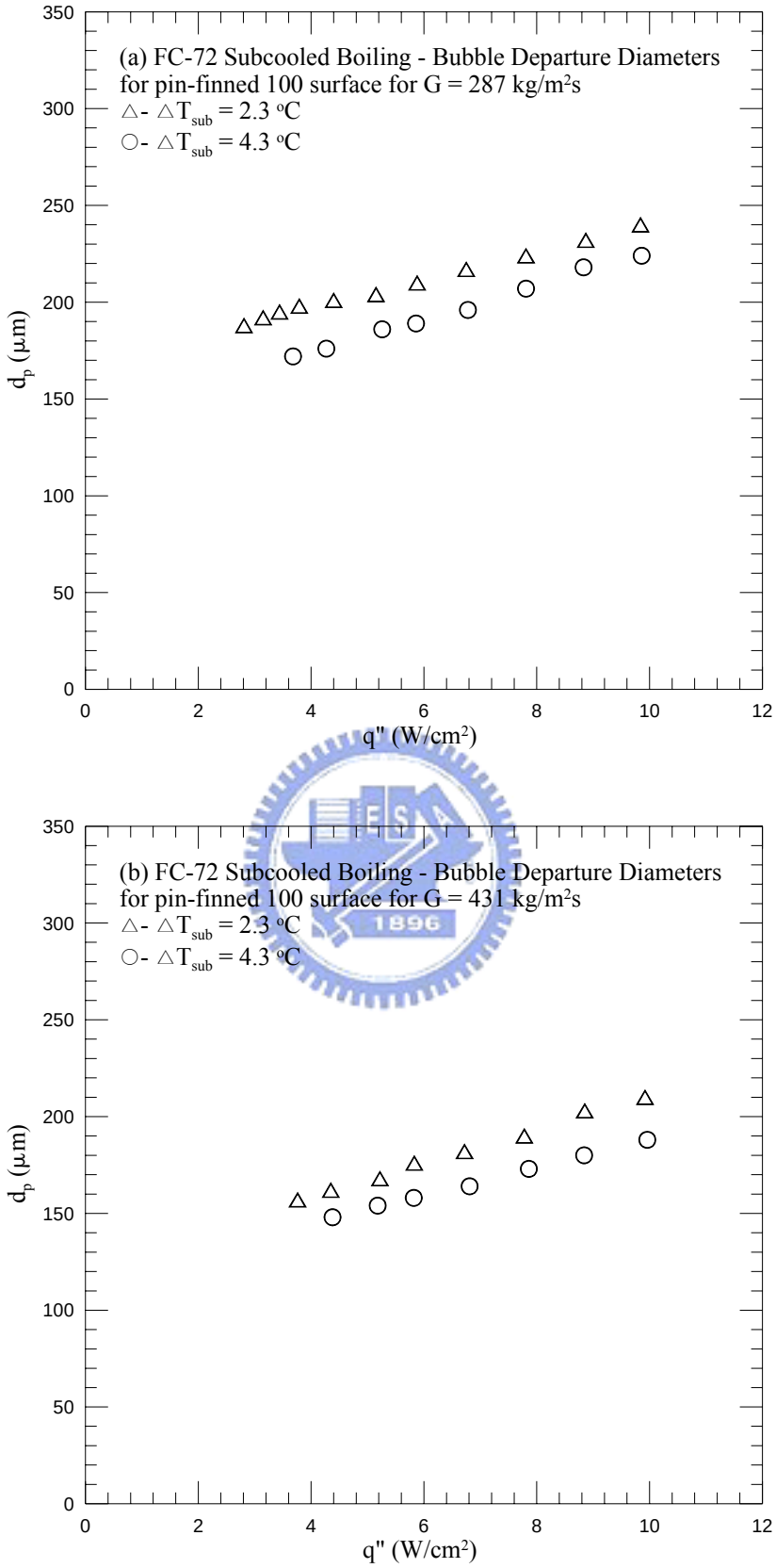

Fig. 5.28 Mean bubble departure diameters for subcooled flow boiling from pin-finned 100 surface for various inlet liquid subcoolings at (a) G = 287 kg/m^{2}s and (b) G = 431 kg/m^{2}s

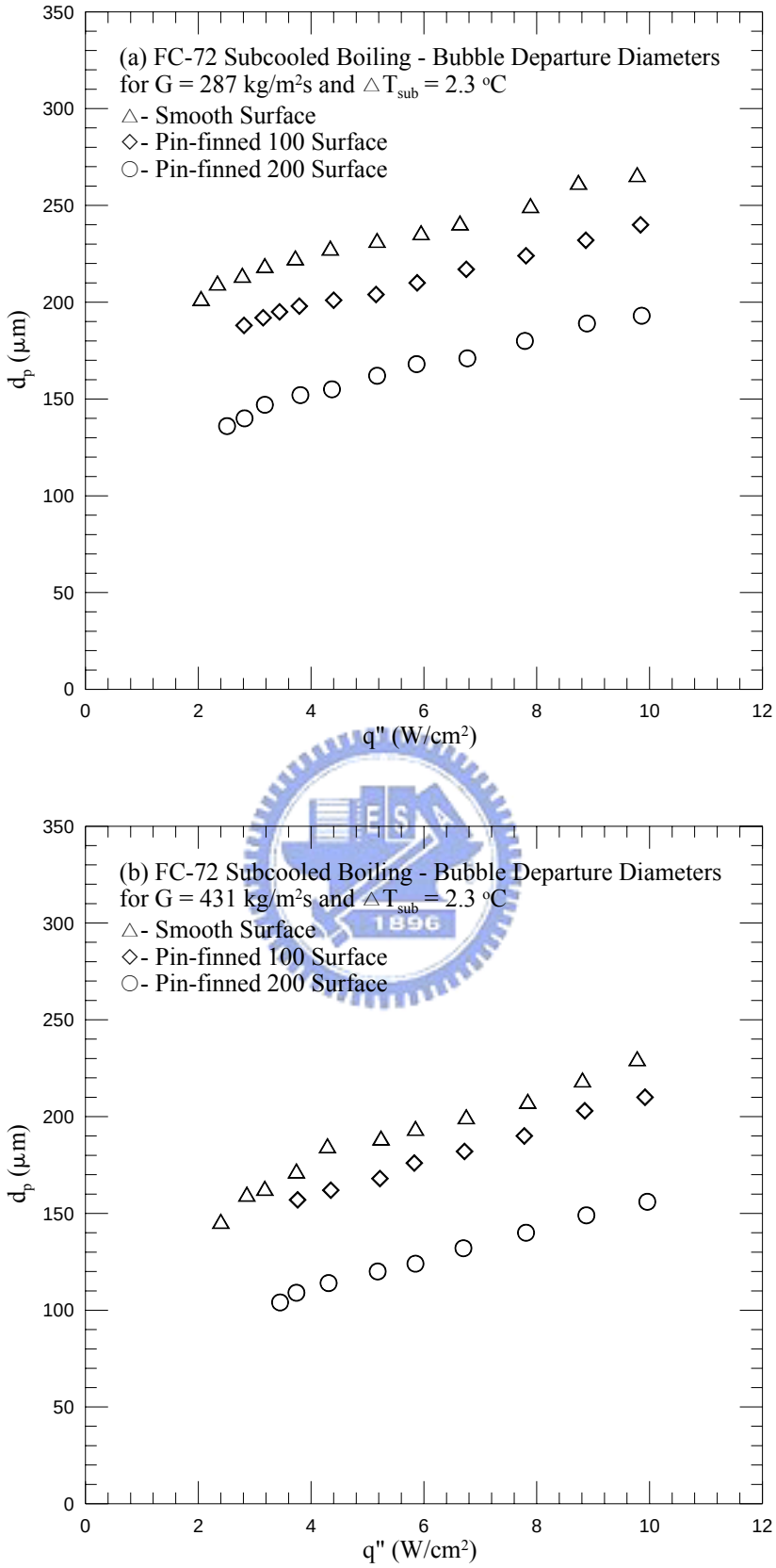

Fig. 5.29 Mean bubble departure diameters for subcooled flow boiling affected by surface micro-structures for ΔT_{sub} = 2.3 °C at (a) G = 287 kg/m^{2}s and (b) G = 431 kg/m^{2}s

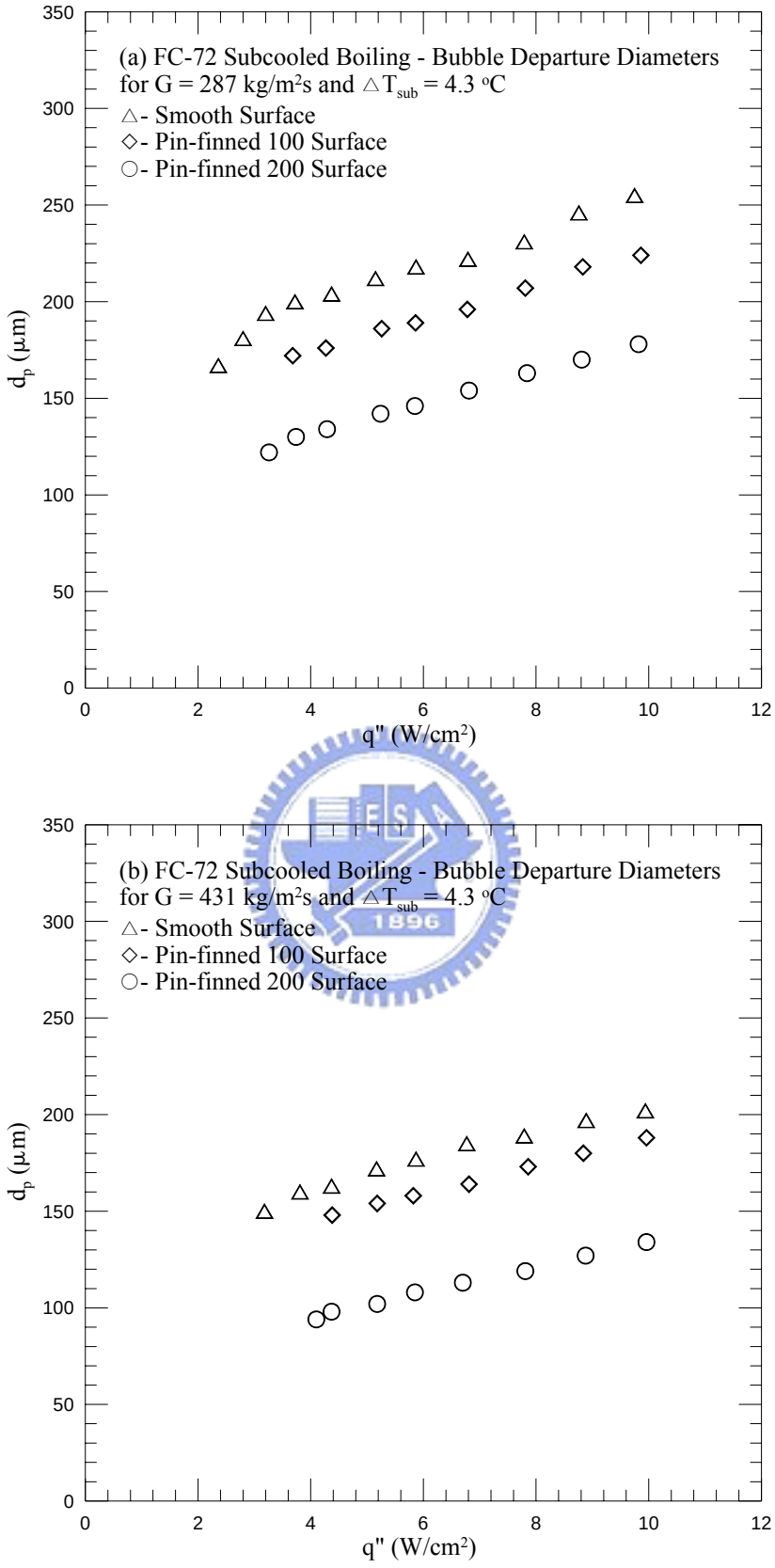

Fig. 5.30 Mean bubble departure diameters for subcooled flow boiling affected by surface micro-structures for ΔT_{sub} = 4.3 °C at (a) G = 287 kg/m^{2}s and (b) G = 431 kg/m^{2}s

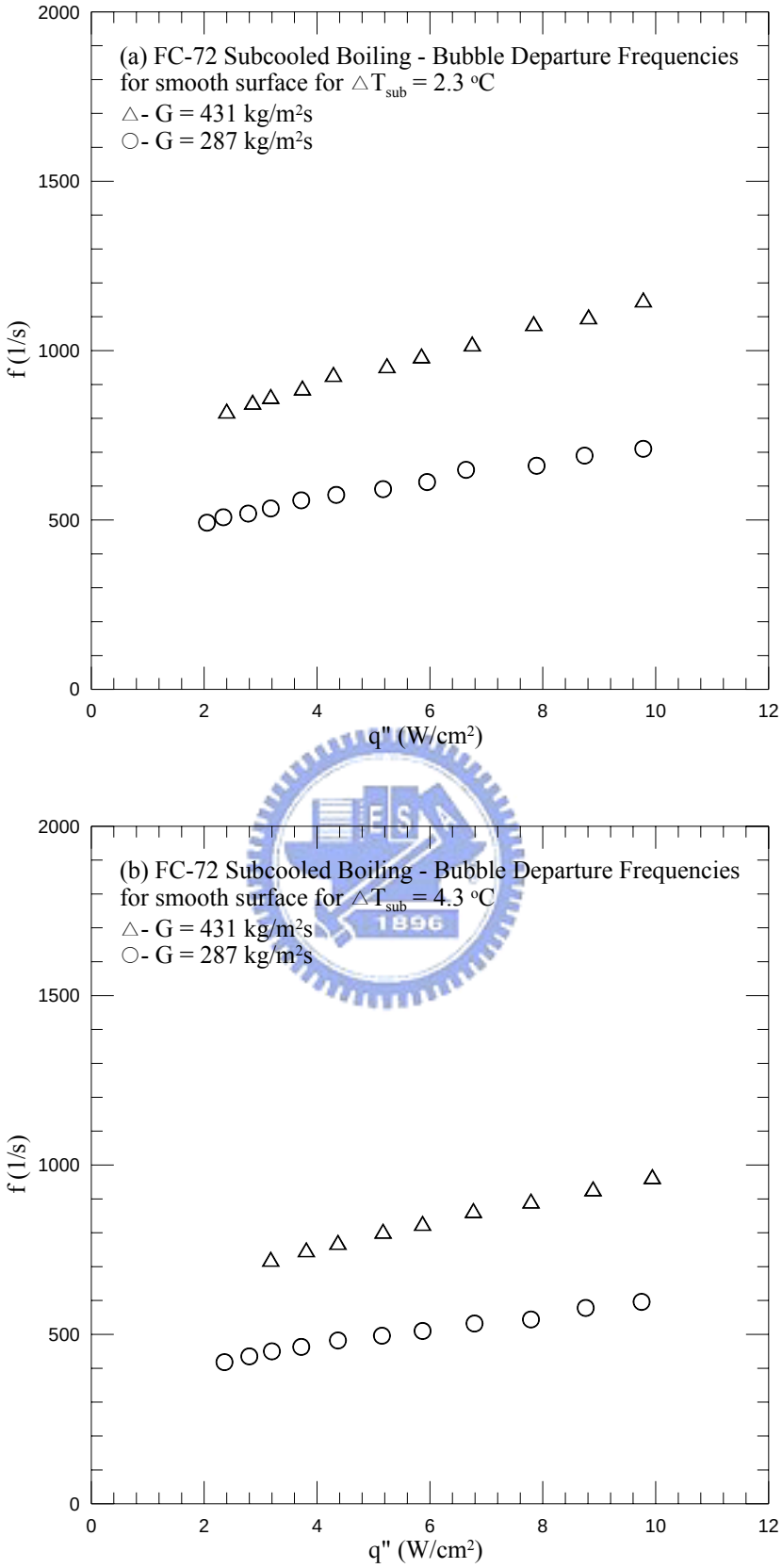

Fig. 5.31 Mean bubble departure frequencies for subcooled flow boiling from smooth surface for various coolant mass fluxes at (a) $\Delta T_{sub} = 2.3\ ^{o}C$ and (b) $\Delta T_{sub} = 4.3\ ^{o}C$

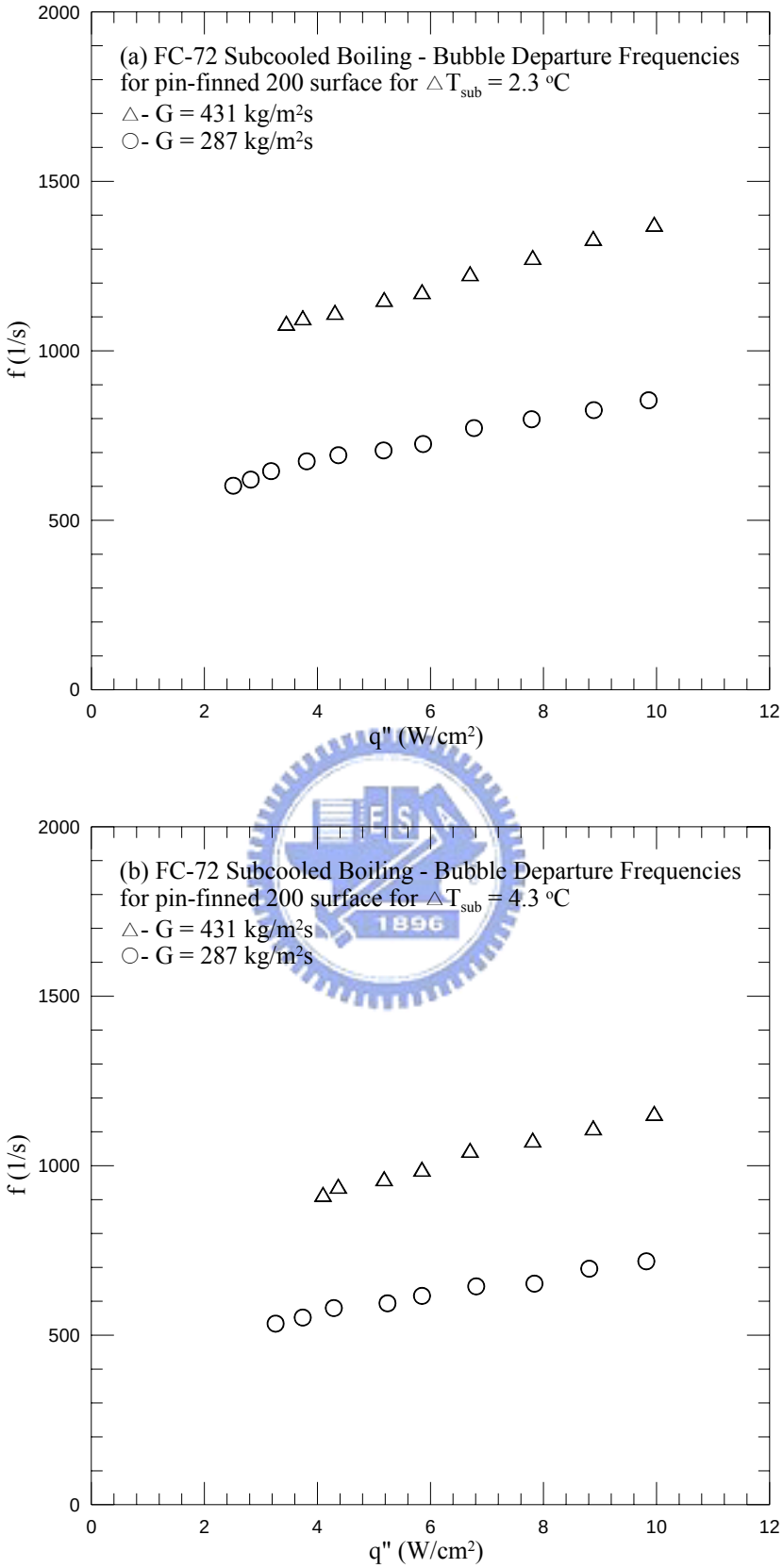

Fig. 5.32 Mean bubble departure frequencies for subcooled flow boiling from pin-finned 200 surface for various coolant mass fluxes at (a) ΔT_{sub} = 2.3 °C and (b) ΔT_{sub} = 4.3 °C

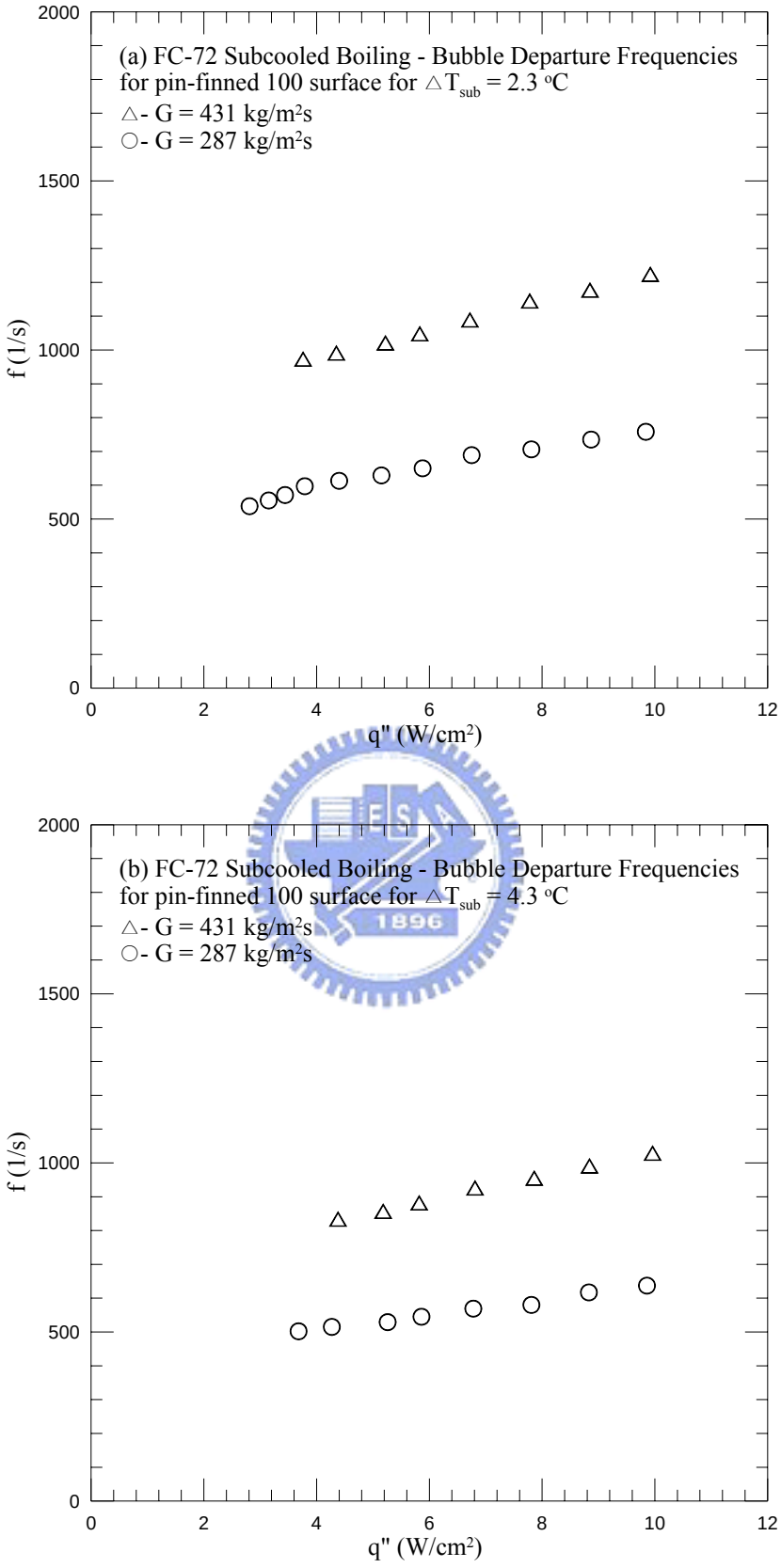

Fig. 5.33 Mean bubble departure frequencies for subcooled flow boiling from pin-finned 100 surface for various coolant mass fluxes at (a) ΔT_{sub} = 2.3 °C and (b) ΔT_{sub} = 4.3 °C

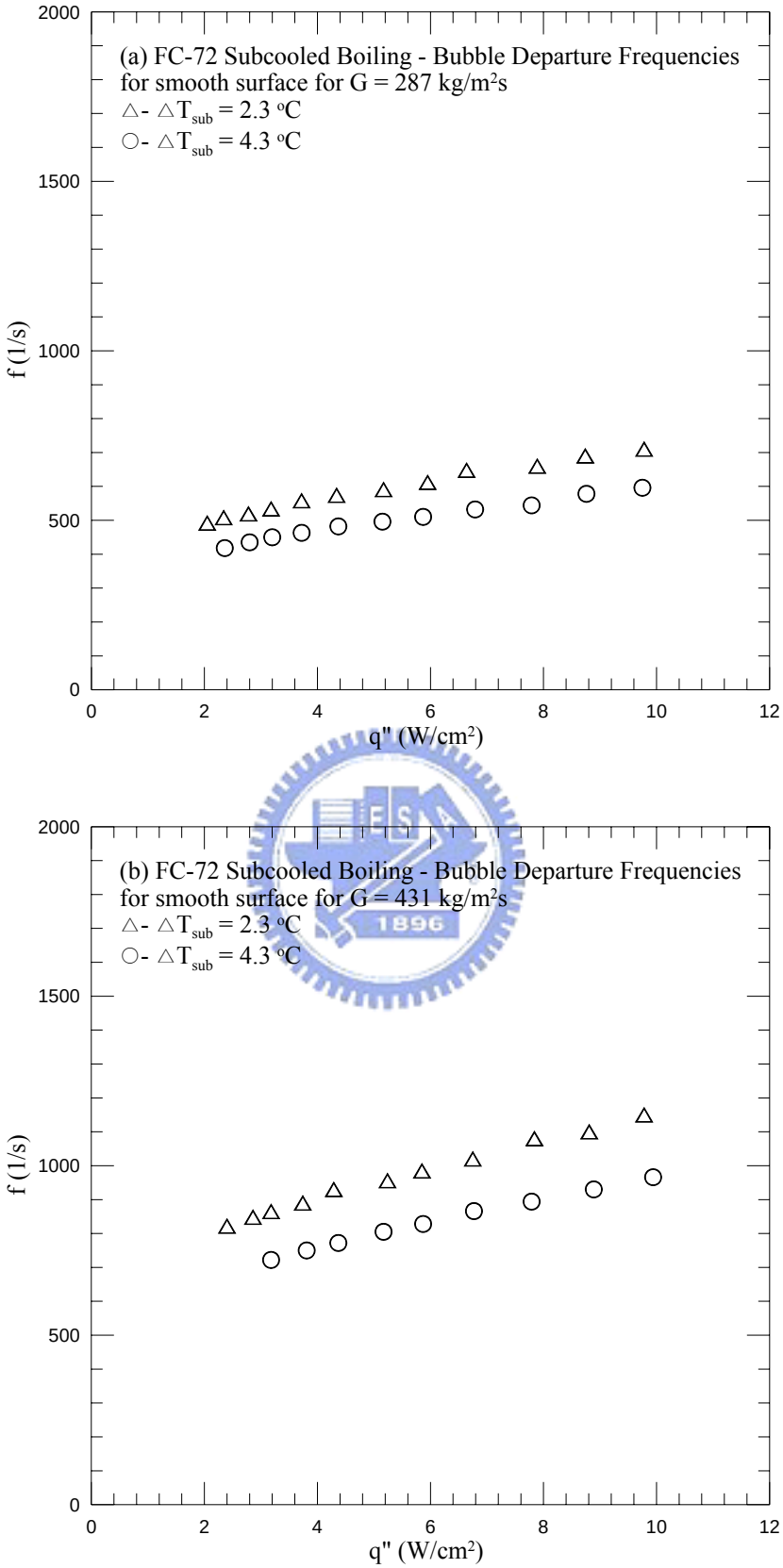

Fig. 5.34 Mean bubble departure frequencies for subcooled flow boiling from smooth surface for various inlet liquid subcoolings at (a) G = 287 kg/m^{2}s and (b) G = 431 kg/m^{2}s

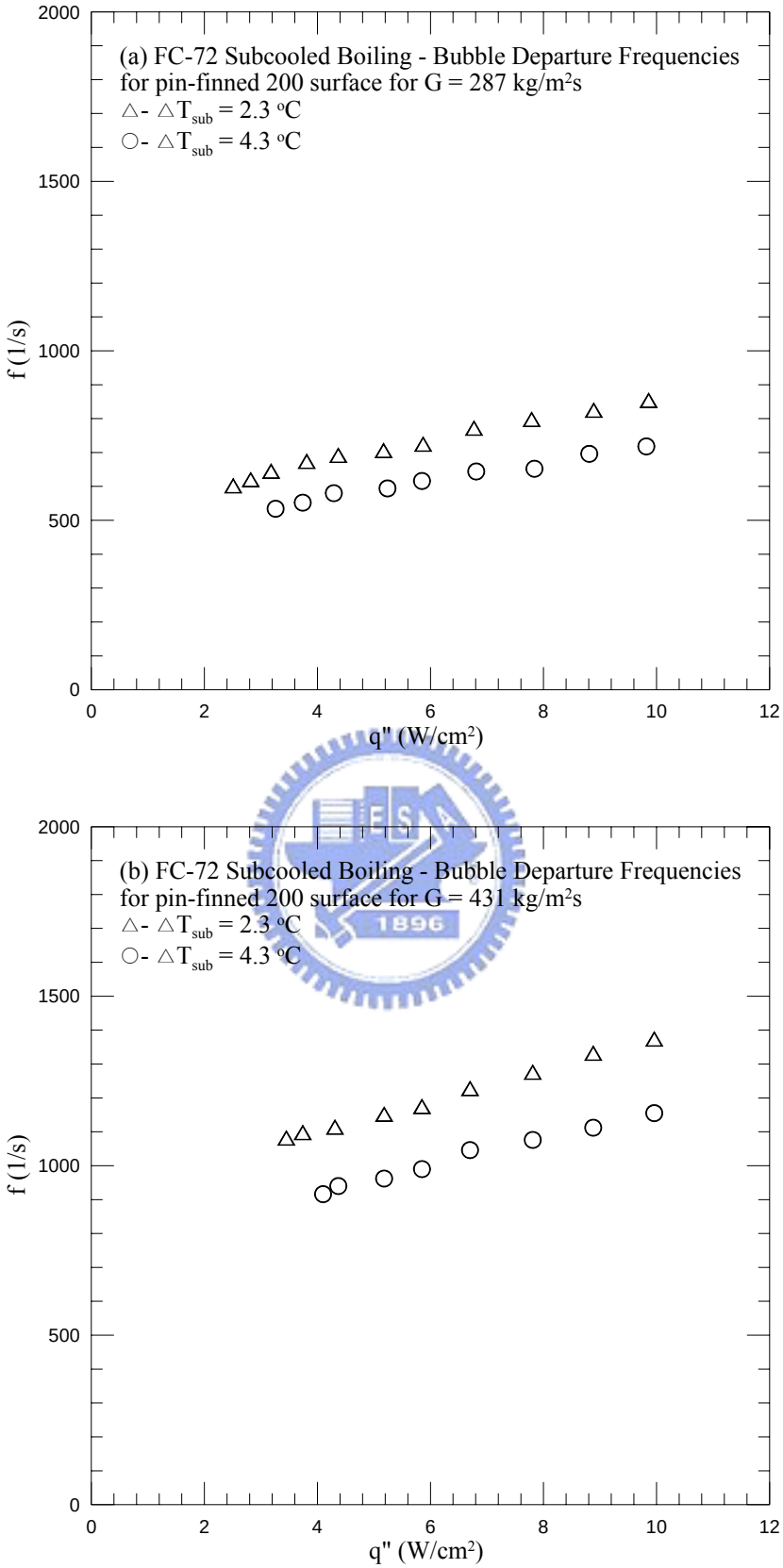

Fig. 5.35 Mean bubble departure frequencies for subcooled flow boiling from pin-finned 200 surface for various inlet liquid subcoolings at (a) G = 287 kg/m^{2}s and (b) G = 431 kg/m^{2}s

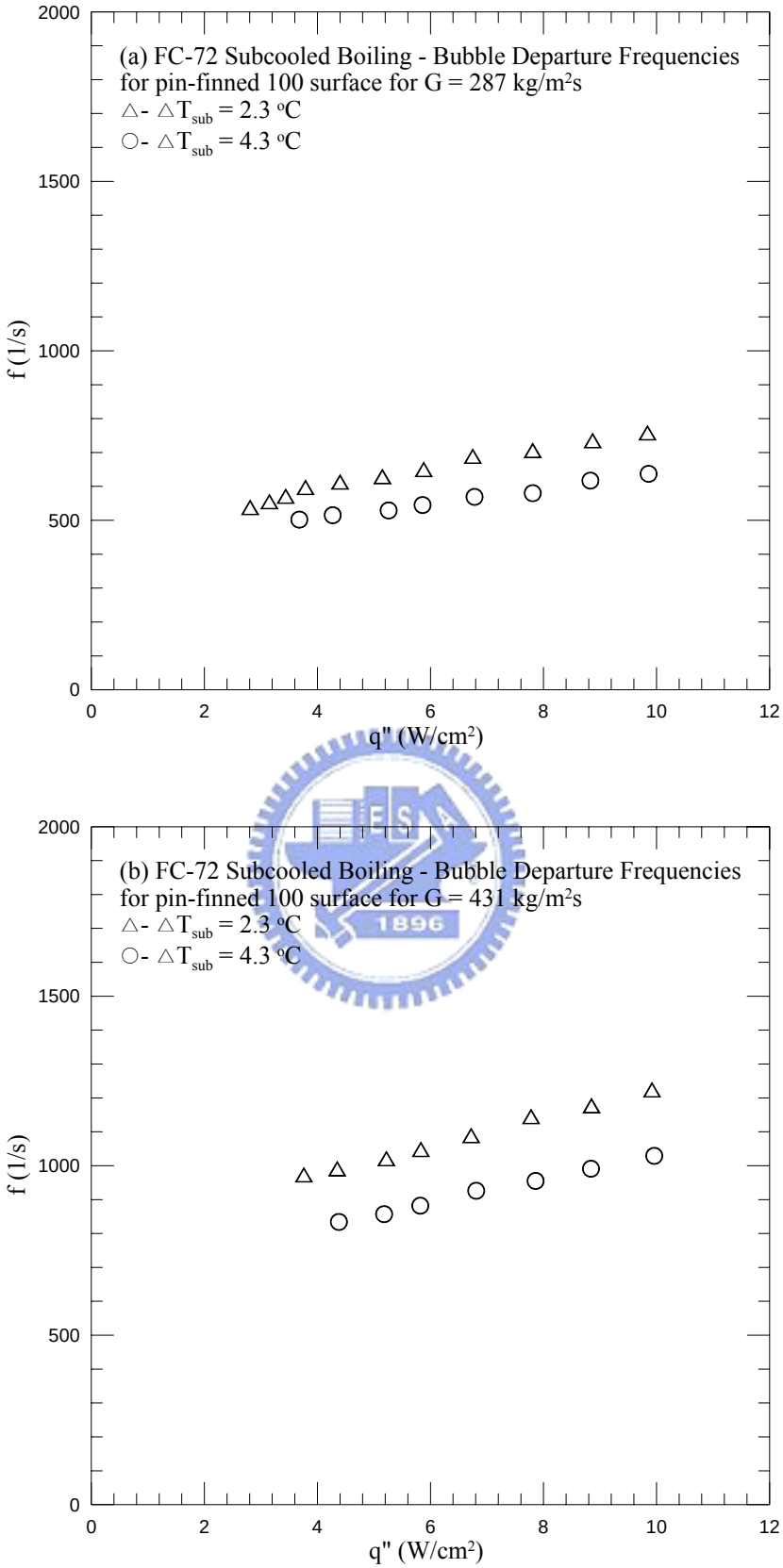

Fig. 5.36 Mean bubble departure frequencies for subcooled flow boiling from pin-finned 100 surface for various inlet liquid subcoolings at (a) G = 287 kg/m^{2}s and (b) G = 431 kg/m^{2}s

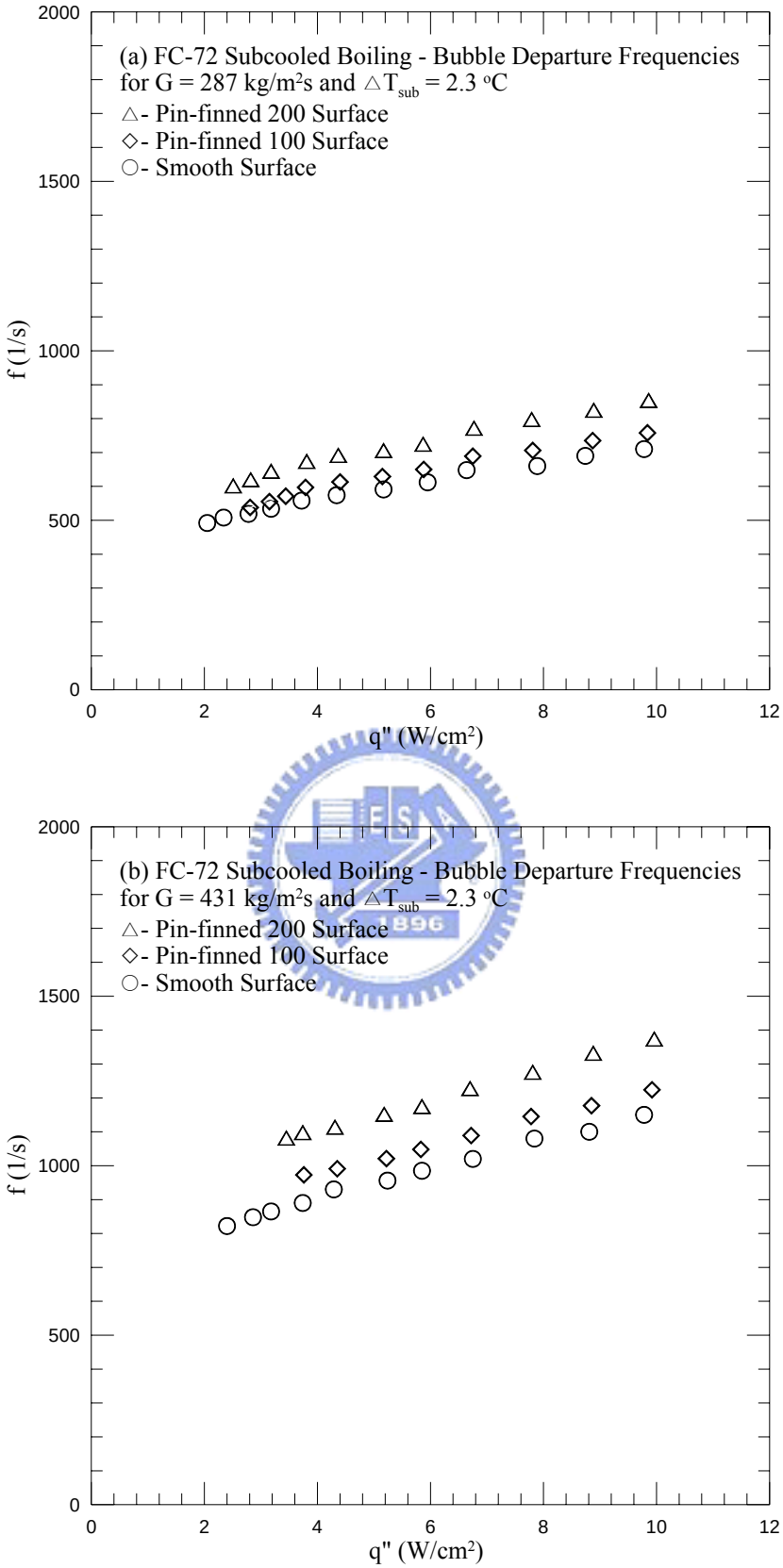

Fig. 5.37 Mean bubble departure frequencies for subcooled flow boiling affected by surface micro-structures for ΔT_{sub} = 2.3 °C at (a) G = 287 kg/m^{2}s and (b) G = 431 kg/m^{2}s

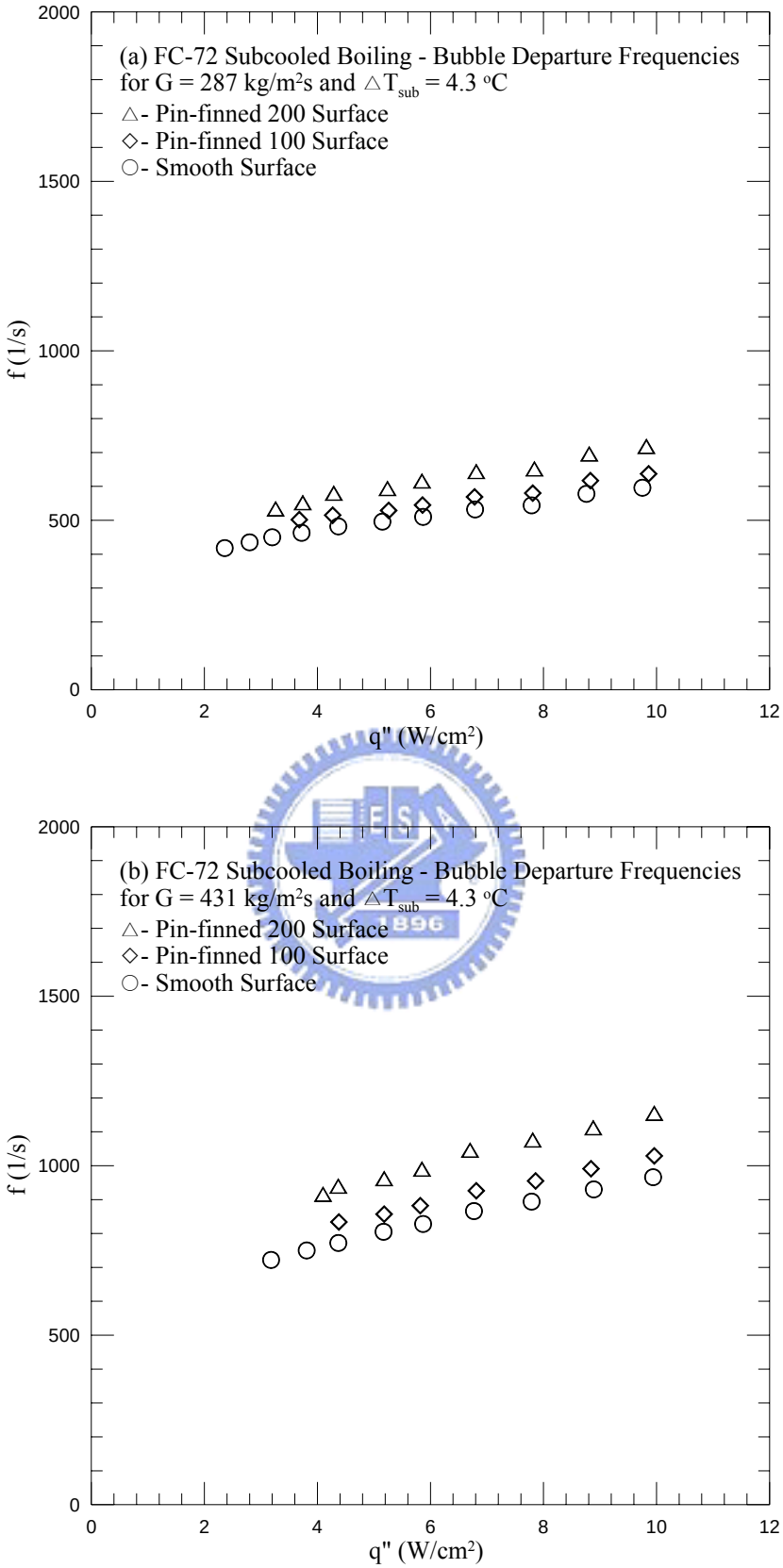

Fig. 5.38 Mean bubble departure frequencies for subcooled flow boiling affected by surface micro-structures for ΔT_{sub} = 4.3 °C at (a) G = 287 kg/m^{2}s and (b) G = 431 kg/m^{2}s

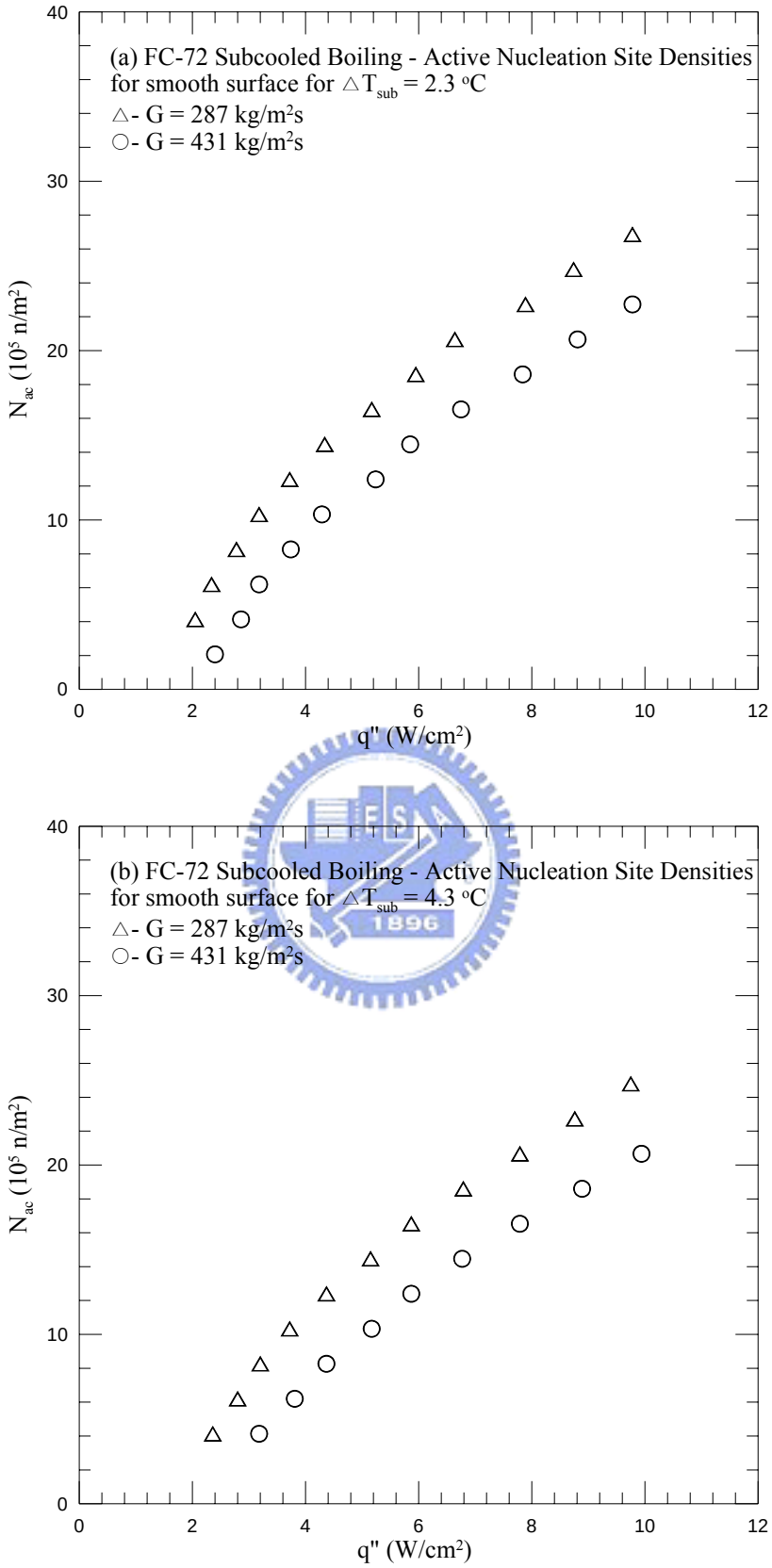

Fig. 5.39 Mean active nucleation site densities for subcooled flow boiling from smooth surface for various coolant mass fluxes at (a) ΔT_{sub} = 2.3 °C and (b) ΔT_{sub} = 4.3 °C

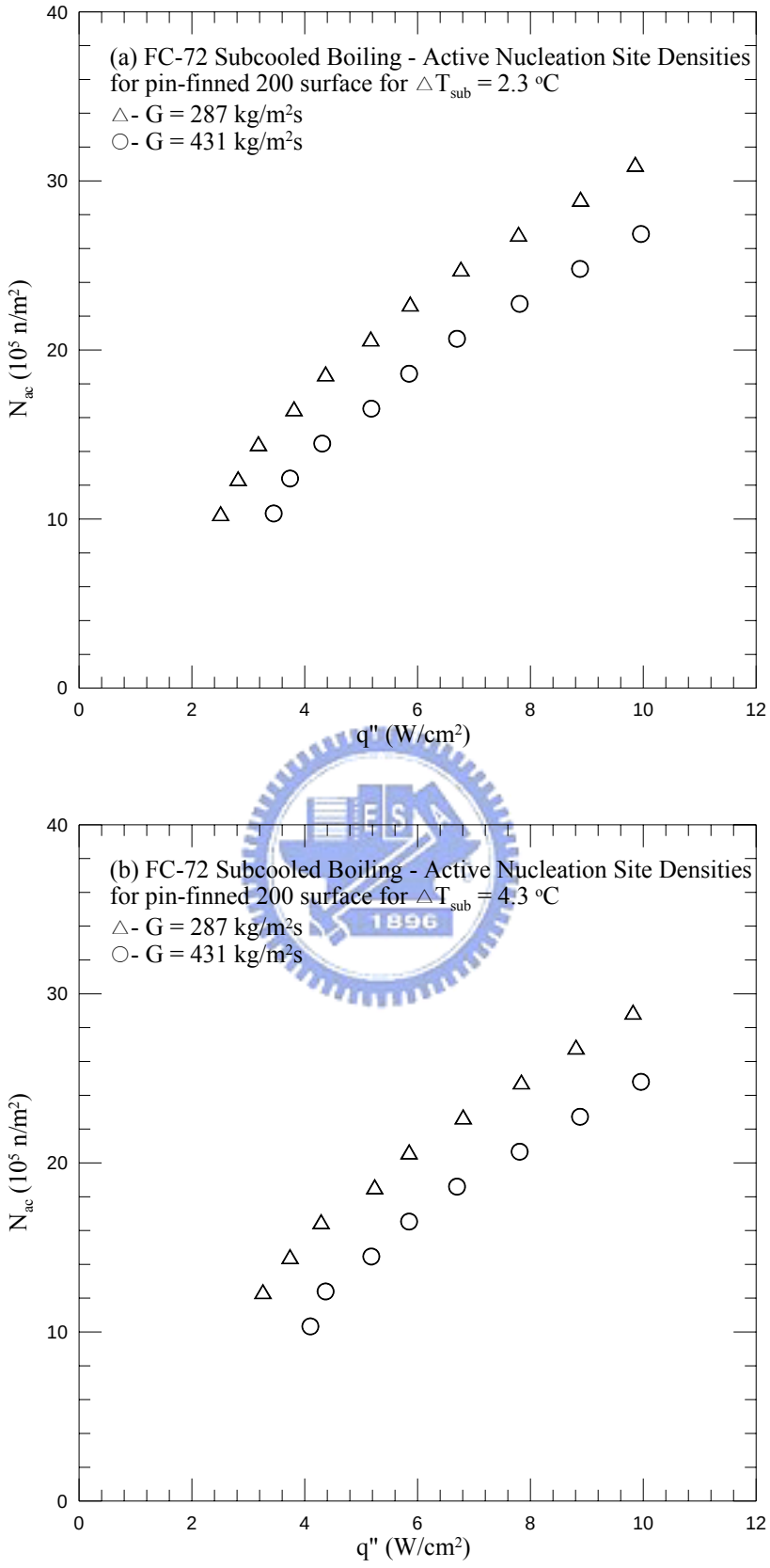

Fig. 5.40 Mean active nucleation site densities for subcooled flow boiling from pin-finned 200 surface for various coolant mass fluxes at (a) ΔT_{sub} = 2.3 °C and (b) ΔT_{sub} = 4.3 °C

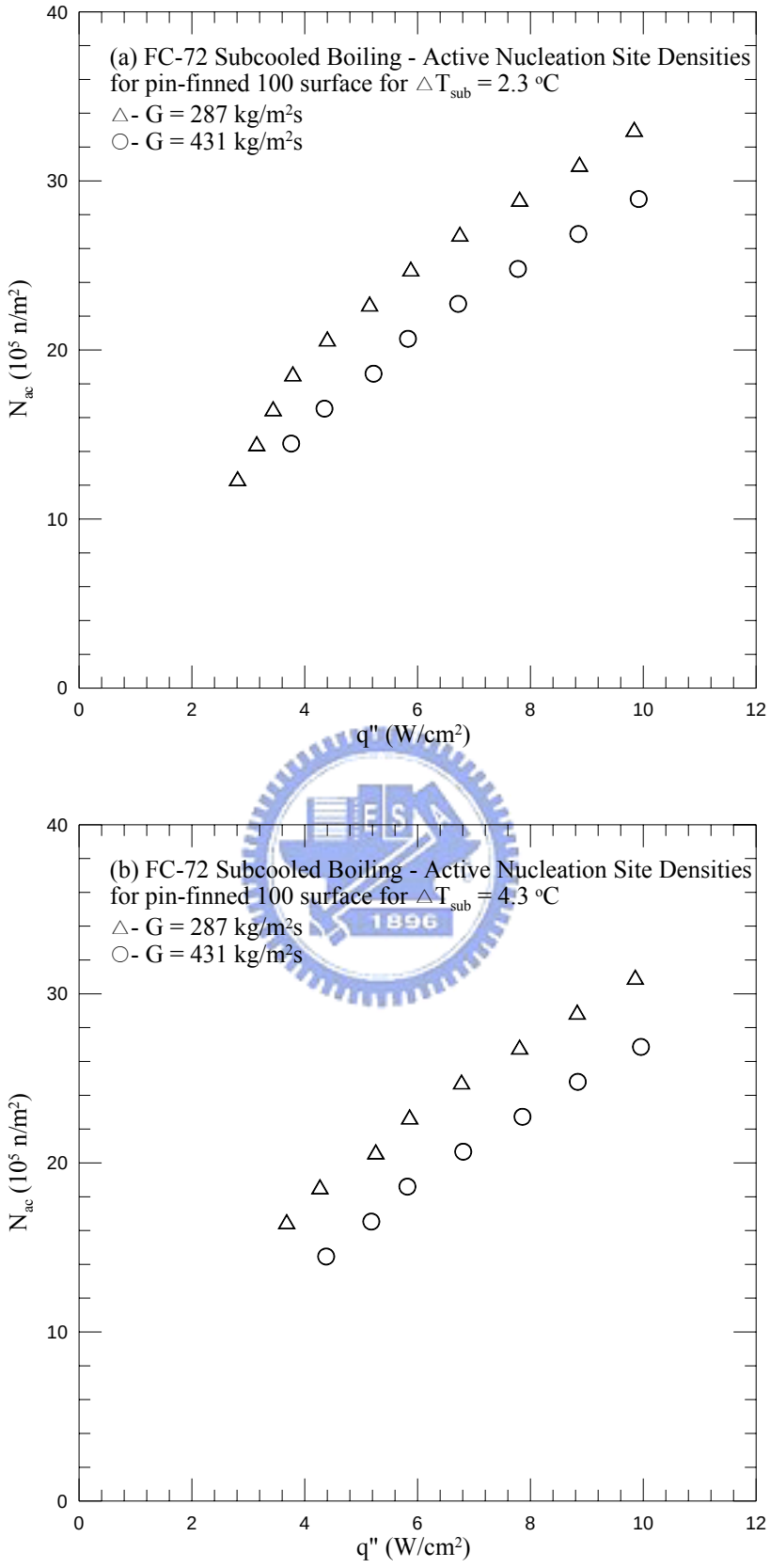

Fig. 5.41 Mean active nucleation site densities for subcooled flow boiling from pin-finned 100 surface for various coolant mass fluxes at (a) ΔT_{sub} = 2.3 °C and (b) ΔT_{sub} = 4.3 °C

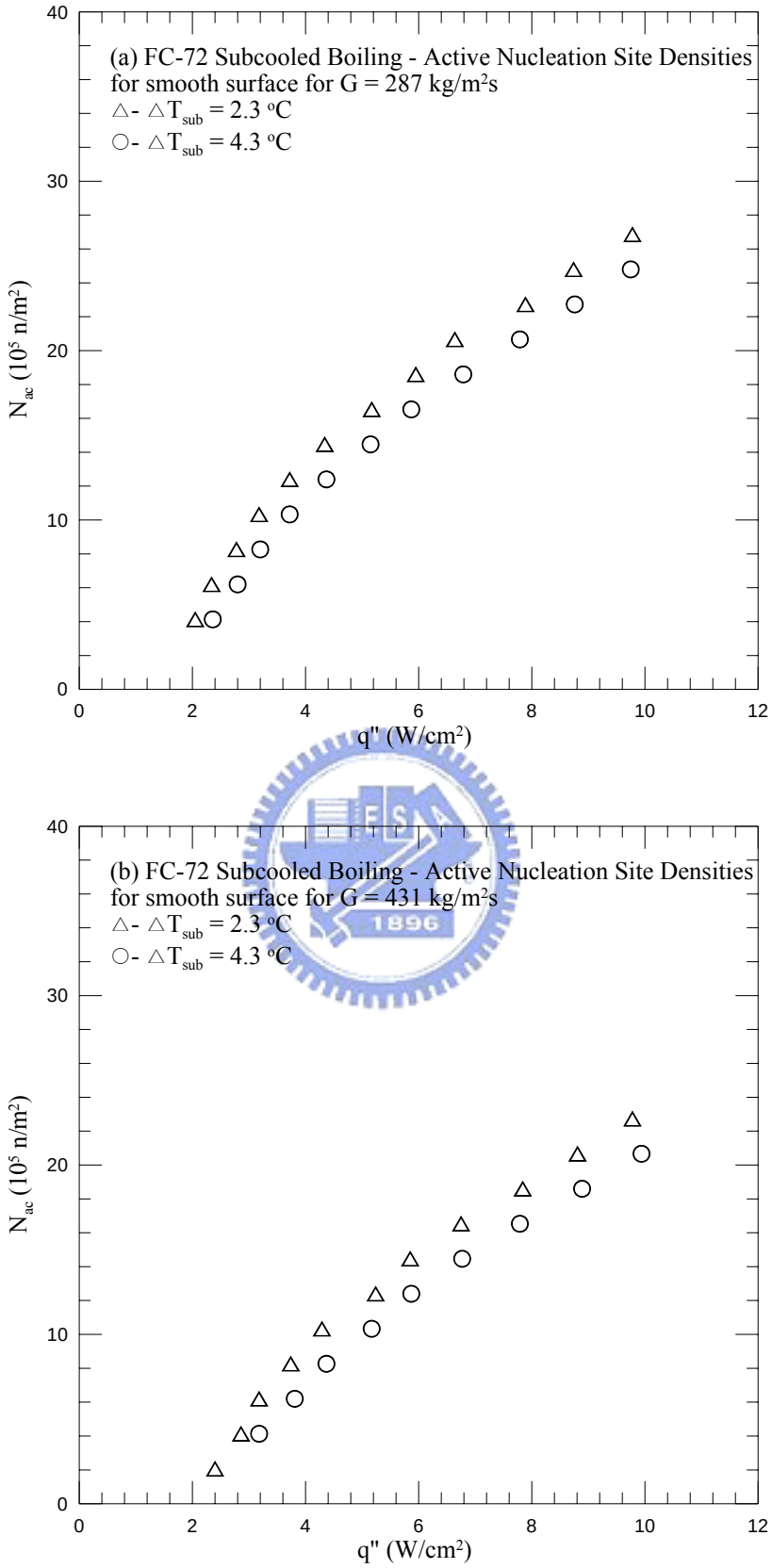

Fig. 5.42 Mean active nucleation site densities for subcooled flow boiling from smooth surface for various inlet liquid subcoolings at (a) G = 287 kg/m^{2}s and (b) G = 431 kg/m^{2}s

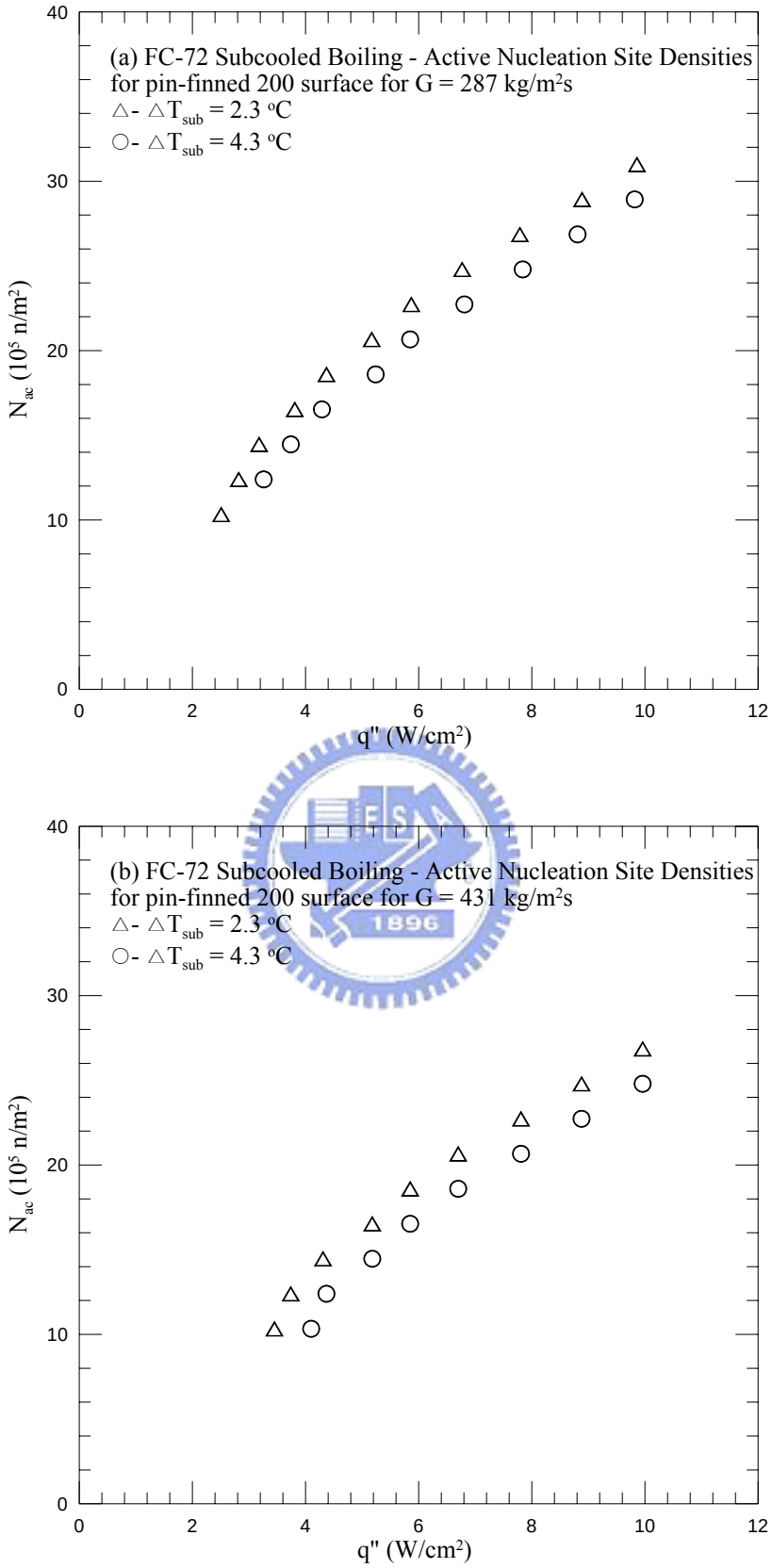

Fig. 5.43 Mean active nucleation site densities for subcooled flow boiling from pin-finned 200 surface for various inlet liquid subcoolings at (a) G = 287 kg/m^{2}s and (b) G = 431 kg/m^{2}s

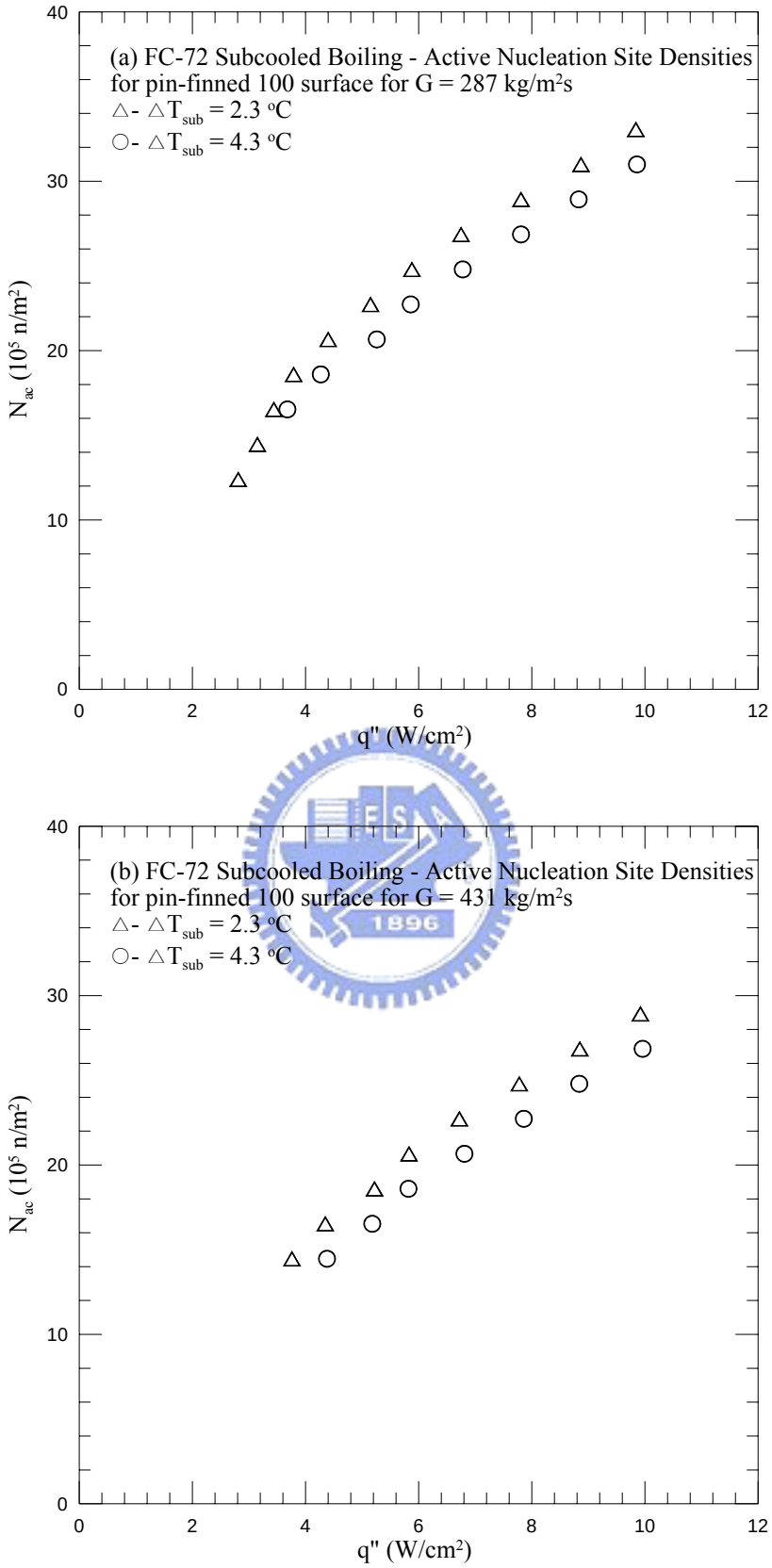

Fig. 5.44 Mean active nucleation site densities for subcooled flow boiling from pin-finned 100 surface for various inlet liquid subcoolings at (a) G = 287 kg/m^{2}s and (b) G = 431 kg/m^{2}s

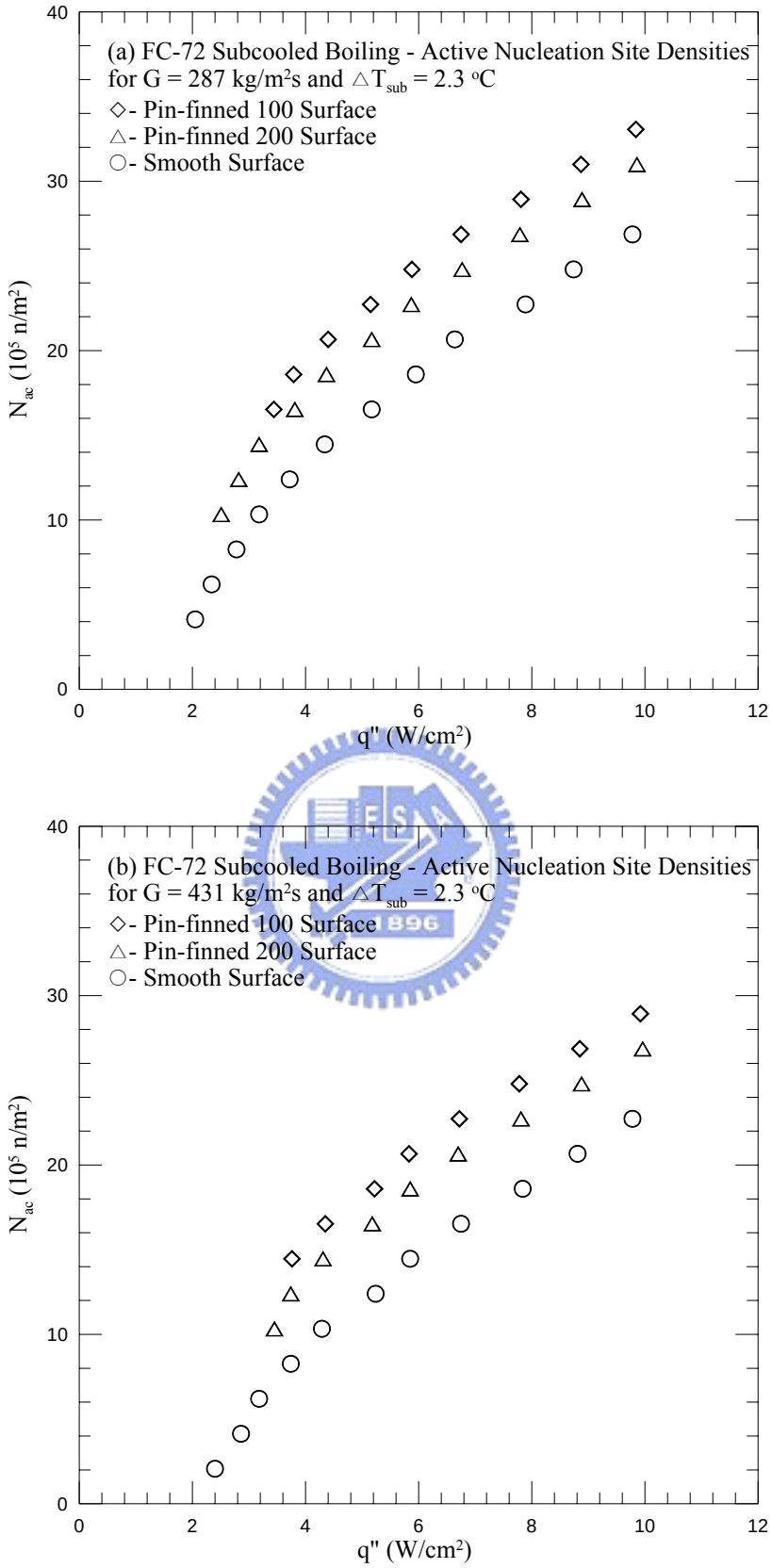

Fig. 5.45 Mean active nucleation site densities for subcooled flow boiling affected by surface micro-structures for ΔT_{sub} = 2.3 °C at (a) G = 287 kg/m^{2}s and (b) G = 431 kg/m^{2}s

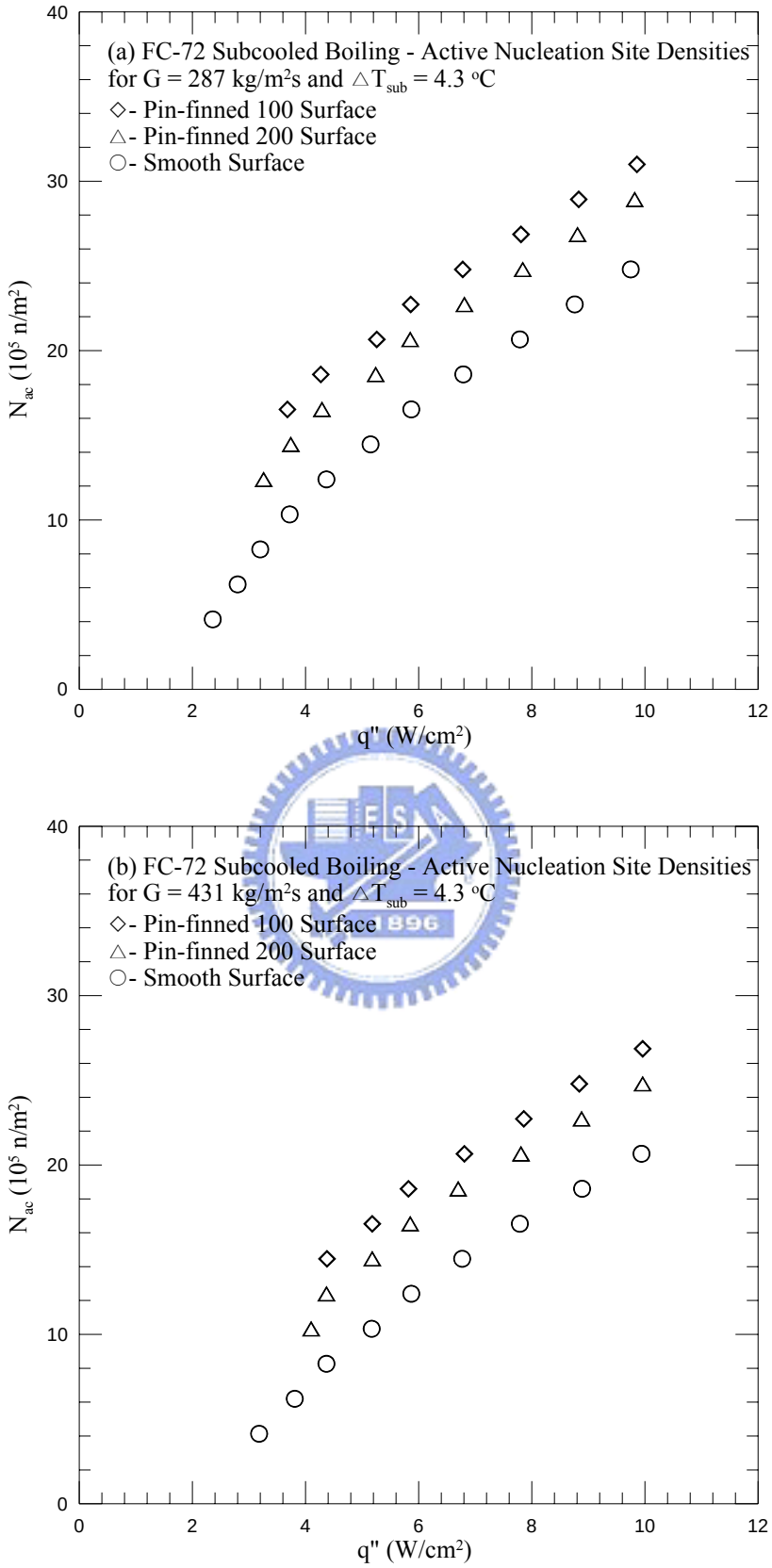

Fig. 5.46 Mean active nucleation site densities for subcooled flow boiling affected by surface micro-structures for ΔT_{sub} = 4.3 °C at (a) G = 287 kg/m^{2}s and (b) G = 431 kg/m^{2}s

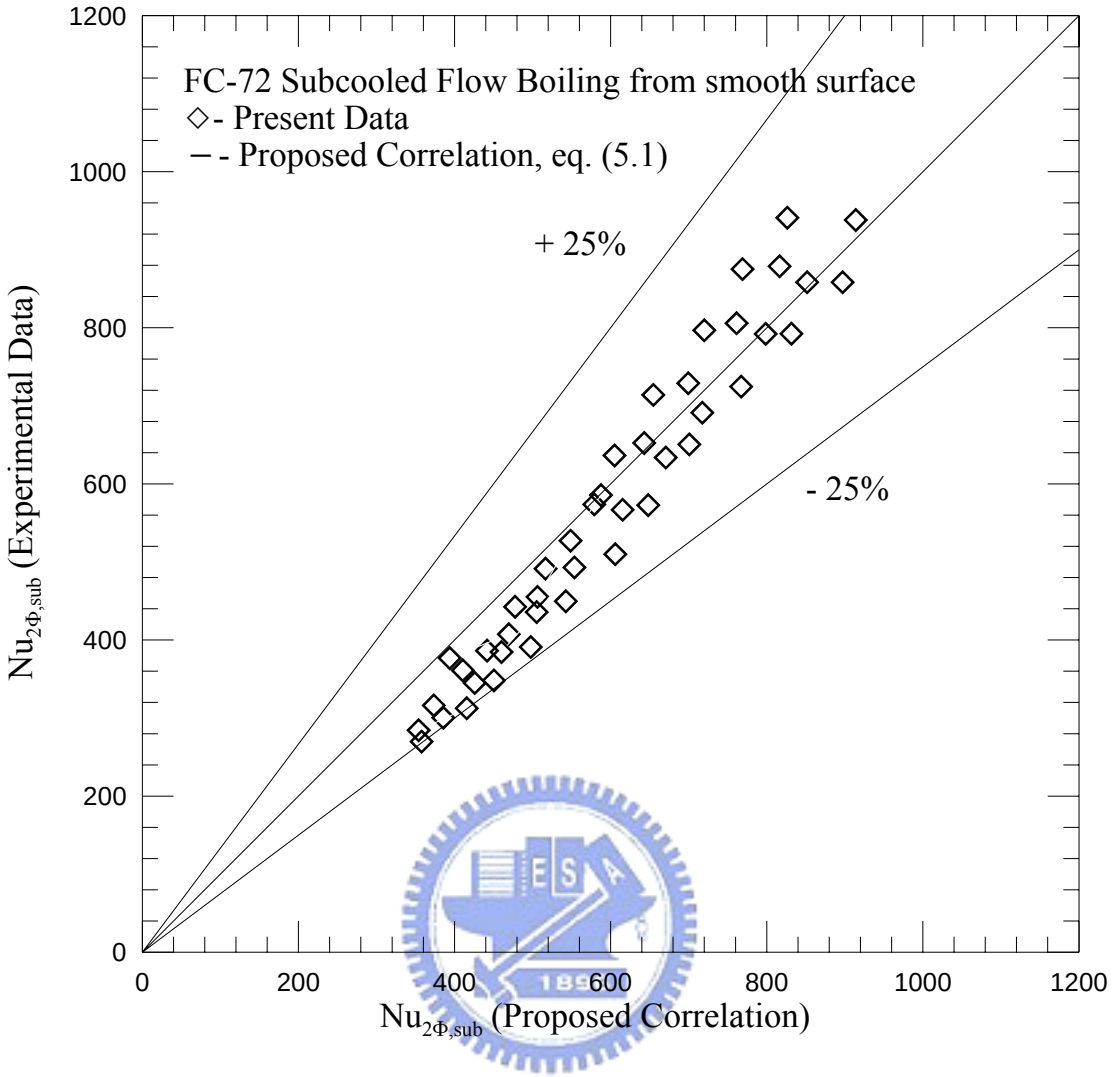

Fig. 5.47 Comparison of the measured data for Nusselt number for subcooled flow boiling of FC-72 on smooth surface with the proposed correlation

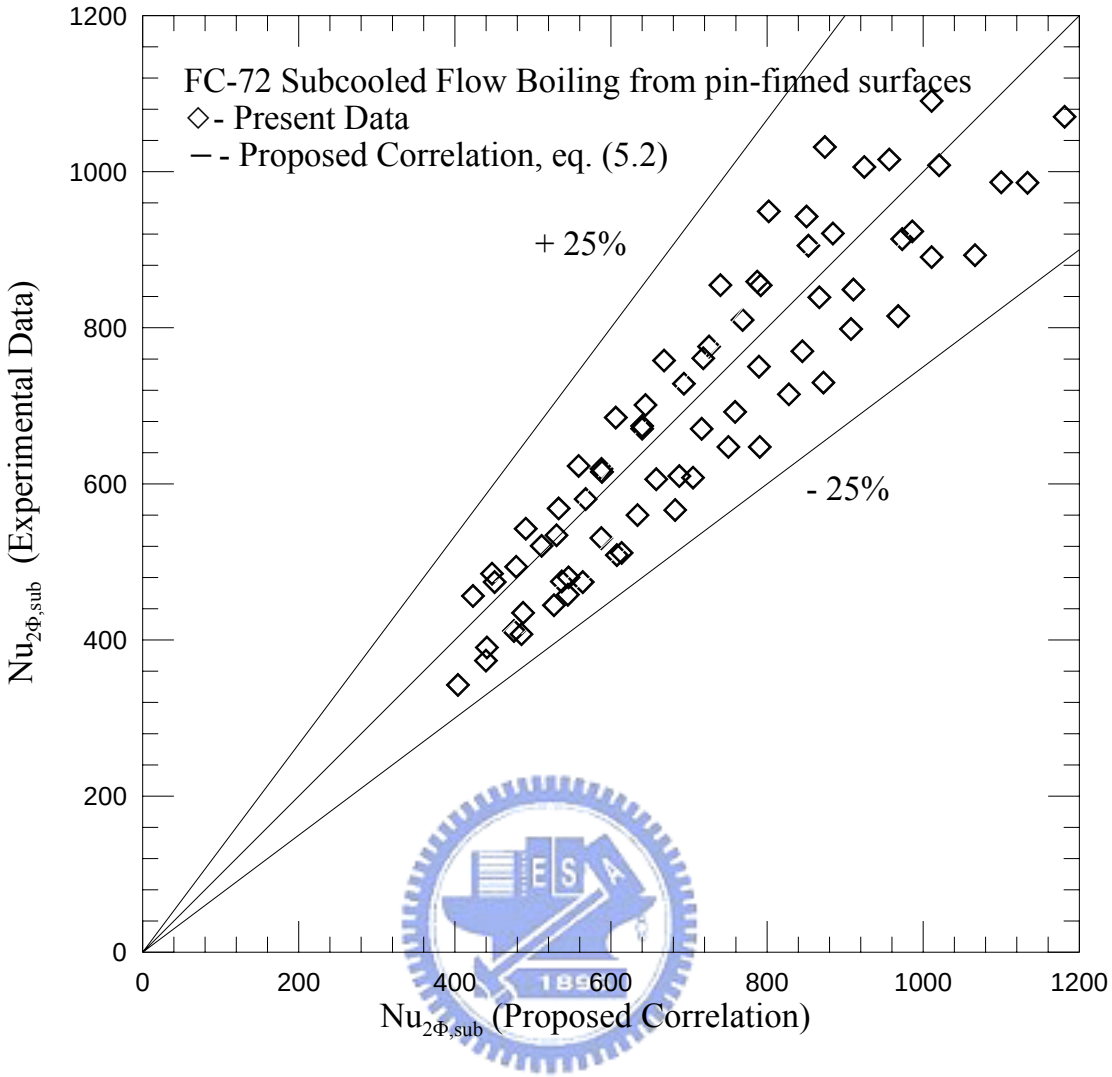

Fig. 5.48 Comparison of the measured data for Nusselt number for subcooled flow boiling of FC-72 on pin-finned surfaces with the proposed correlation

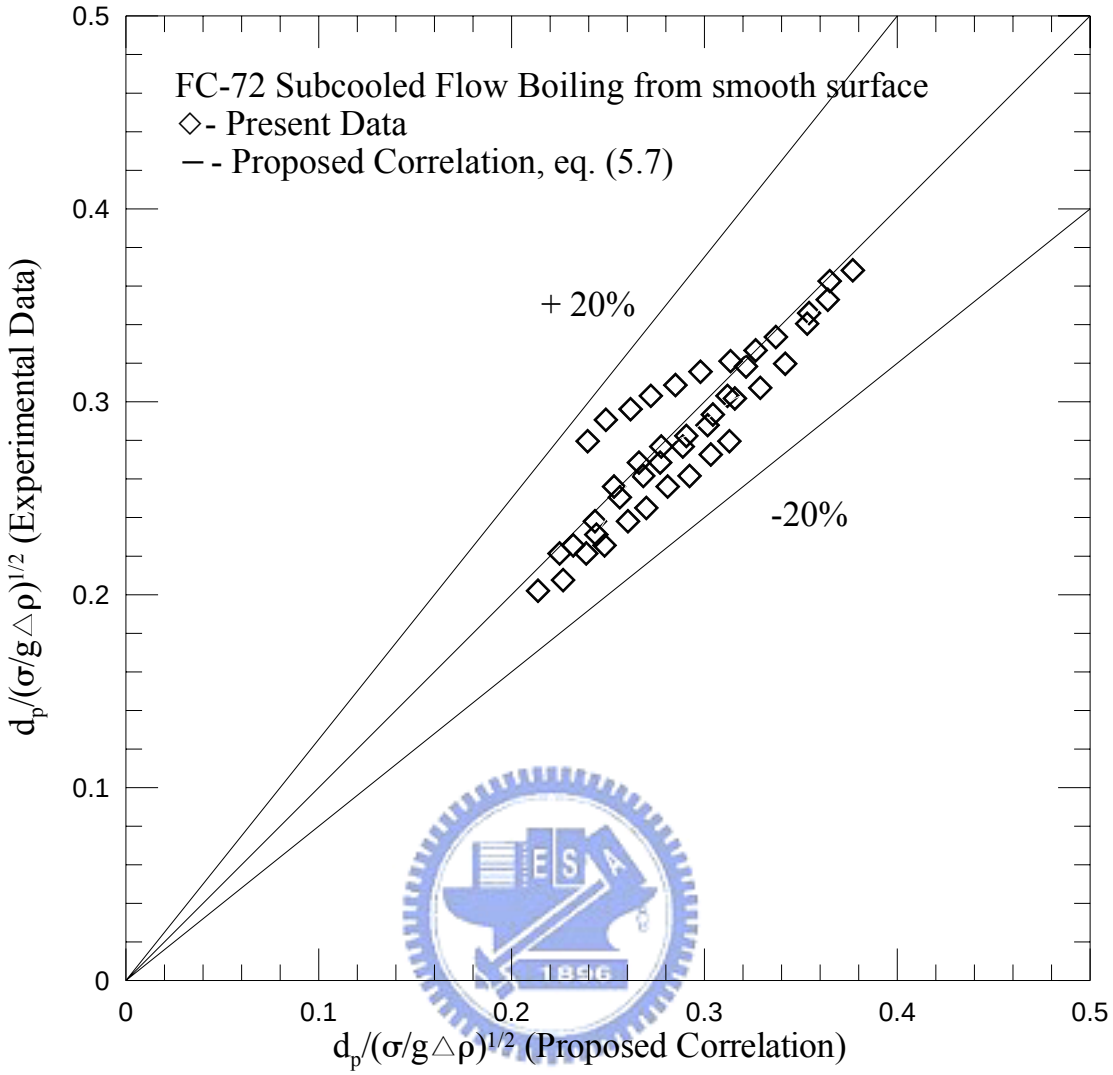

Fig. 5.49 Comparison of the measured data for mean bubble departure diameter for subcooled flow boiling of FC-72 on smooth surface with the proposed correlation

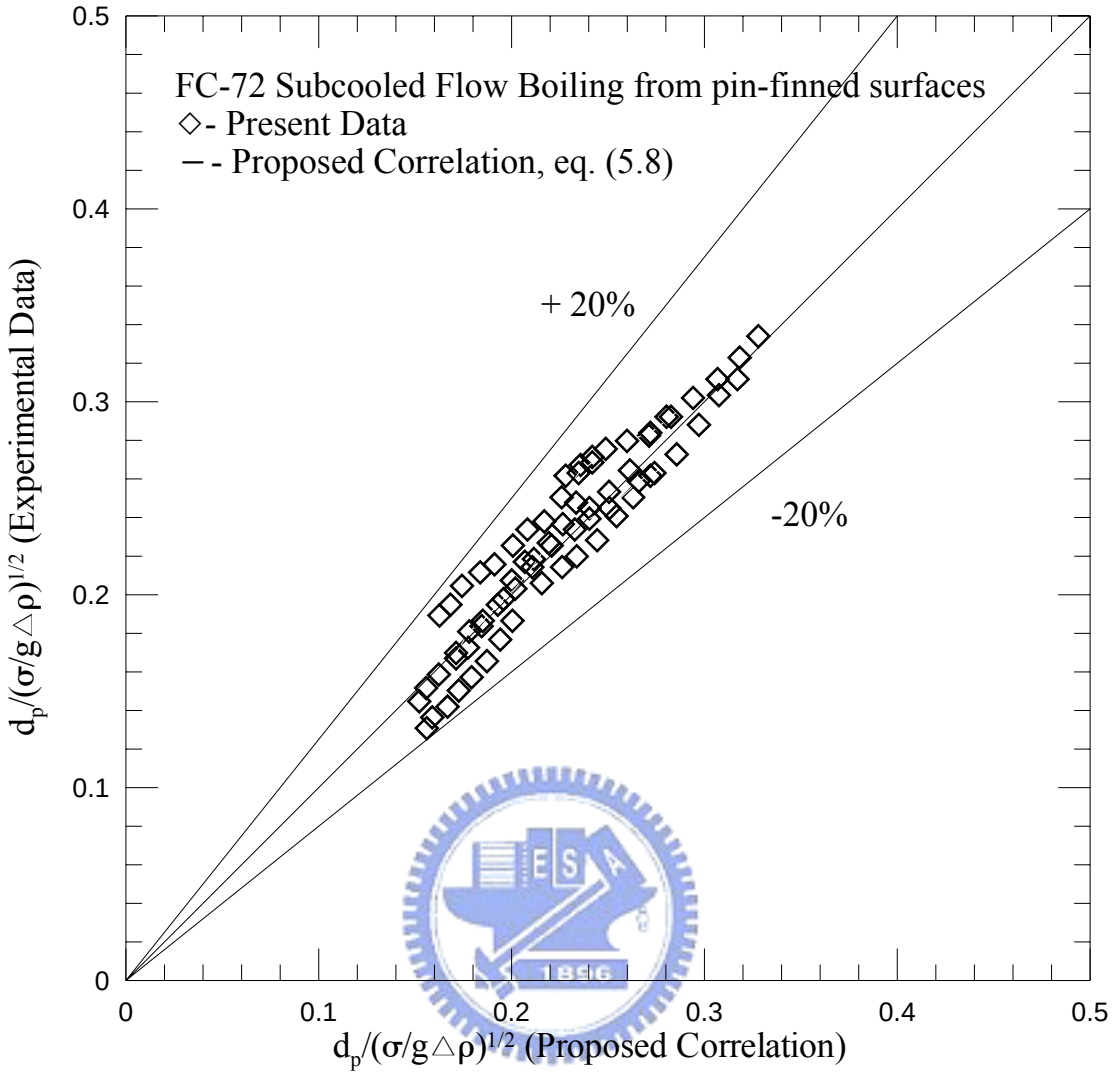

Fig. 5.50 Comparison of the measured data for mean bubble departure diameter for subcooled flow boiling of FC-72 on pin-finned surfaces with the proposed correlation

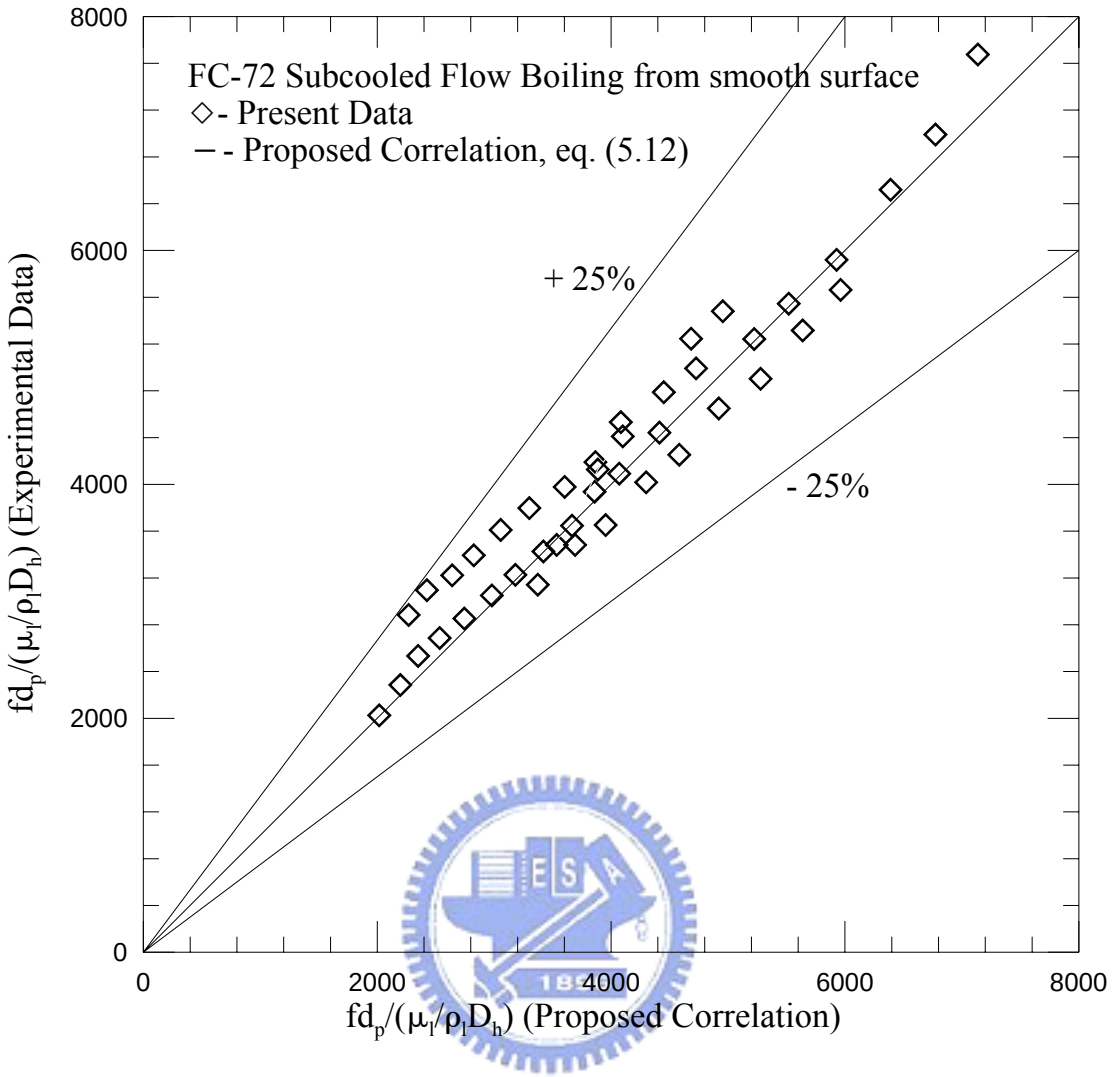

Fig. 5.51 Comparison of the measured data for mean bubble departure frequency for subcooled flow boiling of FC-72 on smooth surface with the proposed correlation

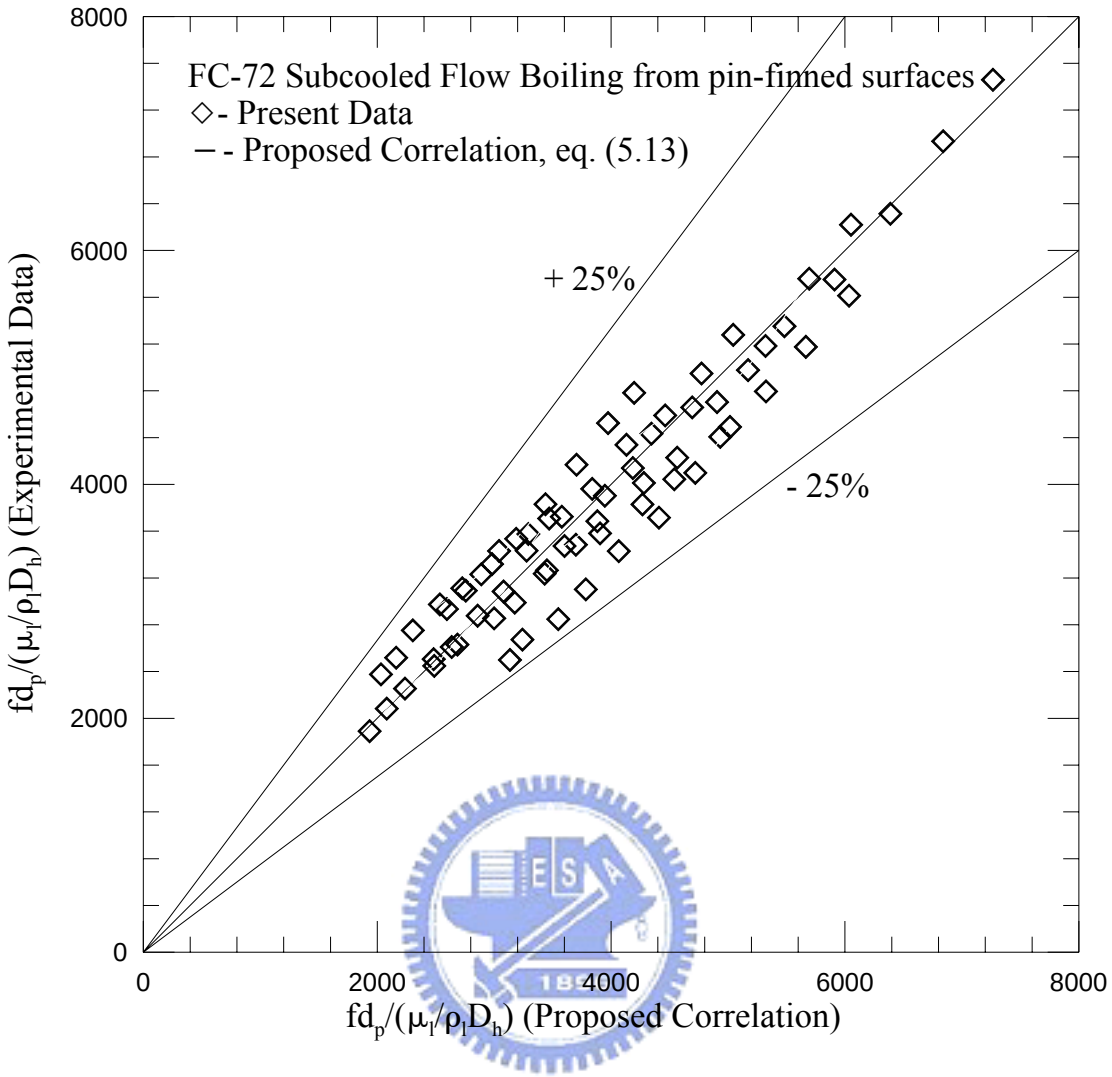

Fig. 5.52 Comparison of the measured data for mean bubble departure frequency for subcooled flow boiling of FC-72 on pin-finned surfaces with the proposed correlation

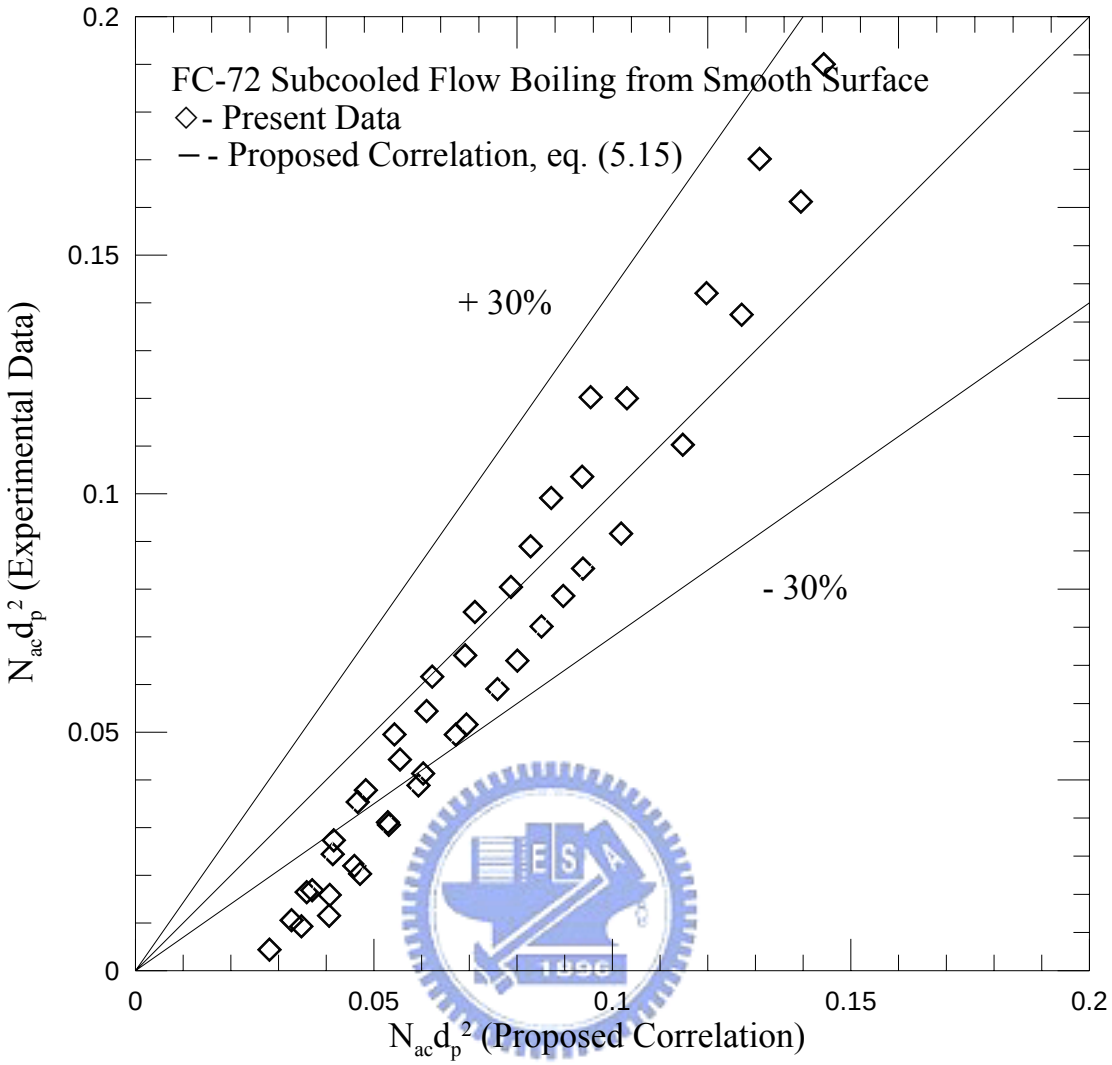

Fig. 5.53 Comparison of the measured data for mean active nucleation site density for subcooled flow boiling of FC-72 on smooth surface with the proposed correlation

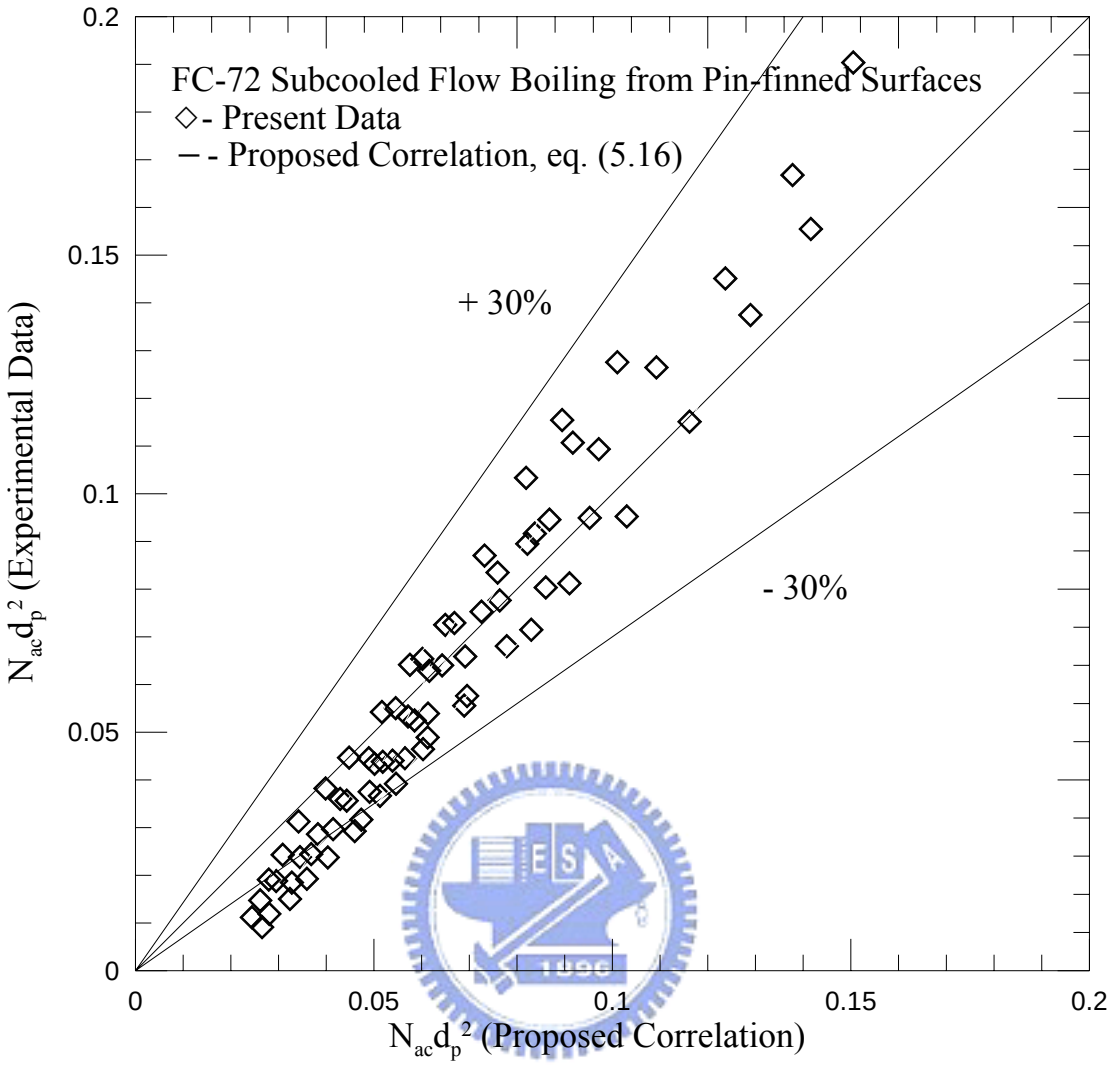

Fig. 5.54 Comparison of the measured data for mean active nucleation site density for subcooled flow boiling of FC-72 on pin-finned surfaces with the proposed correlation

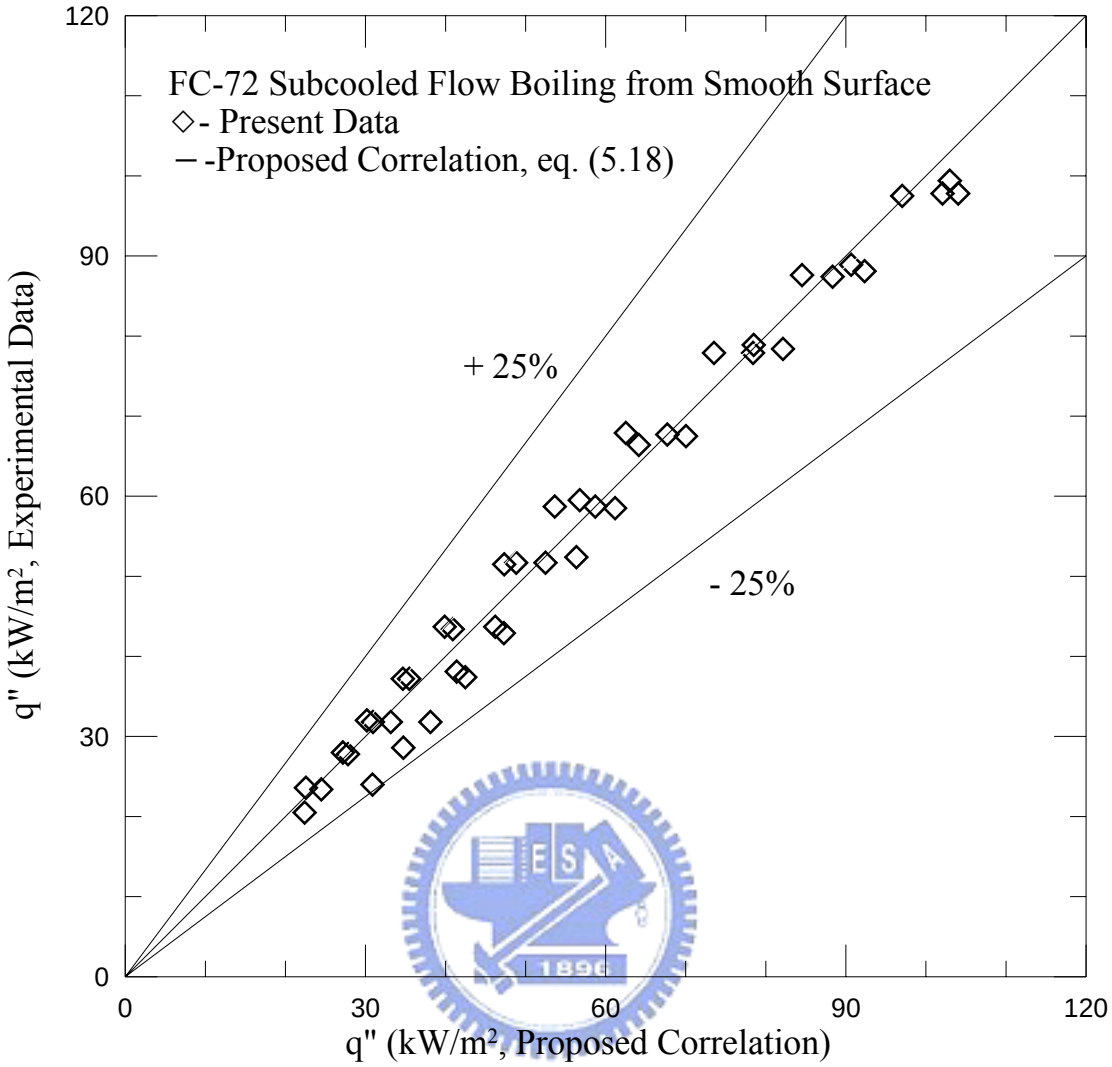

Fig. 5.55 Comparison of the measured data for boiling heat flux for subcooled flow boiling of FC-72 on smooth surface with the proposed correlation

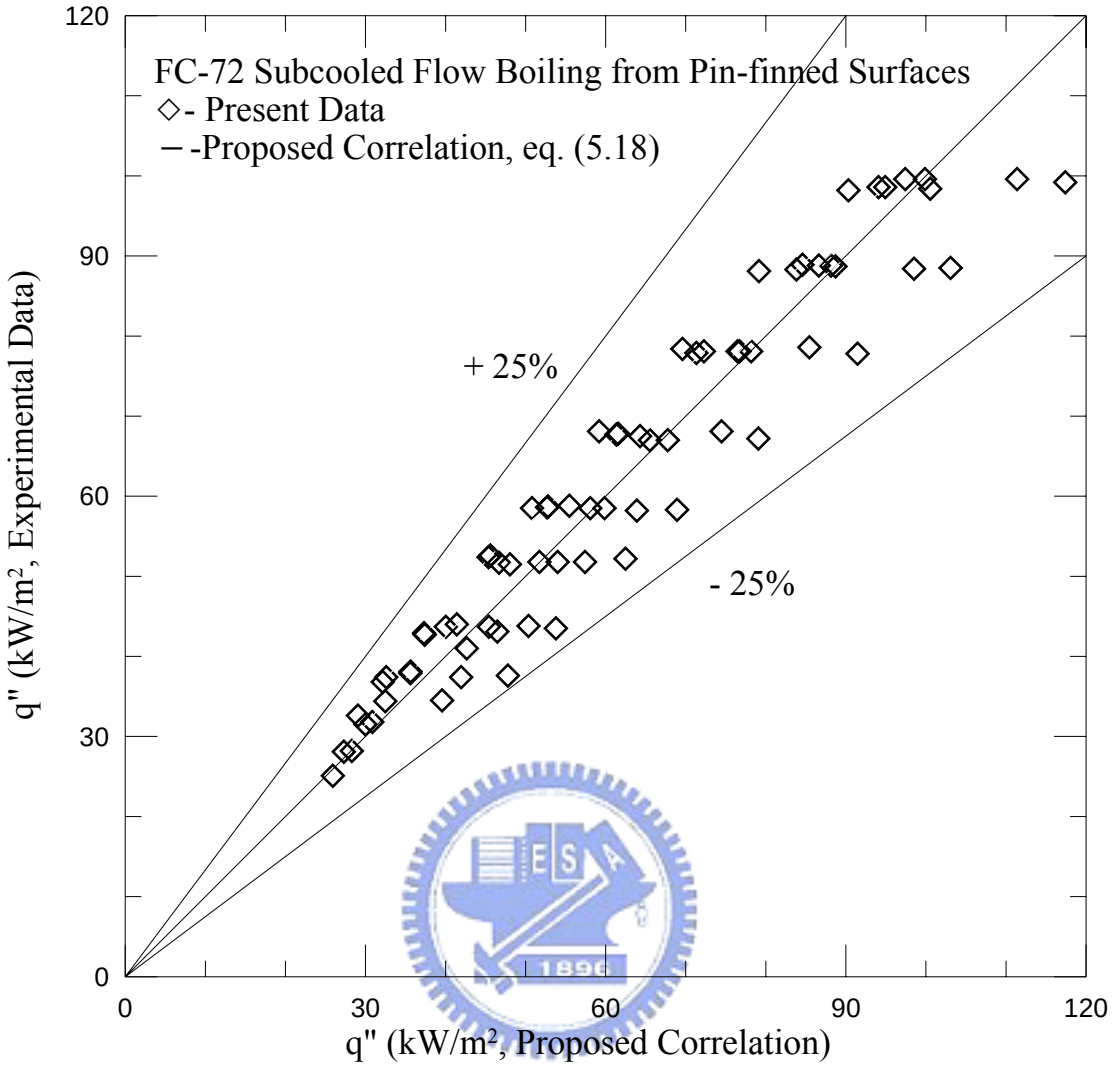

Fig. 5.56 Comparison of the measured data for boiling heat flux for subcooled flow boiling of FC-72 on pin-finned surfaces with the proposed correlation